The dryer section of a paper machine

Modelling and simulation

S. Buysse

Technische Universiteit Delft

The dryer section of a paper machine

Modelling and simulation

by

S. Buysse

to obtain the degree of Master of Science
at the Delft University of Technology,
to be defended publicly on Friday September 3, 2021.

Student number:	4363825	
Project duration:	September 1, 2020 – September 3, 2021	
Thesis committee:	Prof. dr. ir. R. A. W. M. Henkes,	TU Delft, supervisor
	Dr. ir. M. J. Tummers,	TU Delft
	Ir. B. Duller,	Kadant Johnson

TUDelft

Abstract

Currently, the paper producing industry is a significant energy consumer and contributes to the excessive greenhouse emissions. In order to become carbon neutral by 2050, it is evident that the paper industry must become more sustainable as well. Most of the energy is consumed in the dewatering process. Therefore, optimizing this process is key for efficient operation and reducing the carbon footprint.

Since the late 1950's, there have been several models proposed to describe the dryer section of a paper machine. However, the majority did not capture internal transport phenomena resulting in inadequate models for heavier paper grades. In this work, a comprehensive physical-numerical model is developed that describes the internal transport phenomena in multicylinder paper drying. The model solves a set of two differential equations describing the moisture content and temperature in the thickness direction of the sheet. The model can be solved by imposing time-varying boundary- and initial conditions. The model includes unfelted and double-felted cylinders.

Correlations for multiple thermodynamic properties are proposed and evaluated. Heat and mass transfer coefficients at the open surface are determined using the Chilton-Colburn analogy. Furthermore, the sorptive characteristics are fully accounted for.

In order to find the most applicable thermodynamic properties, the model is validated against data gathered in a field survey, carried out as part of this project. In this field survey, a paper grade of 203 $\left[\frac{g}{m^2}\right]$ running at 403 $\left[\frac{m}{s}\right]$ was investigated. Temperature measurements were performed in order to determine the conditions per cylinder. A final moisture content and two temperature profiles were used as test criteria to validate the model. Furthermore, the survey gave direct insight on the state of the dryer section: Cylinder 23 was found to be in the flooded state and the warm-up time was too long.

The model was found to slightly overestimate the final moisture content: the calculated final wet-basis moisture content at the end of the pre-dryer section was 0.235 $\left[\frac{kg}{kg}\right]$, which is 0.022 $\left[\frac{kg}{kg}\right]$ above the measured final moisture content. The calculated temperature profiles closely followed measured values.

The effect of changing three operating conditions was evaluated. This involved fixing the relative humidities in the pockets, felting the first 10 cylinders and varying the machine speeds. By fixing the relative humidities in the pockets, the final moisture content increased by almost 20%. However, a 60% reduction in volumetric flow rate over the fans could be achieved. Felting the first 10 cylinders results in a 50% reduction in the warm-up length and a 8.9% decrease in the final moisture content. Lastly, it was found that for an increased machine speed, the final moisture content increases as well, due to reduced heat transfer and drying time.

This Master Thesis Project was carried out by the author at the company Kadant Johnson in the Netherlands

Contents

Nomenclature

Acronyms

CMC	Critical Moisture Content
EMC	Equilibrium Moisture Content
FSP	Fibre Saturation Point
IMC	Irreducible Moisture Content
IR	Infrared
MAE	Mean Average Error
MG	Machine Glazing
PM	Paper Machine
REV	Representative Elementary Volume
RH	Relative Humidity
TMD	Temperature Measurement Distance

Greek symbols

ϕ	Relative humidity of air $[-]$
γ	Surface tension $\left[\frac{N}{m}\right]$
λ	Thermal conductivity $\left[\frac{W}{mK}\right]$
μ	Dynamic viscosity $[Pas]$
ν	Kinematic viscosity $\left[\frac{m^2}{s}\right]$
ϵ	Porosity $[-]$
ρ	Density $\left[\frac{kg}{m^3}\right]$

Roman symbols (upper case)

A	Surface area $[m^2]$
$C_{p,\,(i)}$	Specific heat capacity of species i $\left[\frac{kJ}{kgK}\right]$
D_{12}	Diffusivity of species 1 into species 2 $\left[\frac{m^2}{s}\right]$
D_{eff}	Effective diffusivity $\left[\frac{m^2}{s}\right]$
H_i	Enthalpy of species i $\left[\frac{kJ}{kg}\right]$
H_{ev}	Heat of evaporation $\left[\frac{kJ}{kg}\right]$
H_s	Heat of sorption $\left[\frac{kJ}{kg}\right]$
K	Absolute permeability $[m^2]$

L	Paper thickness $\left[\frac{W}{m^2K}\right]$
M	Dry-basis moisture content $\left[\frac{kg}{kg}\right]$ (dry)
M_i	Molar mass of species i $\left[\frac{kg}{mol}\right]$
M_{bound}	Bound water moisture content $\left[\frac{kg}{kg}\right]$ (dry)
M_{free}	Free moisture content $\left[\frac{kg}{kg}\right]$ (dry)
M_{irr}	Irreducible moisture content $\left[\frac{kg}{kg}\right]$ (dry)
M_{wet}	Wet-basis moisture content $\left[\frac{kg}{kg}\right]$ (wet)
N	Number of nodes $[-]$
P	Total pressure $[kPa]$
P_c	Capillary pressure $[kPa]$
P_e	Entry Pressure $[kPa]$
P_i	Partial pressure of species i $[kPa]$
$P_{(a),fixed}$	Fixed remaining partial pressure of air $[kPa]$
R	Radius of curvature $[m]$
R	Universal gas constant $= 8.314$ $\left[\frac{J}{Kmol}\right]$
R_i	Specific gas constant for species i $\left[\frac{J}{kgK}\right]$
S	Volumetric saturation$[-]$
S^*	Normalized volumetric saturation$[-]$
S_r	Residual volumetric saturation$[-]$
T	Temperature i $[K]$
V	Volume $\left[m^3\right]$

Roman symbols (lower case)

b_{wt}	Basis weight $\left[\frac{kg}{m^2}\right]$ (dry)
g	Gravitational acceleration $\left[\frac{m}{s^2}\right]$
h_c	Contact heat transfer coefficient $\left[\frac{W}{m^2K}\right]$
h_m	Mass transfer coefficient $\left[\frac{m}{s}\right]$
h_s	Heat transfer coefficient $\left[\frac{W}{m^2K}\right]$
j_i	Diffusive mass flux of species i $\left[\frac{kg}{m^2s}\right]$
k_w	Wetting-phase relative permeability$[-]$
k_{nw}	Non-wetting-phase relative permeability$[-]$

$\dot{m}$	Evaporation rate $\left[\frac{kg}{m^2 s}\right]$
m_i	Mass fraction of species i $\left[\frac{kg}{kg}\right]$
n_i	Absolute mass flux of species i $\left[\frac{kg}{m^2 s}\right]$
r	Pore radius $[m]$
t	Time $[s]$
v	Velocity $\left[\frac{m}{s}\right]$
x	Absolute humidity $\left[\frac{kg}{kg}\right]$
y	Coordinate in the thickness direction $[m]$
z_{dr}	Dry-solids-to-water ratio $\left[\frac{kg_{dry\ solids}}{kg_{water}}\right]$
z_{dsc}	Dry-solids content $\left[\frac{kg}{kg}\right]$

Subscripts

a	Air
atm	Atmospheric conditions
$average$	Average condition
bd	Bone-dry condition
$bound$	Free liquid water
da	Dry air
db	Dry bulb condition
dp	Dew point
ds	Dry solids
f	Fibres
$free$	Free liquid water
FSP	Fibre saturated condition
g	Gas
i	Space index
j	Time index
l	Liquid
$pocket$	Pocket condition
tr	Transition to turbulence
v	Vapour
w	Water

wb	Wet bulb condition

Superscripts

$'$	Saturated conditions

List of Figures

List of Tables

1 Introduction

Although the world is becoming increasingly more digital, paper still is an essential medium that is used in everyday life. It is used in large volumes for storing and recording information. In addition, it is increasingly more used in the wrapping and packaging industry as it tries to step away from plastics. Although it might be perceived as a dying industry, it is in fact a continuously developing industry. In 2018 the production volume of paper and cardboard worldwide was 419 million metric tonnes, and it is still increasing year by year [17].

Globally, the pulp and paper contributes to 5.7% of the industrial final energy use [25] [26]. Furthermore, this industry is ranked fourth in the largest greenhouse gas emitting industries according to [27]. In Europe, the paper industry is among the biggest industrial energy consumers and, therefore, also largely contributes to the excessive greenhouse emissions [28]. The goal set by the European Union [29] is to reduce greenhouse emissions by 80-95% by 2050 compared to levels from 1990. Depending on the type of paper grade that is produced, it requires between 5-17 GJ of energy to produce one tonne of paper [30]. This energy intensive level is comparable to that of steel and cement production. Especially the dryer section of a paper machine is very energy consuming: up to 75% of the total energy consumption is used by the drying section of the paper machine. Therefore, improving the energy efficiency of the dryer section of a paper machine and reducing its energy consumption can be of importance to reach the goals set by [29].

This energy consumption mainly comes in the form of steam (approximately 80% according to Reardon [11] and 78% according to Edelmann [31]). Therefore, increasing the efficiency of the drying section of a paper machine has a considerable effect on the carbon emission and, thus, on global warming. Of course, reducing the energy consumption is also beneficial from an economical point of view. When the specific energy consumption per cylinder can be reduced, this will decrease the energy consumption per tonne paper produced.

Besides the dewatering task, the dryer section has several other tasks and requirements. In the dryer section, the specified paper properties are formed, such as the dry basis weight and strength, by configuring the cylinders in special setups and adding coatings or other chemicals. Another important feature is the equality of the evaporation profile in the cross-machine direction as this influences the quality and runnability of the paper machine. Therefore, a better understanding of the drying process and an increase in the effectiveness allows for new paper grades to be investigated for continuous production and ensures existing paper grades to be produced with fewer cylinders. [22]

Through the years paper machines have been upgraded in several stages increasing the production speed. However, in most cases the limiting production factor was the dryer section. Therefore, increasing the runnability of the drying section alone often causes an increase in the overall runnability of the whole paper machine directly.

In addition, a better understanding of the drying process can help predicting the effect of modifications. However, this requires the availability of a reliable, extensive and sophisticated drying model, which covers a wide range of processes that happen during drying.

The purpose of the present Master project is to develop, test and validate a one-dimensional model that captures all essential internal- and external transfer phenomena occurring in the paper web during multi-cylinder drying. The model includes diffusive and convective flow of water vapour and capillary flow of liquid water. By applying time-varying boundary conditions, the model can be solved in the thickness direction of the sheet for the entire length of a dryer section. A second-order accurate numerical scheme is used to solve the model, keeping the computational time to a minimum, while maintaining sufficient accuracy.

The model calculates the moisture content and temperature distribution in the sheet. In this way, a optimal operation point can be set to achieve better paper specifications. Furthermore, the model can be used to predict the effect of future modifications and give insight into the effect of changing operating conditions.

The structure of this report is as follows. Section two gives a general overview of the paper making process. In addition, the the multi-cylinder drying process is treated in more depth. Section three covers the fundamentals used in the model. These fundamentals are deemed necessary to fully understand the transfer phenomena described in later sections. The different drying phases and the structure of the paper web are treated in section four. In section five, mass- and energy conservation equations are constructed that lay the basis for this model. Furthermore, this section treats the assumptions made, proposes different sets of time-varying boundary conditions and explains the second-order accurate discretization methods used. The thermodynamic properties required to solve the mass- and energy equations are elaborated in section six. In this section also the different transfer coefficients are discussed. Section seven treats the data gathered in the field survey. Besides indicating the efficiency of a dryer section, this survey enables validation of the model. In section eight both sets of time-varying boundary conditions proposed in section four are evaluated. The most applicable set is chosen for future calculations. The fitness of the different correlations proposed in section five is discussed in section nine. After selecting the most applicable correlations, the accuracy of the model is tested. Finally, after completion of the model, the effect of changing three operating conditions is discussed in section ten.

This Master Thesis Project was carried out on behalf of the company Kadant Johnson in the Netherlands, while working from home due to the COVID-19 pandemic.

2 A general overview of the papermaking process

Figure 2.1 provides a schematic overview of a paper machine. Before explaining the dryer section of a paper machine in more detail, we first describe the overall paper making process in short. The paper making process is essentially a very large drainage operation. Although several ways exist to make paper, there is a common method. First, the type of fibre is selected. This type of fibre depends on the location of the paper mill and the specifications needed in the paper grade. After chopping and transporting the wood, the bark is removed. Subsequently, the wood is chipped into smaller pieces and ready for transport to the paper mill. Not only freshly chopped wood is used for making paper. Wood and paper products are recycled most of the time. In this case, the paper is taken to a recycling plant where it is separated into types and grades. Next, the separated paper is washed, so inks, plastics and glue are removed. Now this recycled material can be fed back to the paper mill as well.

In the paper mill the new or recycled material is fed into a digester, where it is cooked in a acidic solution to dissolve the lignin and separate the plant fibres. Next, the pulp obtained is washed to remove the acid solution. Depending on the required paper specifications, different chemicals (colouring agents, fillers, etc..) and water are mixed with pulp creating the right pulp solution. This pulp solution can now be transported to the paper machine, where the final product is created. Figure 2.1 provides a schematic overview of a paper machine. At this point the pulp solution consists of 2-10 g fibre per kg water. At the beginning of the paper machine is the head-box, where the pulp solution is injected at high pressure directly into the space between two continuously rotating wires. The headbox transforms the continuous pipeline flow into uniform rectangular flow equal in width to the paper machine and at uniform velocity in the machine direction [11]. A change in the rate and angle of discharge can have a considerable effect on the final paper quality and should therefore be closely monitored.

The two continuously rotating wires carry the pulp into the gap former, which rapidly drains the excess water using gravitation, pulsation, or vacuum. At this point, the consistency of the web is commonly given as the ratio of dry solids to the total weight. Its value varies between 0.15 to 0.25 [11], [22]. Furthermore, the paper web is now a continuous one, but still very wet and fragile and should therefore be continuously supported by a supporting felt.

The continuous web of paper is then transported into the press section, where a large part of the water is removed through pressure. The water is carried away by water-absorbing fabric. By pressing the water out of the web a consistency of 33-55% (i.e. 1.7-1 $\left[\frac{kg}{kg}\right](dry)$) can be obtained depending on the pressing technology and the paper grade. Now the paper web is ready for the dryer section.

In short, the paper web is transported over a number of cylinders. This number varies between 40 and 120, depending on the efficiency of the dryer section, the paper grade produced and the desired final moisture content. Steam is fed into the cylinders, while they are continuously rotating. Inside the cylinder, the steam condensates on the inner cylinder walls releasing its latent heat to the cylinder wall. The heat is transported through the cylinder wall to the paper web, resulting in evaporation of water inside the web. The water removal results in a reduced moisture content. The condensate that is formed in the cylinders leaves the cylinder through a rotating or static siphon, depending on the pressure differential over the cylinder and the rotational speed. In order to enhance the drying rate, blow boxes are installed so that the pockets are ventilated and moisture is removed. The pockets are defined as the open spaces between the cylinders. The air provided is dry and warm, enhancing evaporation in two ways. Firstly, warm air can take up more water vapour compared to cold air. The fundamentals behind this phenomenon will be discussed in section 3.2.2. Secondly, the air provided has a low relative humidity, causing a larger gradient in vapour pressure, increasing the water vapour transport from the web (See section 3.3.5). According to [22], after the drying section the dry basis moisture content can be reduced to 3-8% depending on the required final moisture content.

Besides the drying function, the dryer section may include sizers and coaters as well. Here several chemicals are added to the paper web in order to meet the specifications of the final product. For instance, in speed sizers extra starch is added to the paper web in order to increase the strength of the paper. Coaters are implemented if a protected layer is required.

Besides adding chemicals to meet the paper requirements, the paper web can also be mechanically treated. In the calendaring process the paper web is compressed between two metal rolls in order to smoothen the surface for better printability. In the last part of the dryer section, the paper may be transported over a cooling cylinders to cool down the paper web. Transporting the paper web over cooling cylinder before winding it up onto a reel will reduce the cooling time.

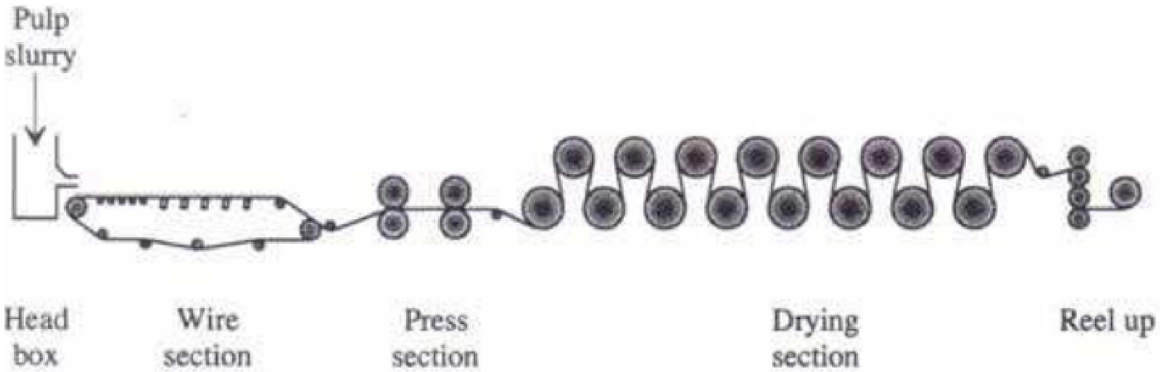

Figure 2.1: Simplified sketch of a typical paper machine. [2]

As mentioned before, within each section water is removed. Sadeghi [22] reports the following water removal quantities per subsection:

- Forming (or Wire) section: 200 $\left[\frac{kg_{water}}{kg_{dry}}\right]$
- Press section: 2.5 $\left[\frac{kg_{water}}{kg_{dry}}\right]$
- Dryer section: 1.5 $\left[\frac{kg_{water}}{kg_{dry}}\right]$

It can be seen that by far the most water is removed in the first stage of the dewatering process. It is important that the paper web is as dry as possible before it enters the drying section, because water removal in the dryer section is much more energy intensive compared to the forming or press section. 1% reduction in the moisture content($\left[\frac{kg}{kg}\right]$ (dry)) before entering the drying section will result in a reduction of 4% in the final moisture content at the reel [5]. Based on Sadeghi's water removal quantities per subsection, the dryer section removes less than 1% water volume originally received by the forming section.

2.1 Multicylinder drying in detail

The main method for drying paper is multicylinder drying. It is accepted to be an economical beneficial way, while providing decent sheet properties. For paper drying, Karlsson [5] and Ghosh [2] estimate that multicylinder drying is preferred in 90% of all cases. It has a good energy efficiency, while it also serves the purpose of transporting the web forward.

2.1.1 Configurations

In general, there are two ways in which cylinders can be arranged: a single tier configuration and a double tier configuration. Since the implementation of the first continuous dryer sections there has always been a felt supporting the paper web. The configuration of the felt can also be categorised in two ways: a doublte-felted configuration and a single-felted configuration. The most common combined configurations are shown in figure 2.2 and will be discussed below.

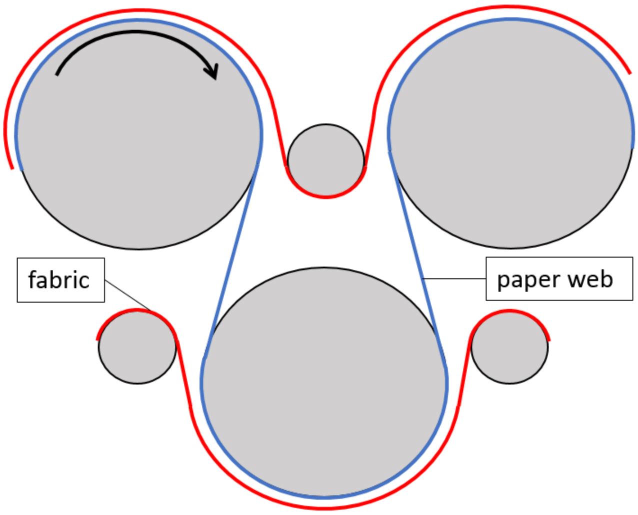

(a) Two-tier double-felted configuration.

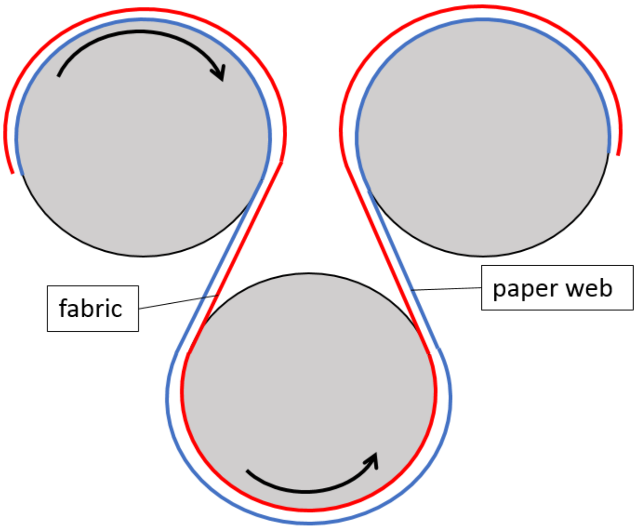

(b) Two-tier single-felted configuration.

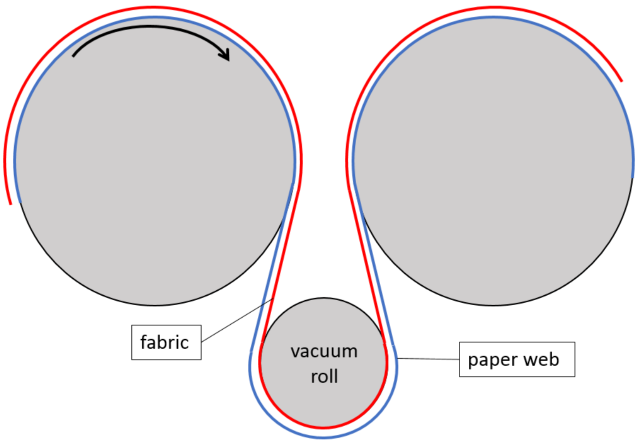

(c) One-tier single-felted configuration.

Figure 2.2: The three most common cylinder and felt configurations.

2.1.1.1 Two-tier double-felted

In figure 2.2a a double two-tier double-felted configuration is shown. Since the introduction of the multicylinder drying concept in the 19^{th} century, the two-tier configuration has been used the most. In this configuration both the top and bottom cylinders contribute to the heating of the paper web. The web is transported from the top to bottom cylinder and back to the next top cylinder again.

Between the cylinders the paper web is unsupported by the felt, leaving it vulnerable to breaking. This is especially the case in the beginning of the drying section where its tensile strength is still low. Therefore, this configuration can only be applied at lower machines speeds or at the end of the dryer section for increased speeds.

2.1.1.2 Two-tier single-felted

Over the years the aim has always been to improve the productivity of the dryer section by increasing the machine speed. However, the increase in machine speed led to more breaks in the paper web, causing runnability problems. The breakage was caused by the fluttering of the paper web between the cylinders and, therefore, a single-felted two-tier configuration was introduced. As can be seen in figure 2.2b, the paper web is now supported by a felt running from cylinder to cylinder supporting the felt along the way. In this configuration, the paper is continuously supported by the felt. This configuration is, however, not optimal. The two-tier single-felt configuration causes the fabric felt to be squeezed between the paper web and cylinder in either the top or bottom cylinder row, depending on the location of the supporting felt. This effect resists heat transfer between the outer cylinder wall and the paper web, reducing the effectiveness of drying.

2.1.1.3 One-tier single-felted

In figure 2.2c a one-tier single-felted configuration is shown. Over the years, machine speeds have increased even further, causing other runnability problems. Due to the high speeds, air flow and centrifugal forces became of significant influence. The moving paper web and felt result in a parallel air flow. This results in areas with excessive pressure and negative pressures around the dryers. Figure 2.3 indicates those areas. The high permeability of the fabric and the pressure difference, forces airflow through the fabric, causing the paper web to flutter loose. Together with the fabric offering additional resistance to heat transfer, this causes major runnability problems Therefore, in the 1980s, a new concept was introduced that replaces the bottom cylinders with vacuum rolls to overcome this problem. In these rolls a vacuum is created, so that the paper web sticks to the fabric even better. This allows the dryer section to be operated at higher machine speeds. The heat that is normally added through the bottom dryers should be compensated by adding more top-row cylinders. Therefore, one-tier single-felted configuration often involve longer dryer sections.

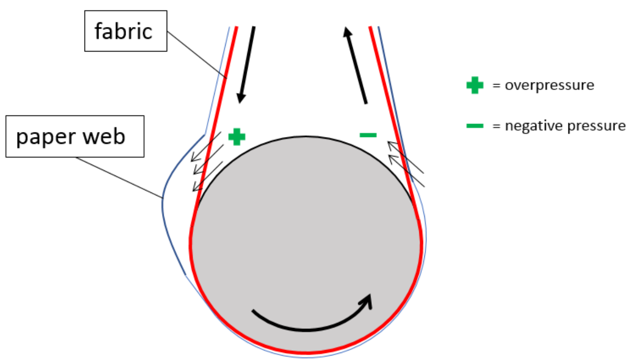

Figure 2.3: Zones of overpressure and negative pressure, caused by the moving paper web and the supporting felt.

2.1.2 Other drying methods

Over the years, several new drying techniques were investigated. Several of them will be discussed below.

Yankee or MG drying

Yankee cylinder drying is another type of cylinder drying that is mainly used for the production of softer tissue. The Yankee cylinder has a typical diameter of 5.5 m and operates in the same way as

common drying cylinders. During this process the thin paper web is transported to the Yankee on a felt. The paper web is pressed on the Yankee, forcing the water out of the paper web into the fabric. The steam-heated Yankee cylinder conducts heat to the paper web, causing very intensive drying. No shrinkage will occur as the paper web is attached to the cylinder during the whole process. At the end of the cylinder, the paper can reach a dryness level of 0.07-0.03 $\left[\frac{kg}{kg}\right]$ (dry). The paper web is than creped from the cylinder using doctor blades. These doctor blades are installed under specific angels, so that a desired creping process takes place. A side view of a Yankee dryer installation and the creping process are presented in the appendices A.2.2 and A.2.1, respectively.
Besides the production of tissue, this drying technique is also used for machine glazing to create a smoother surface. This machine glazing is often abbreviated by MG.

Infrared (IR) drying
This drying technique is commonly used in combination with cylinder drying. This can be found after coater or sizer installations, because the wet coating or sizing does not allow contact drying to be used. Instead, radiative drying is preferred until the applied coating or sizing is properly attached to the paper web.

Impingement drying
In this drying method a high-velocity high-temperature air jet focuses directly on the paper web, breaking the stagnant boundary layer. This greatly enhances the heat transfer coefficient, affecting the production efficiency positively. This technique has only been commercially available for over a decade and is therefore mostly common on new machines. It is commonly installed along side a Yankee cylinder as the air impingement technique is mostly effective for very thin sheets [32].

2.1.3 Cylinder

In figure 2.4 a cross section is shown of a typical heating cylinder or dryer. In the dryer section the dryers or heated cylinders have two major tasks: transporting the web forward and providing heat to the paper web to achieve the desired moisture content at the reel. They can be considered as large cylinders with heads bolted onto them. Modern cylinders are made of several materials. A thinner cylinder wall can be used for the same operating pressure if stronger materials are used. A thinner cylinder wall means less resistance to heat transfer, which is important efficient operation. Some materials have a higher thermal conductivity than others. Therefore, a strong material, with a high thermal conductivity, is often preferred. In outdated paper machines, cast iron was often used, because of the relative easy casting process. Nowadays, dryers exist in variety of sizes, but the most common and used today have a diameter of 1.5 or 1.8 meter. According to Stenström [33], the shell thickness ranges between 25 and 35 mm, while [5] reports a range between 25 and 40 mm. Over the years, production speeds and, therefore, rotational speeds have increased. In the early 19$^{\text{th}}$ century the rotational speed was very low. The coal was shovelled into the cylinder on one side, while the ash was removed at the other side [33]. Nowadays, typical paper machines can be over 10 m wide and reach production speeds over 2000 m/min for lightweight paper grades ([5] and [33]).
More information about the behaviour of the condensate, the effect of non-condensables, the effect of driving power and equipment used in the dryer cylinders can be found in appendix A.1.

2.2 Dryer section ventilation

In the early days of continuous paper drying, air handling was not considered and the water vapour would simply spread across the machine room, creating a very moist unpleasant working environment. As production speeds increased, air handling became a major roll, because of the interaction between the paper web and the air surrounding it. Several subsystems have therefore been installed on modern dryer sections to tackle the ventilation problem [5]:

- Hood and basement enclosure
- Pocket ventilation

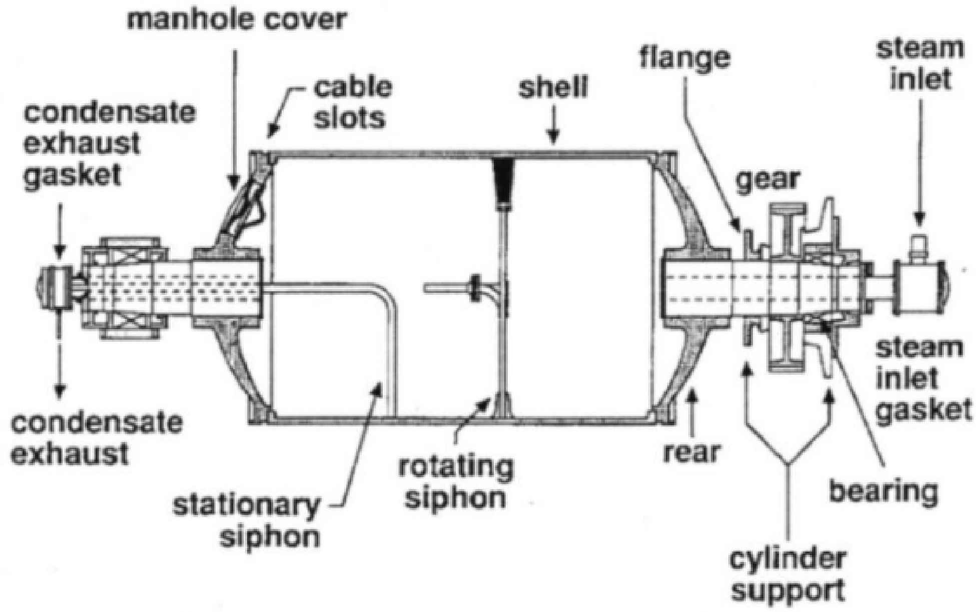

Figure 2.4: A cross sectional drawing of a typical cylinder used in multicylinder drying. [3]

- Heat recovery

The effect of the hood and basement enclosures is not described here, but can can be found in appendix A.3.

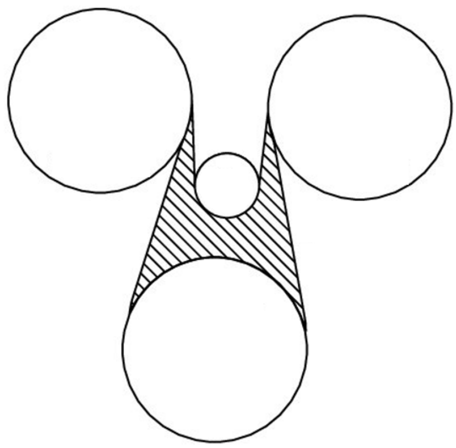

Figure 2.5: Location of a pocket in a two-tier double-felted configuration [4]

2.2.1 Pocket ventilation

Ghosh et al. [2] and Ghodbanan et al. [34] describe the pocket as the space in the dryer section between two adjacent cylinders (in case of single-tier systems) or between three cylinders (in case of two-tier systems). Figure 2.5 shows a pocket for a two-tier double-felted configuration. The pocket is enclosed by the cylinder, fabric and paper web.
Pocket ventilation is, therefore, the ventilation of these spaces. The main purpose of the pocket ventilation is to keep humidity levels low and evenly spread the supply air in the cross machine direction. In this way more water is evapourated per pocket and uneven moisture profiles are prevented. Over the years the introduction of a more permeable supporting fabric has greatly improved the ventilation. However, this air movement causes the sheet to flutter, causing runnability problems. Therefore, additional blow boxes were introduced to control unwanted air movement and to help keeping the paper web attached to the fabric. Depending on the paper grade produced and the permeability of the fabric

supporting the sheet, several configurations of these blow boxes exist. In appendix A.4, the air flow caused by the permeable fabric itself and common ventilation layouts are shown.

2.3 Steam and condensate

Although each papermachine has its own steam and condensate system design, most use the same operating principles. A simplified P&ID of a dryer section's steam and condensate system is depicted in figure A.5.1. The general working principle and the operating conditions are described below. The two main steam and condensate systems can be distinquised: a cascading system and thermocompressor system. A description of these systems is given in appendix A.6.

2.3.1 General working principle

In general, steam is supplied to the dryer section from a boiler. A small amount of steam is drained from the main steam header for ventilation and other heating purposes. Most of the steam is transported to several smaller dryer sections (Predryer, afterdryer, etc.) as can be seen in figure 2.6. Each section serves a different purpose in the drying process and, therefore, different operating conditions apply. Most subsections require condensate removal and drainage. The condensate formed in these sections is collected in condensate tanks. Often steam is collected in these tanks as well, because blow-through steam is required for good condensate removal. The blow-through steam or flash steam can still be used in other section for efficiency reasons. The effect of blow-through steam will be discussed in section A.6.1 in more detail.

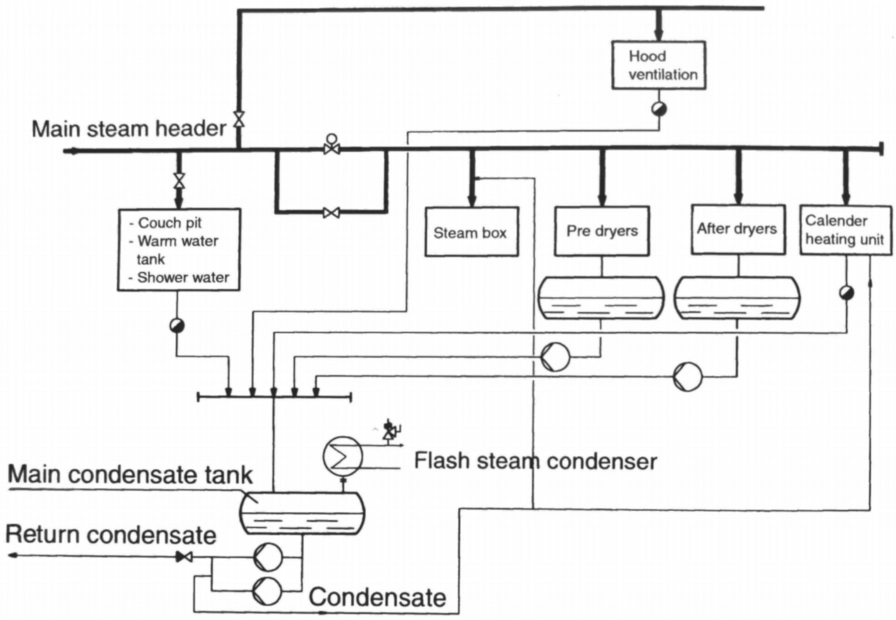

Figure 2.6: Steam supply to different sections of the paper machine [5]

2.3.2 Operating conditions

The lay-out of a steam and condensate system is determined by the operating conditions required for the paper drying process. For example, in beginning of the predryer section, the paper web has a relative low temperature and the web is still very fragile. The paper web should be gradually heated over the first set of cylinders. Otherwise, the fibres might stick to the cylinder wall, resulting in runnability problems. Lowering the temperature of the outer cylinder wall is achieved by reducing the steam pressure.
Moving down the dryer section, the paper web has a higher temperature and evaporation from the paper web takes place at higher temperatures. Therefore, the steam pressure inside the cylinders is increased. Within each subsection in the dryer section, several dryer groups can occur, each operating

at different conditions. For example, in a two-tier configuration the bottom cylinders might operate at different condensation temperatures compared to the top cylinders. In this way the curl of the paper web can be controlled. Consumption of low pressure steam is preferred over high pressure steam as it is beneficial in two ways. Firstly, the cost for producing low pressure steam is lower than for high pressure steam. Secondly, the amount of latent heat is reduced for higher pressures.

2.4 Heat recovery

As already mentioned, the dryer section is the most energy consuming part of the paper machine. Most of the energy supplied to the dryer section comes in the form of steam (Karlsson [5] reports 80%). Karlsson [5] also reports a steam requirement varying between 2.5 and 5.5 GJ to produce one tonne of newsprint and an electrical consumption varying between 1.8 and 2.2 GJ. This large amount of energy supplied to the system provides excellent opportunities for heat recovery. According to Karlsson [5], the heat recovery potential may exceed 20 MW in cold periods. It is therefore beneficial to install modern and efficient heat recovery installations on paper machines. The heat is mostly recovered from exhaust air, because most heat supplied is transferred to the exhaust air.

2.4.1 System variables / optimal operating conditions for heat recovery

In order to determine the efficient operation of the dryer section and optimize the heat recovery it is important to understand how system variables affect the overall energy requirement, the humidity and the amount of leakage air.

2.4.1.1 Exhaust air

The enthalpy of the exhaust air can be increased in two ways: By increasing the temperature and the humidity of the air. Increasing the humidity of air is more favorable than raising the temperature. Therefore, the humidity levels are often raised to a maximum allowable level. If humidities are high, less exhaust air is necessary to carry off the same amount of vapour. This means that fans and ventilators can be turned down, saving electrical costs.

2.4.1.2 Supply and leakage of air

Dry air enters the pockets in two ways: through supply air and through leakage air. Supply air is preheated before being supplied to the pockets. In this way the supply air remains above the dew point, preventing condensation within the hood. Leakage air entering the dryer section of the paper machine is inevitable. This leakage air is not preheated. Besides the condensation problem, this increases the energy consumption. Therefore, the goal is to reach a supply-to-leakage-air ratio as high as possible, within operating limits [5].
A major disadvantage of increased humidities is the negative effect on the driving force for mass transfer from the web. A detailed description will be given in the section 3.3.5, but the important note here is that the driving force for evaporation is reduced.

2.4.2 Heat recovery Unit

Exhaust air is the most common energy source used in heat recovery systems. With the exhaust air energy, several inlet streams can be heated. There exists a priority order in which the inlet streams should be heated. Therefore, the same order of heat exchangers can be found in typical heat recovery units.
The temperature of the hood supply air and of the exhaust air are closely related. Therefore, the air-to-air heat exchanger between the exhaust and supply air comes first in the heat recovery unit. In this heat exchanger, the temperature level of the supply air is raised, while the temperature of the exhaust air drops and condensation takes place.
Following the exhaust air stream, the next heat exchanger in the stack is dependent on the location of the paper machine. For paper machines located in countries with a warmer climate, the heating requirement for pre-heating the machine hall ventilation is reduced. In this case, the heat exchanger

for machine hall ventilation can be installed downstream of the stack. Controlling the machine hall ventilation is important, as this often determines the conditions of the leakage air infiltrating the pockets.

Also a heat exchanger for (pre)heating fresh water exists in the stack. This fresh water can be used in the paper making process or as boiler feed water for steam production. No contamination in fresh water is desired, so indirect heating is incorporated in the heat exchanger design.

Less important streams are located at the end of the stack. Under extreme conditions more heat will be exchanged in the upstream heat exchangers, reducing the amount of available heat in for heat exchangers placed at the end of the stack. Often a water-to-air heat exchanger can be found at this location, through which a glycol/water mixture is fed. This mixture is often used for heating the machine hall.

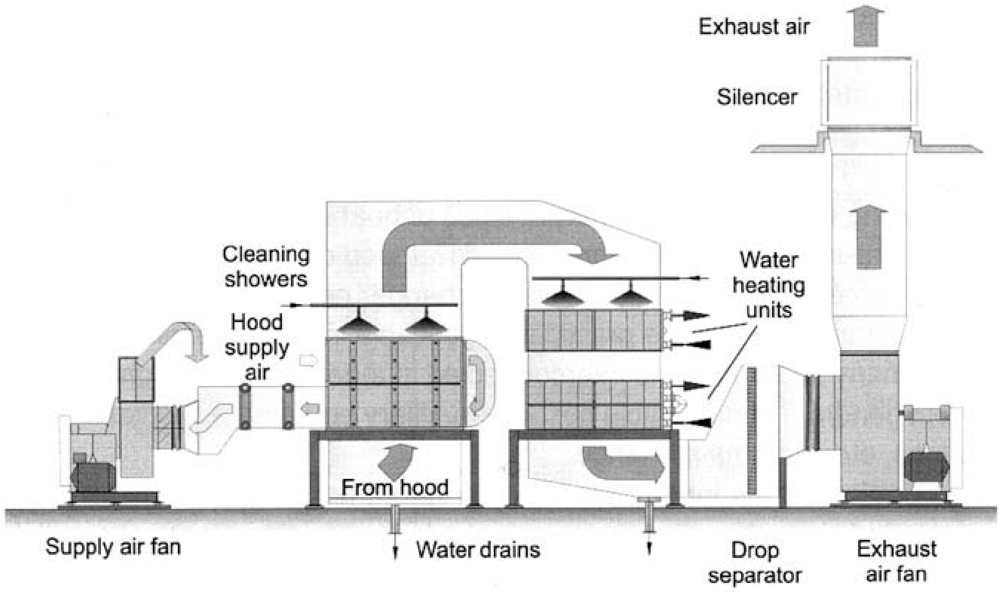

Figure 2.7: Cross-section view of a modern heat recovery unit. [6]

3 Fundamentals

In order to run the drying section of a paper machine at maximum efficiency, it is important to fully understand the drying process. This means understanding the different heat and mass transfer mechanisms that play a role. In this section, the definitions used through-out this work are elaborated. Furthermore, this section treats the fundamentals used to describe the drying process.

3.1 Definitions

Several definitions exist to relate the amount of dry fibre to the water content. In the forming section of a paper machine, it is common to use a dry solids-to-water ratio:

$$z_{dr} = \frac{m_d}{m_w} \tag{1}$$

Further downstream in the drying process, the amount of dry material is related differently to the water content. The dry solids content (*d.s.c.*) relates the weight of the dry solids content to the total weight:

$$z_{dsc} = \frac{m_d}{m_d + m_w} \tag{2}$$

Another way to describe the same relation is by defining the wet basis moisture content (also denoted as $\left[\frac{kg}{kg}\right](wet)$):

$$M_{wet} = \frac{m_w}{m_d + m_w} \tag{3}$$

Besides the dry-solids-to-water ratio, its reciprocal is used also. This is defined as the moisture ratio or dry basis moisture content (4)(also denoted as $\left[\frac{kg}{kg}\right](dry)$):

$$M = \frac{m_w}{m_d} \tag{4}$$

Different properties are defined for air. The moisture content in air is commonly known as the absolute humidity:

$$x = \frac{m_v}{m_a} \tag{5}$$

3.2 Properties of air

3.2.1 Ideal gas law

By applying the ideal gas law (eq.(6d) and eq.(6c)), the moisture content of air can also be described as a function of partial pressures and gas constants (6e).

$$m_v = \rho_v V \tag{6a}$$
$$m_a = \rho_a V \tag{6b}$$
$$\rho_v = \frac{P_v}{M_v R T} \tag{6c}$$
$$\rho_a = \frac{P_a}{M_a R T} \tag{6d}$$
$$x_v = \frac{R_a}{R_v}\frac{P_v}{P_a} \tag{6e}$$

3.2.2 Relative humidity

At a temperature below the boiling temperature, there exists a maximum vapour partial pressure that can be reached in an air-water vapour mixture. This vapour partial pressure is known as the saturation pressure and is a function of temperature. It is depicted in figure 3.1. This means that a limited concentration of water vapour can be present in a air-water vapour mixture. This maximum amount is calculated as:

$$x_v{}' = \frac{R_a}{R_a}\frac{P_v'}{P_a} \tag{7}$$

Note that $'$ denotes the saturated condition. Relating the vapour partial pressure to the saturation pressure results in a formula for the relative humidity:

$$RH = \frac{x_v}{x_v{}'} \tag{8}$$

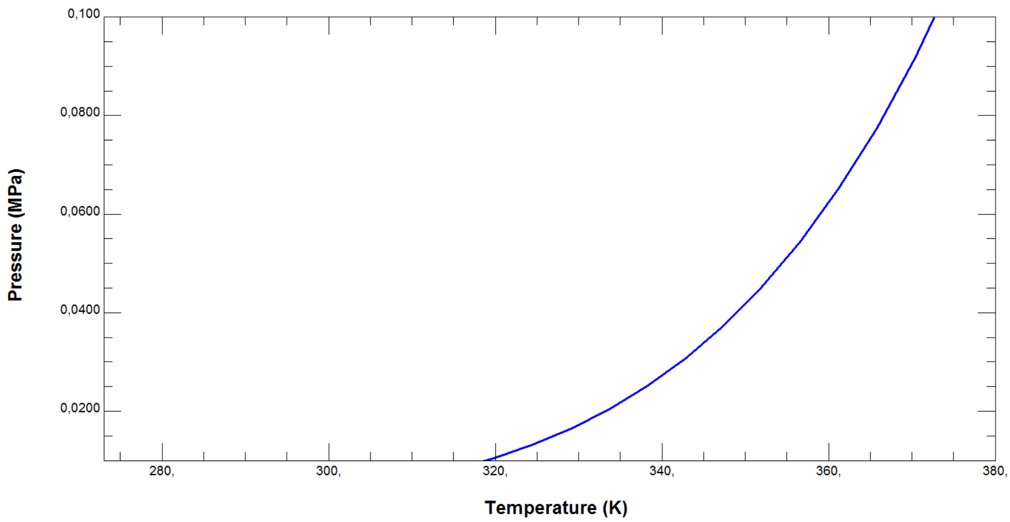

Figure 3.1: Saturated vapour Pressure as function of temperature.

Antoine's equation is a well-known relation between the vapour partial pressure and temperature:

$$P_v' = 100 \times 10^{(A - \frac{B}{C+T})} \tag{9}$$

Where:

- A, B C are fitted parameters.
  [35] reports values of 6.210, 2354 and 7.559, respectively, for the temperature range 293-343$[K]$.
  [36] reports values of 5.084, 1663,45.62, respectively, valid in the temperature range 344-373$[K]$
- T = Temperature $[K]$
- P_v' = Saturated vapour pressure $[kPa]$

3.2.3 Density of humid air

According to Heikkila [14], the density of humid air is a function of temperature, humidity and pressure and can be calculated as:

$$\rho_a = \frac{216.67 P_{tot}(M_{dry} + 1)}{T(M + \frac{M_w}{M_{d.a.}})} \tag{10}$$

Note that in this case M represents the dry basis moisture content $\left[\frac{kg}{kg}(dry)\right]$, M_w denotes the molecular weight of water (= 18.02 $[\frac{g}{mol}]$) and $M_{d.a.}$ denotes the molecular weight of dry air (= 28.97 $[\frac{g}{mol}]$).

3.2.4 Enthalpy of air

Enthalpy is used in order to quantify the amount of energy in the air. The mass fraction of the vapour is only small. Hundy [37] reports 2.16%. In this case, the enthalpy can be defined as:

$$m_a H_a = m_{da} H_{da} + m_v H_v \tag{11}$$

The enthalpies of dry air and vapour can be expanded (eq.(12a),(12b) & (12c)). In these formulas, the reference enthalpy is set to 273.15 K or 0°C for convenience.

$$H_{d.a.} = C_{p,\ (d.a.)}(T - 273.15) \tag{12a}$$
$$H_v = H_v + C_{p,\ (v)}(T - 273.15) \tag{12b}$$
$$H_a = C_{p,\ (a)}(T - 273.15) \tag{12c}$$

By dividing both sides of eq.(11) by $m_a(T - 273.15)$, the specific heat capacity of the mixture can be determined:

$$C_{p,\ a} = C_{p,\ (d.a.)} + x_v C_{p,\ (v)} \tag{13}$$

3.2.5 Wet bulb temperature and air humidity

Air humidities can be calculated using dry- and wet bulb temperatures. The dry bulb temperature is the temperature directly measured by the thermometer, when brought directly in contact with a passing air flow. The wet-bulb temperature is the temperature attained by a fully wetted surface, such as the wick of a wet-bulb thermometer or a wet particle undergoing drying, when brought in contact with an unsaturated air stream. The wet bulb temperature can be measured by wrapping a wet cloth around a thermometer. Passing air will cause water to evapourate due to a difference in the vapour partial pressure. In order to evapourate the water, a certain amount of energy is required. It is assumed that the rate of heat convected to the system equals the rate of mass evapourating from the system [38]. The required evaporation energy will cause a drop in the surrounding temperature. Therefore, the wet bulb temperature always remains below the dry bulb temperature.
The humidity of the air stream can be calculated once the dry- and wet bulb temperatures are known using eqs.(14). In eq.(14a) the saturated pressure at the wet bulb temperature is calculated. Subsequently, the absolute humidity of the air is calculated using eq.(14b). Lastly, eq.(14c) is used to calculate the humidity of the air stream. Karlsson [5] and Devres [39] derived these equations from psychometric charts.

$$P'_{v,\ (wb)} = \exp\left\{11.78 \frac{T_{wb} - 99.64}{T_{wb} + 230}\right\} \tag{14a}$$

$$x'_{v,\ (wb)} = \frac{M_{da}}{M_w} \frac{P'_{v,\ (wb)}}{P_{tot} - P'_{v,\ (wb)}} \tag{14b}$$

$$x = \frac{C_{p,\ (da)}(T_{wb} - T_{db}) + x'_{v,\ (wb)}(H_{ev} + (C_{p,\ (w)} - c_{C,\ (v)})T_{wb})}{H_{ev} + C_{p,\ (v)}T_{db} - C_{p,\ (w)}T_{wb}} \tag{14c}$$

The subscripts wb and db denote conditions at wet- and dry bulb temperatures, respectively. The subscripts v, da and w denote the species water vapour, dry air and liquid water, respectively. $P'_{(v,\ wb)}$ represents the saturated vapour pressure at the wet bulb temperature. $x'_{(v,\ wb)}$ represents the maximum absolute humidity at wet bulb temperature. M_v and M_{da} denote the molecular weights of water vapour and dry air, respectively.

3.2.6 Dew point

The dew point can be defined as the temperature at which the humidity in air will start to condense upon cooling of the air [5]. It can be determined directly from psychometric charts or by means of equations. Karlsson [5] used eqs.(15) to obtain the dew point from humidity and absolute pressure.

$$P_v = \frac{xP_{tot}}{x + \dfrac{M_a}{M_w}} \tag{15a}$$

$$T_{dp} = 99.64 + 329.64\frac{\ln P_v}{11.78 - \ln P_v} \tag{15b}$$

In this case, T_{dp} denotes the dew point (in [$°C$])

3.3 Evaporation from web

One of the most important aspects in paper drying modelling is describing how water is transported from the paper web to its surroundings. Due to the complex configuration of a dryer section, it is very difficult to solve this problem using boundary layer equations as this involves 3D coordinates. However, determining mass- and heat transfer coefficients is key for accurate modeling. Numerous studies have been performed to determine these coefficients for different configurations. In the present study, the evaporation from the web will be modeled as evaporation from a flat plate, although the paper web does not follow a straight path. However, the drying rate will be highest on the locations between the cylinders, where both sides of the paper web are available for evaporation. In those pockets the paper follows a straight path. Therefore, assuming evaporation from a flat plate is justified.
In order to estimate the heat and mass transfer coefficients, firstly an overview of the involved dimensionless groups will be given. Secondly, correlations used in literature to describe flow over a flat plate will be discussed to determine the heat transfer coefficient. Lastly, analogies between heat- and mass transfer correlations will be explained, so the mass transfer coefficient can be determined.

3.3.1 Dimensionless groups

For modeling evaporation from the paper web, existing correlations from the literature will be used. These correlations are presented in dimensionless form to make them applicable to many cases. A list of the relevant dimensionless groups can be found in appendix A.7.

3.3.2 Flow over a flat plate

As described above, the flow-over-a-flat-plate configuration will be used to model evaporation from the web. This configuration is shown in figure 3.2. Numerous studies have been done for this configuration and well-known heat transfer correlations exist. From these correlations the heat transfer coefficient can be determined. By using the analogy between heat and mass transfer (section 3.3.3), the mass transfer coefficient can be determined as well.
In order to determine the heat transfer coefficient, the problem is divided into a laminar and turbulent part. According to Mills [40], the instability that initiates the laminar-turbulent transition usually happens at around $Re_x = 5 \times 10^5$ for a flow-over-a-flat-plate configuration (here the Reynolds number is based on the local distance x counted from the leading edge of the plate).

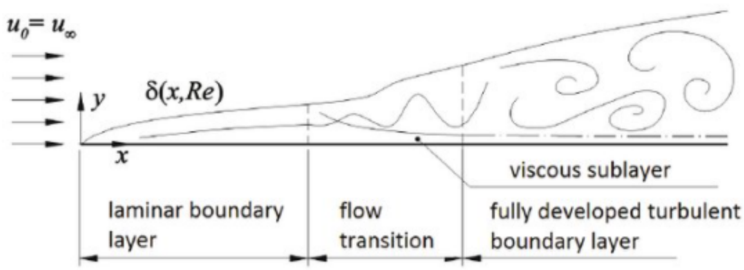

Figure 3.2: Boundary layer development for a flow-over-a-flat-plate configuration. The transition region from laminar to turbulent occurs at around $Re_x = 5 \times 10^5$. [7]

For the laminar part, the local Nusselt number is given by:

$$Nu_x = 0.332 Re_x^{\frac{1}{2}} Pr^{\frac{1}{3}}, \qquad \text{for } 0.6 < Pr < 10 \tag{16}$$

Where:

- $Nu_x = \frac{h_s x}{\lambda}$ = Nusselt number evaluated a distance x from the leading edge.
- $Re_x = \frac{\rho U x}{\mu}$ = Reynolds number evaluated a distance x from the leading edge.

Note that L represents the characteristic length and h_c represents the heat transfer coefficient. For the turbulent part, no analytical solution exists. However, based on experimental data, Whitaker [41] proposed the following correlation:

$$Nu_x = 0.029 Re_x^{0.8} Pr^{0.43}, \qquad \text{for } 0.7 < Pr < 400,\ 5 \times 10^5 < Re_x < 3 \times 10^7 \tag{17}$$

In order to determine the average Nusselt number ($\overline{Nu_L}$) for a certain length from the leading edge, the average heat transfer of the combined laminar and turbulent regime should be evaluated:

$$\bar{h}_s = \frac{1}{L}\left[\int_0^{x_{tr}} h_{s,\,(x)}(laminar)dx + \int_{x_{tr}}^{L} h_{s,\,(x)}(turbulent)dx\right] \tag{18}$$

Rearranging and substituting eq.(18) and (17):

$$\bar{h}_c = \frac{1}{L}\left[\int_0^{x_{tr}} (\frac{\lambda}{x})0.332 Re_x^{\frac{1}{2}} Pr^{\frac{1}{3}} dx + \int_{x_{tr}}^{L} (\frac{\lambda}{x})0.029 Re_x^{0.8} Pr^{0.43} dx\right] \tag{19}$$

The average Nusselt number ($\overline{Nu_L}$) can now be obtained:

$$\overline{Nu_L} = 0.664 Re_{tr}^{\frac{1}{2}} Pr^{\frac{1}{3}} + 0.036 Re_L^{0.8} Pr^{0.43}\left[1 - \left(\frac{Re_{tr}}{Re_L}\right)^{0.8}\right] \tag{20}$$

For a transition Reynolds number $Re_{tr} = 5 \times 10^5$ and a Prandtl number near unity ($Pr \approx 1$ for gasses), eq.(20) can be simplified to eq.(21a). For high Reynolds numbers, only the turbulent part is integrated and the laminar part is neglected. This results in eq.(21b).

$$\overline{Nu_L} = 0.036 Pr^{1/3}\left(Re_L^{0.8} - 35768\right) \tag{21a}$$

$$\overline{Nu_L} = 0.036 Pr^{1/3} Re_L^{0.8} \tag{21b}$$

3.3.3 Analogy between heat and mass transfer

It is commonly known that a strong analogy exists between heat- and mass transfer. Although the driving force for mass and heat transfer is not the same, the formulas have the same form. Therefore, the same kind of relationship for mass transfer can be expected. In this case, the Schmidt and Sherwood number are used, so that the convective mass transfer coefficient can be determined. According to Sherwood [42] and Perry et al. [38] the dimensionless form of the local mass transfer coefficient (the local Sherwood number) can be described according to eq.(22a) and eq.(22b) for laminar and turbulent conditions, respectively. Performing the previous integration, but now for mass transfer results in eq.(22c). It can be seen that (20) and (22c) are almost identical. For high Reynolds numbers often only the turbulent part is integrated, resulting in eq.(22d).

$$Sh_x = 0.332 Re_x^{\frac{1}{2}} Sc^{\frac{1}{3}} \qquad (laminar) \tag{22a}$$

$$Sh_x = 0.0292 Re_x^{0.8} Sc^{0.43} \qquad (turbulent) \tag{22b}$$

$$\overline{Sh_L} = 0.036 Sc^{1/3}\left(Re_L^{0.8} - 35768\right) \qquad (average) \tag{22c}$$

$$\overline{Sh_L} = 0.036 Re_x^{0.8} Sc^{\frac{1}{3}} \qquad (average) \tag{22d}$$

3.3.4 Chilton-Colburn analogy

For some configurations data for mass transfer is not available, but data for heat transfer is. For the present case, the Chilton-Colburn Analogy may provide an estimation of the mass-transfer coefficient based on heat-transfer data. This analogy was found by Chilton and Colburn in 1934. This analogy relates heat, momentum and mass transfer, because the mechanisms and mathematics for transfer are closely related. The analogy is given by:

$$J_M = J_H = J_D \tag{23a}$$

$$\frac{f}{2} = \frac{\mathrm{Nu}}{\mathrm{RePr}^{\frac{1}{3}}} = \frac{\mathrm{Sh}}{\mathrm{ReSc}^{\frac{1}{3}}} \tag{23b}$$

$$\frac{f}{2} = \frac{h_s}{\rho c_p U_\infty} * \left(Pr^{\frac{2}{3}}\right) = \frac{h_m}{U_\infty}\left(Sc^{\frac{2}{3}}\right) \tag{23c}$$

In the formula above, J_M, J_H and J_D represent the J-factors for momentum, heat and mass, respectively. From this analogy the mass transfer coefficient can be determined using eq.(23c).

3.3.5 Low vs high mass-transfer theory

The theory for mass transfer is important in order to model the evaporation from the web. Especially when drying happens at high temperatures, different mass transfer mechanisms play a role. According to Mills [40], the absolute species flux can be written in terms of a sum of the absolute species fluxes as described in eq.(24a). Furthermore, applying conservation of mass on an elementary volume in which no chemical reaction occurs results in eq.(24b).

$$n_i = m_i \sum_{i=1,2,} n_i + j_i \tag{24a}$$

$$\frac{\partial \rho_i}{\partial t} = \boldsymbol{\nabla} \cdot n_i \tag{24b}$$

Where:

- n_i = absolute species flux (mass basis) of species i $\left[\frac{kg}{m^2 * s}\right]$
- m_i = mass fraction of species i $[-]$
- j_i = diffusive mass flux of species i $\left[\frac{kg}{m^2 * s}\right]$

Eq.(24a) can be divided into two parts: a convective component ($m_i * \sum n_i$) and a diffusive component (j_i).

3.3.5.1 Low mass transfer theory

In low mass transfer theory, it is assumed that there is no bulk movement: $\sum n_i = 0$. This means that the convective component is neglected and the absolute species flux is approximated by:

$$n_i = j_i \tag{25}$$

By assuming Fick's law of diffusion and a binary mixture, eq.(25) can be further expanded.

$$j_1 = -\rho D_{12} \nabla m_1 \tag{26}$$

The amount of mass diffusing from surface s to the surrounding e can be calculated using the mass transfer mass transfer coefficient h_m. Furthermore, one can assume that the total density of the mixture is constant if only a small mass fraction gradient exists. Therefore, eq.(26) reduces to:

$$j_{1,s} = h_m(\rho_{1,s} - \rho_{1,e}) \tag{27a}$$

$$n_{1,s} = h_m(\rho_{1,s} - \rho_{1,e}) \tag{27b}$$

3.3.5.2 High mass transfer theory

According to Mills [40], it is justified to neglect the convective part if the difference in the mass densities between the surface and its surroundings does not exceed $0.2\left[\frac{kg}{m^3}\right]$. Otherwise the convective part can not be neglected and high mass transfer theory should be used.
In the case of paper drying, it is assumed that two species exist in the gas phase: air and water vapour. For low mass transfer, which is based on equimolar counterdiffusion, it was assumed that $n_1 + n_2 = 0$. For high mass transfer theory, it can be assumed that the evapourated water is transported through a boundary layer of thickness L, in which the air is assumed to be stagnant. This unimolar diffusion results in $n_1 \neq 0, n_2 = 0$. For a one-dimensional problem, eq.(24a) can then be written as:

$$n_1 = -\frac{\rho D_{12}}{1-m_1}\frac{dm_1}{dz} \tag{28}$$

Eq.(28) can be substituted substituted in eq.(24b). By assuming steady state conditions in the boundary layer, eq.(29a) is obtained.

$$0 = \frac{d}{dz}\left(-\frac{\rho D_{12}}{1-m_1}\frac{dm_1}{dz}\right) \tag{29a}$$

$$z = 0, \quad m_1 = m_{1,s} \tag{29b}$$

$$z = 1, \quad m_1 = m_{1,e} \tag{29c}$$

Here $m_{1,s}$ and $m_{1,e}$ represent the mass fraction of species 1 just above the evapourating surface and outside the boundary layer, respectively.
By integrating eq.(29a) twice with the corresponding boundary conditions, a concentration profile is obtained:

$$\left(\frac{1-m_1}{1-m_{1,s}}\right) = \left(\frac{1-m_{1,e}}{1-m_{1,s}}\right)^{z/L} \tag{30}$$

By differentiating eq.(30) and evaluating at z=0, the evaporation rate at the surface of the paper is obtained:

$$n_{1,s} = \frac{\rho D_{12}}{L} ln\left(\frac{1-m_{1,e}}{1-m_{1,s}}\right) \tag{31}$$

In this case, L denotes the thickness of the boundary layer. By applying the ideal gas law and substituting the mass transfer coefficient, the evapourating rate can be expressed as:

$$n_{1,s} = \frac{h_m P_{tot}}{R_v T} ln\left(\frac{P_{tot} - P_{v,e}}{P_{tot} - P_{v,s}}\right) \tag{32}$$

$P_{v,s}$ and $P_{v,e}$ represent the vapour partial pressure of species 1 just above the evapourating surface and outside the boundary layer, respectively.

4 Transport phenomena in porous media

In this section, a detailed description will be given of the heat- and mass transport phenomena that play a role in paper drying. First, the structure of the paper web will be discussed. Then the drying processes and its drying phases will be described. Assumptions will be made in order to reduce the complexity of the mass and heat balance equations, so only essential transport mechanisms will remain. Thereafter, conservation of mass and energy equations will be set up and each term will be discussed.

4.1 Paper structure

Paper can be seen as a porous medium consisting of voids between solid particles. It has a complex structure consisting of cellulose fibres, water, air, fillers or other chemical additives. Its complex structure is created by a combination of successive processes. An elaborate description of all these processes is omitted in this work, but the two main process should be mentioned.
The first process is the pulping process. In this process the raw fibres are suspended into water. Several methods exist for the pulping process: mechanical pulping, chemical pulping or a combination of both. In mechanical pulping, shear force is used to produce heat in order to separate the cellulose fibres, lignin and hemicellusose. In chemical pulping, a solution separates the lignin and hemicellusose from the fibres, alternating its physical properties. The separation process of the lignin is also known as bleaching [22].
The second process is the dewatering or drying process. At the beginning of the dewatering process, liquid water is present in two forms: free water and bound water. Free water is located in the pores between the fibres (macro pores). In the macropores pores water can move freely and, thus, will be transported and evapourated first. The bound water is in micropores at the amorphous regions in the cell wall and in accessible hydrophilic groups [5]. As more water is evapourated from the paper web, the hygroscopic effect of the paper becomes visible. The hygroscopic effect can be explained as the natural tendency of the paper web to adsorb a certain amount of water under normal conditions. The hygroscopic effects are captured in sorption isotherms. These will be discussed in more detail in section 6.1. The range of moisture contents in which this effect becomes dominant is called the hygroscopic region. At moisture contents above the hygroscopic region the fibres are assumed to be fully saturated. Drying in the hygroscopic region results in water being evapourated from the micropores within the fibres. This will reduce the swollen state of the fibres, resulting in shrinkage of the paper web. The effect of drying on free- and bound water is depicted in figure 4.1.

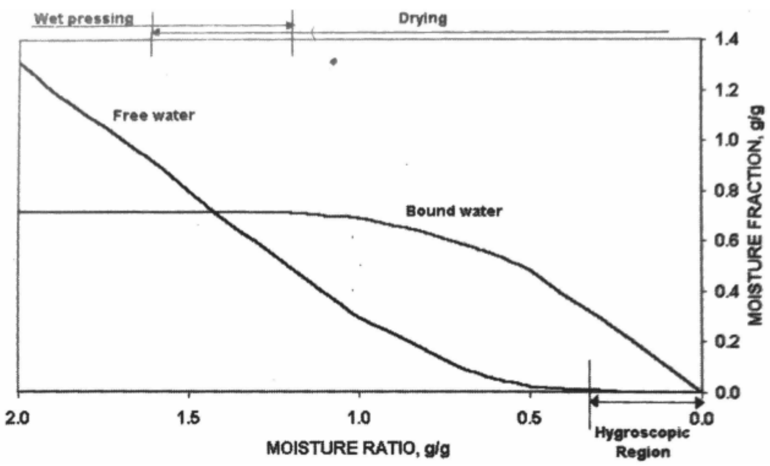

Figure 4.1: The effect of paper drying on free- and bound water. It can be seen that free water is removed first from the web, followed by bound water. [5]

The properties of the pores are essential in performing an accurate mass- and heat analysis. Permeability, porosity and flow of liquid water are all affected by the pore properties. It is impossible to fully describe the complete pore structure as this involves topology, pore dimensions, pore geometry, etc. Therefore, a common assumption is to treat the pores as cylindrical tubes [11]. Based on this assumption, the pore size distribution can be determined using several measurements techniques [43]: mercury intrusion, gas permeability, scanning electron microscopy, atomic force microscopy and light scattering. A detailed description of these measurement techniques will not be given in this report. However, applying data from these measurement techniques should be done with caution. The pore properties are significantly altered upon drying [43] and, therefore, this drying technique may provide inaccurate data for the drying process.

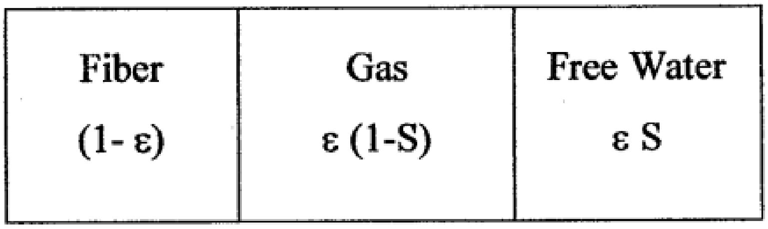

Figure 4.2: Volume fractions in the paper web. ϵ represents the total volume of the pores. S denotes the volumetric saturation of the pores.

In order to correlate properties used in the heat and mass balance, the volumetric saturation, S, is often used. By introducing the volumetric saturation, the paper web can be divided into three volume fractions (see figure 4.2). The moisture content of free water, M_{free} is related to the volumetric saturation, S, according to eq.(33). Notice that when the volumetric saturation is unity, the pores are entirely filled with water. When the saturation approaches zero, all the water is removed from the macropores and water is only present in bound form. Therefore, eq.(33) only represent the moisture content of free water located in the macropores.

$$M_{free} = \frac{S\epsilon\rho_w}{(1-\epsilon)\rho_f} \tag{33}$$

The moisture content can be described as function of the dry basis weight and moisture content. The dry basis weight is described as the mass of dry material (i.e. fibres) per squared meter. Therefore, dry basis weight can be described as:

$$\frac{b_{wt}}{L} = (1-\epsilon)\rho_f \tag{34}$$

Here, b_{wt} is the dry-basis weight in $\left[\frac{kg_{fibre}}{m^2}\right]$ and L the thickness of the paper sheet. The dry-basis moisture content of free water can then be calculated as:

$$M_{free} = \frac{S\rho_L\epsilon L}{b_{wt}} \tag{35}$$

In studies found in the literature, many have used pore size distribution functions to relate the volumetric saturation to the largest radius of the liquid water-filled macropores. In this way, the capillary pressure and relative permeability can be expressed as a function of the moisture content. The procedure for determining the volumetric saturation from a pore size distribution function is explained in appendix (A.8).

4.2 Drying process

A continuous drying process can be divided into three phases: the heating phase, the constant drying phase and the falling phase [2] [5] [32]. These phases are depicted in figure 4.3 and will be discussed below. It is important to note that drying phases in industrial drying are more complex. In this case, large gradients in the moisture content and the temperature are present in the thickness direction. Therefore, averaging the moisture content and the temperature is not justified. The constant heating phase may not be present in a dryer section, because of changing external conditions. Furthermore, the onset of each phase is not clear, due to large gradients in the sheet.

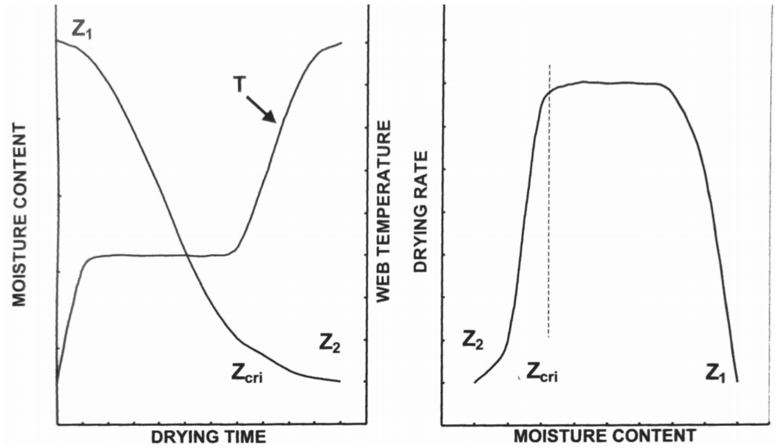

Figure 4.3: Different drying phases in continuous drying. Z_1 represents the start of the drying process and Z_2 is the end of the drying process. [5]

4.2.1 Heating phase

In this phase, heat is supplied to the sheet and the sheet temperature increases. As can be seen in figure 4.3, the drying rate will increase as well. Within this phase, only a small amount of water is evapourated.

4.2.2 Constant heating phase

After the heating a phase, a constant phase is reached. In this constant phase the temperature and the drying rate remain constant. At this point, the energy consumption for vapourizing the water is in equilibrium with the energy supplied to the web. During the constant drying phase, capillary forces can transport free water to the surface of the paper web. This phase can be compared to evaporation from a free water surface, where drying takes place as rapidly as water vapour can diffuse from the surface into the air stream [44]. Besides evaporation from a free water surface, also evaporation below the water surface occurs. Up to this point, this does not have to be captured, as the total amount of evapourated water can be described by evaporation from a free water surface.
There exists a point at the end of the constant drying phase, however, where the evaporation from the web is not dictated by the rate of evaporation from a free water surface anymore. At this point, the resistance of vapour diffusion and capillary transport will dictate how much water evapourates from the web. This point is known as the critical moisture content (CMC) [45] [5] [44]. This inversion point is the start of the falling drying phase.

4.2.3 Falling rate phase

In the falling rate phase, the transport properties of the paper web will dictate how much can be evapourated from the web. The falling rate phase can be divided into two sections, due to the hygroscopic nature of the paper web. Belhamri [45] describes the phases as the first falling period and the second falling period. Before discussing those phases, the onset of the hygroscopic region needs adressing first.

4.2.3.1 The onset of the hygroscopic region

To account for the sorptive effects, it is important to define the onset of the hygroscopic region. As can be seen in figure 4.3, there is no discontinuity at the start of the hygroscopic region, but a smooth transition. The onset of the hygroscopic region, therefore, represents a moisture content at which the hygroscopic effects become significant. In the literature several indicators have been used to describe this point:

- The equilibrium moisture content (EMC) is defined as the moisture content at which an initially dry material is in equilibrium with its surrounding at 100% relative humidity.

- A more relevant parameter describing the onset of the hygroscopic region of the paper web is the fibre saturation point (FSP). In paper drying, the FSP denotes the moisture content in which all the water in the macro pores has been removed, but the fibres itself remain fully saturated. Therefore, this point indicates the amount of bound water present in the sheet.
- The CMC represents the moisture content from which the drying rate is dictated by internal heat and mass transfer instead of evaporation from a free water surface. Sometimes this parameter is used to represent the onset of the hygroscopic region. However, this parameter is a function based on the heat and mass transport mechanisms rather than paper properties. Therefore, it is heavily dependant on the drying conditions, resulting in different values for each dryer section.
- The irreducible moisture content (IMC) is often used in drainage experiments to represent the start of the hygroscopic region. This moisture content represents the point where the capillary pressure goes asymptotically to infinity. In other words, increasing the capillary pressure at this moisture content will not cause any flow of water. According to Sadeghi [22], the IMC is heavily dependant on the experimental conditions and, therefore, not a good indicator for the onset of the hygroscopic region.

By using the FSP as indicator for the hygroscopic region and assuming that capillary flow ceases at the onset of hygroscopic region, only free water is available for capillary transport. Therefore, the FSP is used to indicate the onset of the hygroscopic region.

4.2.3.2 First falling period

As described above the first falling period starts at the CMC, where the internal transport properties of the paper web dictated the amount of evaporation from the web. In the first falling period, Comings [44] reports a linear decrease in the drying rate, based on early works of Sherwood. At this point, internal transport can still provide free water to the surface of the paper web, but with a decreasing rate.

4.2.3.3 Second falling period

Once the sorptive effect becomes significant, the first falling period is considered to be over. By assuming the FSP as the onset of the hygroscopic region, it is assumed that only bound water is left. If enough heat is supplied, the second falling period starts. In this case, there is only bound water left. Bound water can be transported in liquid or gaseous state to the surface of the web. The sorptive effects cause a reduction in vapour partial pressure, reducing the driving force for removing the water from the web. By using a sorption isotherm for each specific paper grade, this reduction can be described. Due to the adhesive forces of the water molecules, additional heat needs to be supplied to evapourate the bound water. This additional heat is referred to as the heat of sorption and will be discussed along with sorption isotherms in more detail in section 6.1.3.

4.3 Drying phases in multicylinder drying

According to Reardon [11] and Sadeghi [22], Nissan and Kaye ([46], [47], [48]) were the pioneers in describing multicylinder drying. They distinguished four phases of drying occurring in cylinder drying in a two-tier double-felted configuration. The phases are shown in figure 4.4. Most modern drying models are based on these four phases, which will be described below (following Karlsson [5]).

4.3.1 Drying phases in two-tier double-felted configuration

The four phases of drying in a two-tier double-felted configuration are the following:

A-B: One side of the paper web is heated by the cylinder, while the other side faces the pocket air. The drying rate is low, as the paper web needs to be heated first. At the point where the felt meets the paper, the drying rate is slightly reduced.

B-C: The paper web is squeezed between the felt and the cylinder. The web is heated along the whole length, until the paper web reaches its hottest point (point C). The drying rate is increased only slightly, because the felt offers extra resistance to the evaporation.

C-D: One side of the sheet is still heated by the cylinder, while the other side is open for evaporation. Therefore, a jump in drying rate can be seen in figure 4.4c.

D-E: The paper web faces the pocket air at both sides, offering great potential for evaporation. At point D, the temperature of the paper web is still high, causing a lot of evaporation. When the paper web reaches the next cylinder (Point E) the temperature has decreased by a significant amount, resulting in less evaporation.

4.3.2 Drying phases in single-tier single-felted configuration

The four phases of drying in a single-tier single-felted configuration are the following:

A-B: The paper web is squeezed between the felt and the cylinder. The web is heated along the whole length, until the paper web reaches its hottest point (point B). The drying rate is increased only slightly, because the fabric offers extra resistance to evaporation.

B-C: One side of the paper web faces the pocket air, while the other side is continuously supported by the felt. Since one side is open for evaporation, there is a jump in the drying rate. This drying rate is enhanced by the use of permeable fabric and blow boxes.

C-D: The supporting felt is squeezed between the turning role and the paper web, leaving one side of the paper web open for evaporation. This results in only a slight drop in drying rate over the length of the turning role.

D-E: One side of the paper web faces the pocket air, while the other side is continuously supported by the felt. In this case, the turning role does not heat the web, so the drying rate over this section is only small.

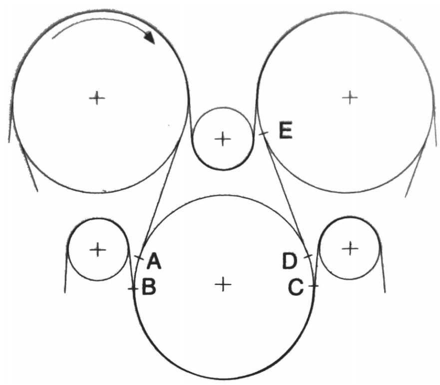

(a) Location of four phases of drying in two-tier double-felted configuration.

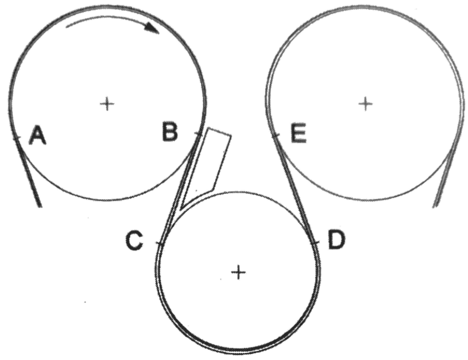

(b) Location of four phases in drying in single-tier single-felted configuration.

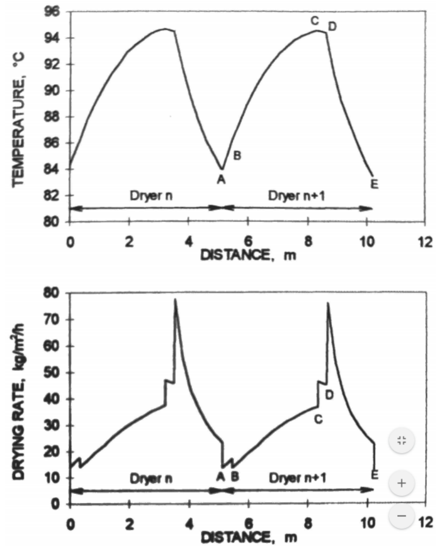

(c) Drying rate for 4 phases in drying in double-tier double-felted configuration.

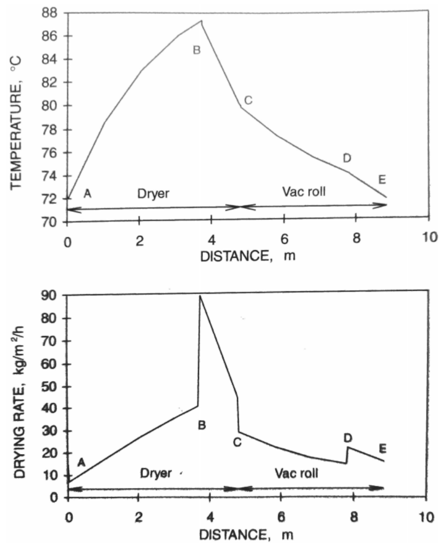

(d) Drying rate for four phases in drying in single-tier single-felted configuration.

Figure 4.4: Different phases in multicylinder drying. On the left four phases in a two-tier double-felted configuration is shown. On the right, four phases in a single-tier single-felted configuration are shown [5].

5 Model development

In this thesis, the focus will be on constructing a model for multicylinder drying of a continuous paper web. The model is meant to determine the moisture content and the temperature profile in the paper thickness direction, while the paper web is transported over the drying cylinders.
First, a literature review on paper drying modeling is given. Secondly, the assumptions made will be discussed. Next, the conservation laws of mass and energy will be analyzed. Two separate conservation equations will be constructed: one for the moisture content and one for the temperature. These equations will be constructed using the assumptions made.

5.1 Literature on paper drying modeling

Modelling the dryer section started in the 1950s and a large number of studies have been dedicated to this subject since then. In this literature review only the relevant works will be included.
Nissan and Kaye [46] were among the first to make a significant contribution to paper drying modeling. They distinguished the four phases in drying as mentioned in figure 4.4. In this model transportation of water from the web to the felt was under serious investigation, because it was unclear if liquid water was absorbed by the cloth or transported by means of water vapour. Although this model was very limited, it formed the basis for several other models. Depoy [49] extended the work of Nissan and Kaye by including three zones of drying in a dryer section: heating zone, constant zone and the falling zone. Depoy [49] used mass transfer coefficients to calculate the moisture removal from the sheet to study both traditional dense absorbing felts and modern open synthetic felts. Drying rates for the open felt were reported to be much larger compared to the traditional felt.
However, the limited model of Nissan and Kaye did not include internal transport mechanisms. Han [50] was the pioneer to describe the paper drying process by analyzing internal heat and mass transfer. This author noticed that the wide range of pore sizes was causing capillary movement. The model included liquid movement in the early stages of drying following Darcy's law and vapour movement based on Fick's law. Hartley and Richards [51] also used internal transport mechanisms to describe the drying process. They noticed the presence of the capillary forces; however, they did not include this effect in their model.
In the 1980s, the need to capture the internal transport phenomena was recognized by several research groups. Lee and Hinds [52] noticed that internal mass and heat transfer occurs primarily because of capillary pressure differentials in the early stages of drying. However, Lee and Hinds did not account for internal transport phenomena according to Reardon [11]. According to Sadeghi [22] and Ma [53], Lee and Hinds determined the coefficients for heat and mass transport from and to the paper web experimentally for several paper grades. They performed simulations for several paper machines producing different paper grades. By tuning the simulation for a specific paper grade and paper machine, a normalized simulation was constructed. In this way different paper machines and paper grades could be compared. For lightweight paper grade, the results were in good agreement with the data, but for heavier grades, the simulation was inaccurate. This illustrates the importance of capturing internal heat ans mass transfer. In a later paper, Hinds and Neogi [54] used the Chilton-Colburn analogy to update the boundary conditions and applied sorption isotherm formulated by Prahl [13] to capture sorptive effects.
Karlsson and Soininen [15] also recognised the effects of the capillary transport mechanism, but only assumed diffusion as a transfer mechanism. They related the porosity and tortuosity to the diffusivity of the paper web and used Prahl's data for constructing the sorption isotherm. Karlsson and Paltakari [55] continued the work an emphasized that internal processes must be taken into account for heavier paper grades.
In 1990, Harrmann and Schulz [56] constructed an elaborate model on convective paper drying. They noticed that water influenced the sheet structure and incorporated this in their model. According to Reardon [11], their model took into account the effects of sorption, shrinkage and pressure-driven liquid flow.
Based on earlier works of Han (1964), Ramaswamy [24] constructed a very comprehensive model. Besides the capillary liquid transport and the diffusive vapour transport, Ramaswamy incorporated

the effects of pressure-driven vapour flow, once the pressure exceeded the atmospheric pressure. The model could only be used to a limited extend for a couple of reasons. Firstly, it was specifically designed for linerboard. Secondly, no variation in pocket conditions could be simulated and, thirdly, the felt was not taken into account.
In 1994, Reardon [11] presented a model that accounted for capillary action, the vapour diffusion and convective transport. However, the major drawback of this model is that Reardon assumed also the bound water to be transported by capillary action. In addition, Reardon did not take into account the effect of air, and assumed vapour to be the only species in the gas phase.
In the end of the 1990s, several simulators were designed to simulate the behaviour of the paper during the drying section. In 1996 Wilhelmsson et al. [57] applied their simulator to nine different dryer sections. Accurate values were reported only for lightweight grades, because no internal transport phenomena were taken into account.
An even more advanced model was developed by Bond et al. [58] and this was developed further by Sidwall [59] [60]. In the first version of the model, Bond et al. considered internal heat and mass transfer mechanisms, which were diffusion-based. Sidwall extended the model by applying the applicable boundary conditions and external transport phenomena. Sidwall also extensively validated the model against several paper drying machines and laboratory tested. The model showed good agreement with the laboratory tests. However, when the model was compared to actual paper drying machines, the model underpredicted the amount of evapourated water. According to Sadeghi [22], this was probably because the internal transport mechanisms were simplified and the equations only captured diffusion-based terms.
Stenström [33] reviewed the literature of paper drying between 2000 and 2018, and reported no major changes in the technology of paper drying and its modeling. According to Strenström [33] there were several publications in the field of paper drying modeling. Karlsson et al. [61] [62] developed a dynamic model to simulate the capacity and quality. Furthermore, Strenström [33] reported two more models that included heat and mass transfer: Reardon [63] presented a model for drying two newsprint papers and Sadeghi [22] constructed a model for industrial paper drying and validated it against 12 different dryer sections. Reardon's model solved a heat and mass balance for water without accounting for the hygroscopic region. Both models proposed by Reardon [11] and Sadeghi [22] proposed 4 boundary conditions per side. In section 8 it is shown that these are contradicting.
Several other models were reported by Strenström [33] that did not capture the effect of internal transport mechanisms. The importance of capturing these mechanisms has been stated several times and, therefore, these models can be ignored.

Up to this point, there has been no clear mentioning of paper drying models that can accurately describe the drying process for heavier grade materials. In the present Master thesis study a model will be developed that aims at overcoming these shortcomings. This means that convection- and diffusion-based internal transport phenomena need to be captured for both the liquid phase and the gas phase. Furthermore, a set of appropriate non-contradicting boundary conditions needs to be formulated.

5.2 Assumptions

In most modeling cases it is almost impossible to fully describe the behaviour of a system. This is also the case in paper drying. Due to the complexity and the anisotropic properties of its structure, it is practically impossible to model the transport phenomena at microscopic level (i.e. pore level). Instead, this model will be based on macroscopic transfer equations. These macroscopic transfer equations are based on a continuum model. In a continuum model, volume averaging is applied over a representative elementary volume (REV), which may contain many pores in each coordinate direction [9]. The parameters (like diffusivity, porosity, thermal conductivity, etc.) are the averages of the microscopic properties within the REV. By deriving the conservation equations at macroscopic level, there is some loss in structural information. This is a direct consequence of averaging over a REV. However, in this way a reduction in computational capacity is achieved. Capturing only essential structural information allows a fairly accurate model to be constructed, while keeping the required

computational capacity to a minimum.
The assumptions mentioned above are based on structural properties. A list of other assumptions is presented below:

1. **No gravitational influence on transport mechanisms.**
   [1], [11], [24] and [22] all neglect gravitational effects. Asensio [1] found that the gravimetric pressure contribution to water transport would only be a few Pascal, while the capillary pressure contribution was estimated to be 10 kPa.

2. **Only transport in the thickness direction of the paper is considered.**
   In this case, the model is reduced to a 1D heat and mass transfer problem. In reality, capillary transport and diffusion occur in the plane of the sheet. However, the transport mechanisms in the thickness direction are assumed to be orders of magnitude larger.

3. **No energy accumulation or dissipation.**
   Upon drying, the fibres might deform, resulting in accumulation of energy. In addition, viscous dissipation effects are present during the flow of water (vapour) through the paper web. Both are considered to be negligible.

4. **Thermodynamic equilibrium at each REV point in the paper web.**
   The different phases in a REV point are considered to be in thermodynamic equilibrium. Therefore, the temperature of each phase is in equilibrium [22].

5. **The gas phase is assumed to be saturated with water vapour.**
   Therefore, the vapour pressure at each REV point can be directly related to its temperature.

6. **Free water is transported according to Darcy's law.**
   A pressure difference within the liquid water causes the water to move. The capillary pressure causes this pressure difference. This will be explained in more detail in section 5.4.1.

7. **Transport of bound water is negligible.**
   Bound water starts to evapourate from the web once free water is evapourated. Reardon [11] and Ramaswamy [24] also neglect the effects of moving bound water.

8. **The gas phase consists of two ideal gasses: water vapour and dry air**
   The operating conditions will be at relative low pressures and low temperatures, validating the use of the ideal gas law.

9. **The minimum total gas phase pressure in the sheet is the atmospheric pressure.**

10. **A fixed minimum partial pressure of dry air exists.**
    Combining this assumption with assumption 9, the total pressure of the gas phase can be described at every location in the sheet. In this way, the need for an extra mass balance is omitted, while maintaining the ability to describe pressure differentials in the gas phase. Reardon [11] made the same assumption.

11. **Water vapour is transported through diffusion and a possible pressure gradient.**
    Two vapour transport mechanisms may occur in the voids of the web. If the total pressure of the gas phase is below atmospheric pressure vapour transport will take place by diffusion. If a pressure build-up occurs in the sheet, vapour is also transported by a pressure-driven Darcy flow.

12. **No chemical reactions occur**
    The interaction of the liquid water, water vapour or paper web will not be based on chemical reactions. This simplifies the mass balance.

5.3 Conservation of mass

The conservation of mass will be applied to a REV. This representative elemenatry volume can be subdivided into three fractions as shown in figure 4.2. Here, ϵ is the void volume fraction (porosity) and S is the void fraction filled with free water (volumetric saturation). As described before, the moisture content and the volumetric saturation are correlated according to eq.(33).

5.3.1 Conservation of water

Three states of water can be found inside the web: free water, bound water and water vapour. Taking assumption 7 into account, only free water and water vapour contribute to water movement. They occupy a volume fraction ϵS and $\epsilon(1-S)$, respectively (see figure 4.2).
There continuity equations can be written as:

$$\frac{\partial(\epsilon S \rho_{free})}{\partial t} + \nabla \cdot n_{free} = \dot{m}_{free} \tag{36a}$$

$$\frac{\partial(\epsilon(1-S)\rho_v)}{\partial t} + \nabla \cdot n_v = \dot{m}_v \tag{36b}$$

$\dot{m}_{free}$ and $\dot{m}_v$ can be considered as sink and source terms, respectively. They are representing the evaporation. Taking assumption 12 into account, the sum of these terms should be equal to zero: the amount that leaves the liquid state is added to the vapour state.

$$\dot{m}_{free} + \dot{m}_v = 0 \tag{37a}$$

$$\frac{\partial(\epsilon S \rho_{free}) + (\epsilon(1-S)\rho_v))}{\partial t} + \nabla \cdot [n_{free} + n_v] = 0 \tag{37b}$$

Substituting eq.(33) into eq.(37b) leads to the conservation of mass equation for water. In this conservation equation, a constant density of the fibres and homogeneity is assumed throughout the drying process.

$$(1-\epsilon)\rho_f \frac{\partial M}{\partial t} = -\nabla \cdot [n_{free} + n_v] \tag{38}$$

5.3.2 Conservation of air

In the gas phase two species contribute to the transport: air and water vapour. In order to fully describe the movement of the gas phase, two conservation equations should be constructed: one for air and one for water vapour. However, in the present study the use of a separate conservation equation for air is omitted by using assumptions 9 and 10.
At low vapour partial pressure, a constant atmospheric pressure is assumed in the sheet, disabling the pressure-driven flows. However, at high temperatures, the partial pressure of vapour may approach the atmospheric pressure, resulting in pressure-driven flows. In this case, a minimum fixed vapour partial pressure is required in order to use eq.(32).
Assumptions 9 and 10 can also be formulated mathematically:

$$P_{tot} = \begin{cases} P_{atm} & \text{, if } P_v + P_{a,fixed} < P_{atm} \\ P_v + P_{a,fixed} & \text{, otherwise} \end{cases} \tag{39}$$

In order to find the most applicable value for $P_{a,fixed}$, two values (0.1 and 0.01 $[kPa]$) will be evaluated in the sensitivity analysis performed in section 9.

5.4 Mass flux terms

In order to solve eq.(38), the terms on the right hand side should be expanded. The first term on the right hand side of eq.(38), n_{free}, identifies the movement of free water. By applying assumption (6), this term can be expanded. The second term on the right hand side, n_v, can be expanded by assumption (11). This means that n_v should be expanded into two terms: one term represents the diffusive flow and the other term represents the bulk flow of vapour. It is enabled if the total gas phase pressure exceeds the atmospheric pressure in the sheet (see assumptions 9 and 10).

5.4.1 Capillary pressure

As described before, the structure of the paper web will be modeled as a set of capillaries of different sizes. In order to obtain an accurate model, the capillary action must be taken into account. In our case, the capillary pressure causes the pressure difference between liquid water and moist air inside the capillaries. In a capillary tube, partly filled with air and water, the water molecules tend to adhere to the solid fibres. This phenomenon is called the wettability. The result of this adhesion is a curved water-air interface, i.e. a meniscus.
The differential pressure between the liquid and moist air can be described by the Young-Laplace equation:

$$\Delta P = -\gamma \left(\frac{1}{R_1} + \frac{1}{R_2} \right) \tag{40a}$$

$$= \frac{-2\gamma}{R} \qquad (R_1 = R_2) \tag{40b}$$

Where:

- ΔP = Laplace pressure $[Pa]$
- γ = Surface tension $[\frac{N}{m}]$
- R = Principal radius of curvature $[m]$

Note that in these equations the radii of curvature do not correspond with the radius of the tube. The radius of curvature can be related to the radius of the capillary tube, r, using figure 5.1 and the following equation:

$$R = \frac{r}{\cos\theta} \tag{41}$$

Therefore, eq.(40b) can be written as:

$$\Delta P = \frac{-2\gamma\cos\theta}{r} \tag{42}$$

It is assumed that capillaries with a tapered end exist. This explains the variety of pore radii. Therefore, the capillary theory should be extended to capillaries with tapered ends (see figure 5.2). In this case a pressure gradient is present between the left and right side. A similar total gas phase pressure is assumed at both sides. The capillary pressure can also be written as:

$$P_{tot} = P_w + P_c \tag{43}$$

Here the subscripts P_{tot}, P_l and P_c denote the gas, liquid and capillary pressure, respectively. Assuming equal total gas phase pressures at both sides leads to:

$$P_{tot,\,(1)} = P_{tot,\,(2)} \tag{44a}$$

$$P_{w,\,(1)} + P_{c,\,(1)} = P_{w,\,(2)} + P_{c,\,(2)} \tag{44b}$$

$$P_{w,\,(1)} - P_{w,\,(2)} = P_{c,\,(2)} - P_{c,\,(1)} \tag{44c}$$

$$P_{w,\,(1)} - P_{w,\,(2)} = \frac{2\gamma\cos(\theta_2+\phi)}{r_2} - \frac{2\gamma\cos(\theta_1+\phi)}{r_1} \tag{44d}$$

Due to the larger radius of curvature on the left side, the capillary pressure will be lower on the left side. If an equal total gas phase pressure is assumed on both sides, the liquid pressure on the left side must exceed the liquid pressure on the right side. This effect will cause capillary flow from the left to the right as indicated in figure 5.2. This pressure gradient will be the driving force for the transportation of free water.

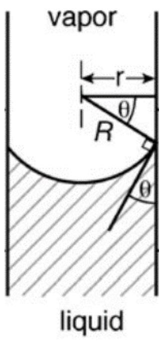

Figure 5.1: Relation between the radius of curvature and the radius of capillary tube. [8]

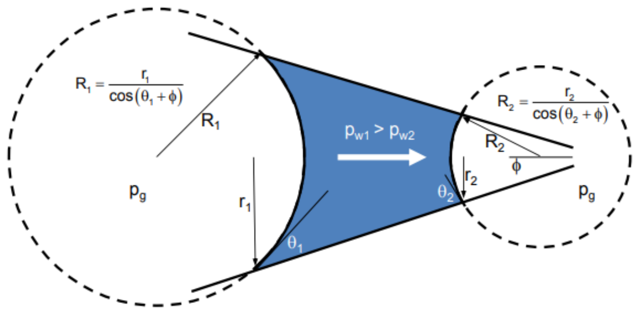

Figure 5.2: Capillary pumping in a small slightly tapered tube. [9]

5.4.2 Capillary pressure functions

5.4.2.1 Capillary pressure based on pore size distribution

Eq.(42) relates the largest pore size filled with liquid water to the capillary pressure. In appendix A.8 the maximum pore size filled with moist is related to the moisture content in the paper sheet. By combining these relations it is possible to relate the moisture content to the capillary pressure. This formulation is omitted here, but can be found in appendix A.9

5.4.2.2 Capillary pressure based on experiments (without furnish dependency)

It can be difficult to find the pore size distribution of a porous structure. Therefore, there can be a significant uncertainty in the derived capillary pressure curves. Moreover, the angle of contact, θ, cannot be measured. In the derivation given above, this contact angle is set to 0°. Although this assumption was made by Reardon [11], its validity is questionable. Therefore, the capillary pressure-saturation relations are often determined experimentally and illustrated using capillary pressure curves, like the one depicted in figure 5.3. In this figure, two curves can be distinguished. The upper and lower curves represent drainage and imbibition, respectively. Drainage can be defined as the process where the wetting phase (liquid water in this case) is replaced by the non-wetting phase (moist air in this case). For a fixed saturation, imbibition happens at a lower capillary pressure, because the wetting fluid tends to adhere better to the solid structure. The wetting solids pulls itself through the solid structure, replacing the non-wetting phase. This behaviour is called hysteresis. In the case of imbibition the solid structure cannot be fully saturated as the non-wetting phase becomes trapped in voids within the structure. For the drainage case, the capillary pressure approaches infinity at the irreducible saturation or irreducible moisture content (IMC). This saturation represents the amount of water that cannot be removed by capillary forces. In this study, the focus will be on drainage curves as we remove water from the paper web.
Numerous experimental studies can be found in the literature on the relation between the saturation and the capillary pressure. Brooks and Corey [10] presented the following correlations:

$$P_c = P_e(S_{tot}^*)^{\frac{1}{\lambda}} \tag{45a}$$

$$S_{tot}^* = \frac{S_{tot} - S_r}{1 - S_r} \tag{45b}$$

$$S_{tot} = \frac{M(1-\epsilon)\rho_f}{\epsilon\rho_L} \tag{45c}$$

$$S_r = \frac{M_r(1-\epsilon)\rho_f}{\epsilon\rho_L} \tag{45d}$$

Where:

- P_c = Capillary pressure. $[kPa]$

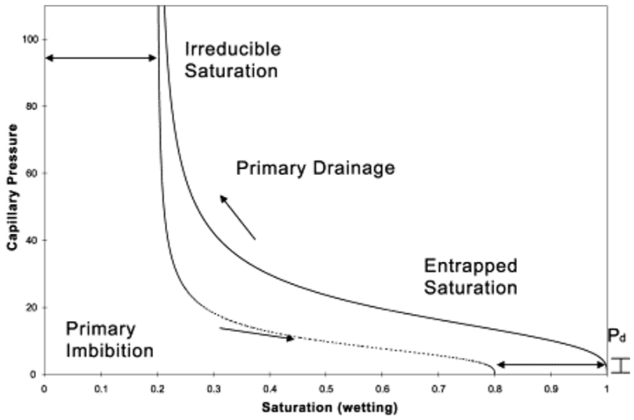

Figure 5.3: Typical capillary pressure curves.

- P_e = Entry capillary pressure. $[kPa]$
- S^* = Normalized wetting phase saturation. [-]
- λ = Pore size distribution index. [-]
- S_r = Residual wetting phase saturation. [-]

The entry capillary pressure,P_e, can be defined as the minimum pressure that needs to be overcome in order to replace the wetting phase with the non-wetting phase. The residual wetting phase saturation,S_r, is the saturation that cannot be removed for increasing capillary pressure. At this saturation, the movement of liquid water resulting from capillary forces ceases. In the present thesis project, the fibre saturation point is assumed to represent this point. Spolek and Plumb [64] performed a series of experiments involving the drying of softwood fibres. They reported average values of 12.4 $[kPa]$ for the entry capillary pressure and -1.64 for the pore size distribution index.

5.4.2.3 Capillary pressure based on experiments (with furnish dependency)

Asensio [1] also included the furnish dependency in her capillary pressure curves. Six types of paper types were investigated and the following relations for the capillary pressure were proposed depending on the temperature and the furnish type:

$$P_c = c\left(\frac{b}{M - M_{irr}} - 1\right)^{\frac{1}{d}} \tag{46a}$$

$$P_c = \frac{c}{b}\left(\frac{b}{M - M_{irr}} - 1\right) \tag{46b}$$

Asensio used the irreducible moisture content as the point beyond which capillary flow ceases. The irreducible moisture content is based on experiments and it is heavily dependent on the experimental conditions. Therefore, the FSP is used instead. By using the FSP, there is a clear distinction between free water, which can move by capillary forces, and bound water, which cannot move by capillary forces [22]. The coefficients applicable to each furnish type can be found in appendix A.10.

5.4.2.4 Concluding remarks on capillary pressure correlations

Numerous capillary pressure correlations have been proposed in the literature. In the present study the capillary pressure functions based on pore size distributions will not be used, because there is hardly any information available on pore size distributions. Instead capillary pressure curves based on experiments will be used in this model.

In figure 5.4 three capillary curves are shown as function of the free water moisture content: one furnish-independent correlation proposed by Brooks and Corey [10] and two furnish-dependent correlations proposed by Asensio [1]. Although Asensio investigated several different furnish types, only two are comparable to the furnish type investigated in the field survey. As can be seen in figure 5.4, the correlation proposed by Brooks and Corey agrees relatively well with the correlation proposed by Asensio for the northern softwood kraft (NSWK) furnish type. The correlation for the eucalyptus furnish type differs slightly from the others. Therefore, is was chosen to include Brooks and Corey's correlation and Asensio's correlation for eucalyptus in the sensitivity analysis.

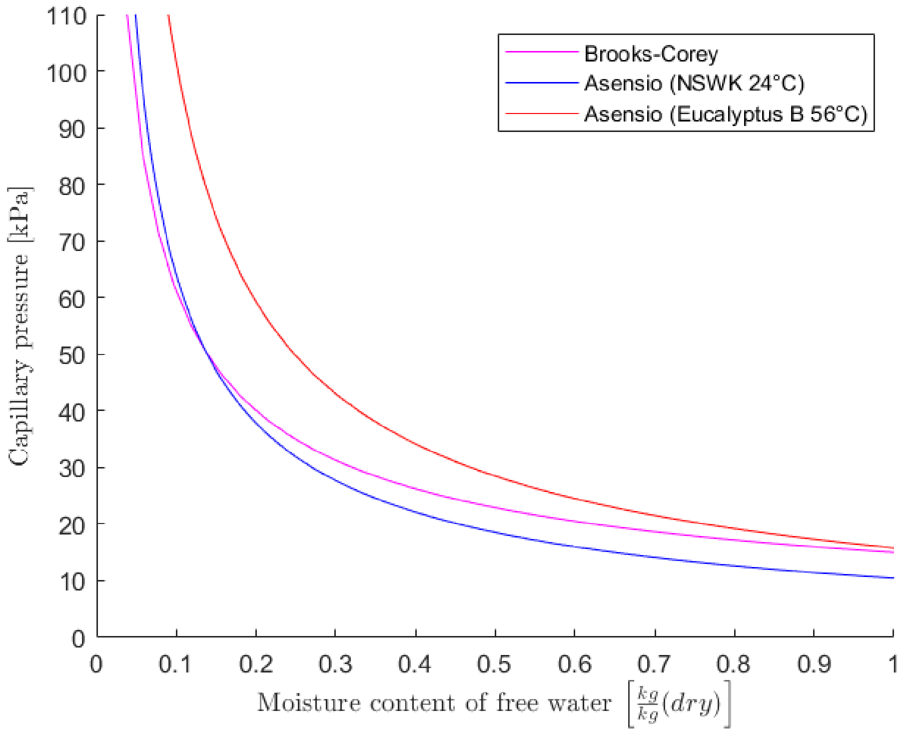

Figure 5.4: Capillary pressure curves proposed by Brooks and Corey [10] and Asensio [1] as function of the free-water moisture content.

5.4.3 Capillary flow of free water

Assumption 6 states that transportation of free water follows Darcy's law:

$$v_{free} = -\frac{K}{\mu}\left(\nabla P - \rho g\right) \tag{47}$$

This equation is valid for single phase flow in a saturated homogeneous porous medium, where the permeability is independent of the position [22]. By applying assumption 1, the gravity term can be neglected. Furthermore, it is assumed that no pressure gradient exists other than in the thickness direction. This pressure gradient denotes the pressure gradient within the liquid phase, P_L.
As described above, eq.(47) is valid for a single phase flow through a porous medium. However, in this case two-phase flow occurs: flow of liquid water and vapour flow. The flow of the second phase can hinder the transportation of the first phase and vice versa. The amount of resistance that a phase experiences is heavily dependent on the amount of saturation of that phase. In order to account for this, dimensionless relative permeabilities are introduced: k_w and k_{nw}. The subscripts w and nw denote the relative permeabilities of the wetting and the non-wetting phase, respectively. For capillary flow k_w is used, because liquid water represents the wetting phase.
Therefore, eq.(47) can be written as:

$$v_{free} = -\frac{k_w K}{\mu}\left(\frac{\partial P_L}{\partial y}\right) \tag{48}$$

The first term on the right side of eq. (38) represents the mass flow of free water through the sides of a REV:

$$n_{free} = \rho_{free} v_{free} \tag{49}$$

Substituting eq.(48) results into:

$$n_{free} = -\frac{k_w K}{\nu_w}\left(\frac{\partial P_L}{\partial y}\right) \tag{50}$$

P_L can be expanded using eq.(43). Therefore, eq.(50) can be rewritten as:

$$n_{free} = -\frac{k_w K}{\nu_w}\left(\frac{\partial(P_{tot} - P_c)}{\partial y}\right) \tag{51}$$

5.4.4 Vapour flow

vapour is transported through diffusion and possibly by a pressure-driven flow (see assumption 11).The transportation of vapour through the sides of a REV can be described as:

$$n_v = \rho_v v_g + J_v \tag{52}$$

5.4.4.1 Pressure-driven bulk vapour flow

Once the paper web has sufficiently dried, evaporation will occur mostly inside the web. If the rate of diffussive transportation cannot keep up with the rate of evaporation, a pressure build-up may occur inside the web. This pressure build-up causes a pressure-driven flow for the gas phase. This flow can also be described as Darcy flow. The same reasoning for the relative permeability term applies, but now for the non-wetting phase. Again, the pressure gradient (for the total gas phase pressure, in this case) only occurs in the thickness direction of the paper. Therefore, eq.(47) can be modified to:

$$v_g = -\frac{k_{nw} K}{\mu_g}\left(\frac{\partial P_g}{\partial y}\right) \tag{53}$$

5.4.4.2 Sorptive effects

Once the fibre saturation point is reached, the hygroscopic effects of the paper web become significant. Bound water tends to remain absorbed onto the paper, causing a decrease in the vapour partial pressure. This phenomenon is known as the Kelvin effect. An accurate description of the Kelvin effect is given in appendix A.11. The Kelvin effect depends on the largest pore radii filled with liquid water, making it hard to implement.

The reduction of the vapour partial pressure can also be described by an experimentally-determined relative humidity of air, ϕ. This term depends on the temperature and moisture content. It is defined as:

$$P_v(M,T) = P_v^{'}(T)\phi(M,T) \tag{54}$$

Sorption isotherms are constructed to indicate the relative humidity of air as a function of the moisture content at constant temperatures. Sorptive effects and sorption isotherms will be discussed in more detail in section 6.1.

5.4.5 Diffusive vapour flow

In the present study, vapour diffusion is assumed to follow Fick's law. The same assumption was made by Reardon [11], Sadeghi [22] and several others. Perry et al. [38] define the mass flux with respect to the mass average velocity as:

$$J_v = -\rho_g D_{eff}\frac{\partial m_v}{\partial y} \tag{55}$$

Note that in this equation m_v represents the vapour mass fraction $\left(\frac{\rho_v}{\rho_g}\right)$. D_{eff} represents the effective diffusivity and will be explained in section 6.3 in more detail. By using assumption 8, the ideal gas law can be used to write the densities as partial pressures.

5.4.6 Final mass balance

The original mass balance is derived in eq.(38). By substitution of eq.(51),(52) and (53) into eq.(38), the final mass balance is obtained:

$$(1-\epsilon)\rho_{fibres}\frac{\partial M}{\partial t} = \begin{cases} -\boldsymbol{\nabla}\cdot\left[\frac{k_w K}{\nu_w}\left(\frac{\partial P_c}{\partial y}\right) - \rho_g D_{eff}\left(\frac{\partial m_v}{\partial y}\right) - \frac{\rho_v k_{nw} K}{\mu_g}\left(\frac{\partial P_v \phi}{\partial y}\right)\right] & \text{, if } P_v > P_{atm} \\ -\boldsymbol{\nabla}\cdot\left[\frac{k_w K}{\nu_w}\left(\frac{\partial P_c}{\partial y}\right) - \rho_g D_{eff}\left(\frac{\partial m_v}{\partial y}\right)\right] & \text{, otherwise} \end{cases} \tag{56}$$

Eq.(57) can be further simplified, by assuming that the thermodynamic properties in this formula are not a function of the position. This will result in the final conservation of mass equation: eq(57). The thermodynamic properties in this equation will be discussed in the section 6.

$$(1-\epsilon)\rho_{fibres}\frac{\partial M}{\partial t} = \begin{cases} -\frac{k_w K}{\nu_w}\left(\frac{\partial^2 P_c}{\partial y^2}\right) - \rho_g D_{eff}\left(\frac{\partial^2 m_v}{\partial^2 y}\right) + \frac{\rho_v k_{nw} K}{\mu_g}\left(\frac{\partial^2 P_v \phi}{\partial y^2}\right) & \text{, if } P_v > P_{atm} \\ -\frac{k_w K}{\nu_w}\left(\frac{\partial^2 P_c}{\partial y^2}\right) - \rho_g D_{eff}\left(\frac{\partial^2 m_v}{\partial^2 y}\right) & \text{, otherwise} \end{cases} \tag{57}$$

5.5 Conservation of energy

In order to derive at the conservation of energy equation, Reardon [11] provides the schematics presented in figure 5.5. Reardon also did not include the movement of bound water in the model and assumed that bound water was evapourated first before being transported. The following conservation of energy equation was derived, which will be used in the present study as well:

$$\frac{\partial \rho c_p T}{\partial t} = -\frac{\partial Q}{\partial y} - \frac{\partial}{\partial y}\left[n_l H_l\right] - \frac{\partial}{\partial y}\left[n_l(H_l + H_s)\right] \tag{58}$$

Where:

- $\frac{\partial \rho c_p T}{\partial t}$ = Energy accumulation term. $\left[\frac{kJ}{m^3 s}\right]$
- $\frac{\partial Q}{\partial y}$ = Energy diffusion term. $\left[\frac{kJ}{m^3 s}\right]$
- $\frac{\partial}{\partial y}[n_l H_l]$ = Energy transport due to free water movement. $\left[\frac{kJ}{m^3 s}\right]$
- $\frac{\partial}{\partial y}\left[n_v(H_v + H_s)\right]$ = Energy transport due to vapour movement. $\left[\frac{kJ}{m^3 s}\right]$

The parameters n_L and n_v were already discussed in section 5.3. The energy that is accompanied by the mass flow terms consists of the enthalpy of free water (H_l), the enthalpy of water vapour (H_v) and the heat of sorption (H_s). The heat of sorption results from the evaporation of bound water. For a decreasing moisture content, the heat of sorption increases, because it becomes more difficult to evapourate the bound water as stronger molecular bonds need to be overcome. The only term that needs to be addressed is the energy diffusion term: $\frac{\partial Q}{\partial t}$.

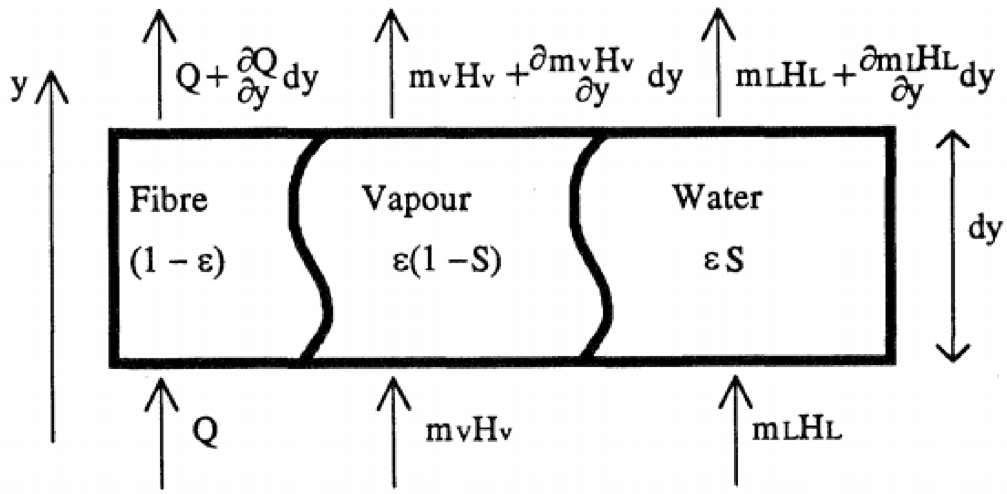

Figure 5.5: Energy analysis on a representative elementary volume. [11]

5.5.1 Heat conduction

The heat conduction in one direction can be described by Fourier's law:

$$Q = -\lambda \frac{\partial T}{\partial y} \tag{59}$$

The average thermal conductivity, λ, is a combination of the thermal conductivities of liquid water, water vapour, air and fibres. A detailed description of the average thermal conductivity will be given in section 6.5.

5.5.2 Final energy balance

The original energy balance is derived in eq.(58). By substitution of eq.(51), (52),(53) and (59) into eq.(58), the final energy balance is obtained:

$$\frac{\partial \rho c_p T}{\partial t} = \begin{cases} \lambda \frac{\partial^2 T}{\partial y^2} - \frac{k_w K}{\nu_w}(H_l)\left(\frac{\partial^2 P_c}{\partial y^2}\right) - \rho_g D_{eff}(H_v + H_s)\left(\frac{\partial^2 m_v}{\partial^2 y}\right) + \frac{\rho_v k_{nw} K}{\mu_g}(H_v + H_s)\left(\frac{\partial^2 P_v \phi}{\partial y^2}\right) & \text{, if } P_v > P_{atm} \\ \lambda \frac{\partial^2 T}{\partial y^2} - \frac{k_w K}{\nu_w}(H_l)\left(\frac{\partial^2 P_c}{\partial y^2}\right) - \rho_g D_{eff}(H_v + H_s)\left(\frac{\partial^2 m_v}{\partial^2 y}\right) & \text{, otherwise} \end{cases} \tag{60}$$

The thermodynamic properties in this equation will be discussed in section 6.

5.6 Boundary conditions

Both surfaces of the paper web experience several external conditions, while travelling through the dryer section. On a cylinder, only one side is open to drying, while in the pockets both sides are open to drying. It is imperative for the model to capture these alternating external conditions in order to obtain an accurate model. The external conditions consist of the heat input from the cylinder and heat- and mass transfer from the paper web.

By describing boundary conditions for single-sided drying, two sets of boundary conditions are required: one set describing the heated cylinder and the other side the pocket. Extension double-sided drying is easy, because the set describing the pocket has to be applied on both sides. Therefore, it suffices to describe boundary conditions for single-sided drying only, before extending to a complete dryer section.

5.6.1 Boundary conditions for single-sided drying

In single-sided drying, one surface faces an impermeable heated wall and the other surface is exposed to moving air. The latter surface allows mass and heat transfer over the boundaries, while the former only allows heat transfer. Various boundary conditions for single-sided drying have been derived in the literature. In order to find the most applicable set of boundary conditions, two different sources were explored.

5.6.1.1 Boundary conditions proposed by Reardon [11]

For the surface facing the hot impermeable cylinder wall, Reardon [11] proposed the following boundary conditions:

$$-\lambda \frac{\partial T}{\partial y}\bigg|_{y=0} = h_c\left(T_c - T_0\right) \tag{61a}$$

$$\frac{\partial \rho_v}{\partial y}\bigg|_{y=0} = 0 \tag{61b}$$

$$\frac{\partial P_l}{\partial y}\bigg|_{y=0} = 0 \tag{61c}$$

$$\frac{\partial P_{tot}}{\partial y}\bigg|_{y=0} = 0 \tag{61d}$$

For the surface exposed to moving air, Reardon [11] proposed the following boundary conditions:

$$-\lambda \frac{\partial T}{\partial y}\bigg|_{y=L} = h_s\left(T_L - T_{air}\right) \tag{62a}$$

$$-D_{eff} \frac{\partial \rho_v}{\partial y}\bigg|_{y=L} = h_m\left(\rho_{vL} - \rho_{vair}\right) \tag{62b}$$

$$\frac{\partial^2 P_l}{\partial^2 y}\bigg|_{y=L} = 0 \tag{62c}$$

$$\frac{\partial^2 P_{tot}}{\partial^2 y}\bigg|_{y=L} = 0 \tag{62d}$$

Eq.(61a) represents the temperature boundary conditions that relate the heat transfer from the cylinder to the heat conduction. Eqs.(61b), (61c) and (61d) ensure that zero mass flux over the cylinder wall is achieved. Eq.(62a) relates the heat conduction at the open surface to the heat transfer from the sheet. The mass transfer from the sheet is given in eq.(62b). According to Reardon [11], the open surface offers no resistance to pressure-driven flows of liquid and vapour. Therefore, Reardon [11] proposes eqs.(62c) and (62d) as boundary conditions for the pressure-driven flow terms. Eqs.(61d) and (62d) should only be used if the total pressure exceeds atmospheric.

5.6.1.2 Boundary conditions proposed by Nasrallah et al. [16]

The model proposed by Reardon [11] and its boundary conditions were specifically formulated to simulate the dryer section of a paper machine. Nasrallah et al. [16] do not specifically focus on paper drying, but focus on modeling convective drying of porous media in general. In their work, an adiabatic impermeable wall is modeled instead of a cylinder wall. For the surface facing the hot impermeable cylinder wall, Nasrallah et al. [16] proposed the following boundary conditions:

$$-\lambda \frac{\partial T}{\partial y}\bigg|_{y=0} + \Delta H_{evap}(\rho_l v_l)\big|_{y=0} = 0 \tag{63a}$$

$$(\rho_l v_l)\big|_{y=0} + (\rho_v v_v)\big|_{y=0} = 0 \tag{63b}$$

$$v_a = 0 \tag{63c}$$

For the surface exposed to the moving air, Nasrallah et al. [16] propose the following boundary conditions:

$$-\lambda \frac{\partial T}{\partial y}\bigg|_{y=L} + \Delta H_{evap}(\rho_l v_l)\big|_{y=0} = h_s\left(T_L - T_{air}\right) \tag{64a}$$

$$(\rho_l v_l)\big|_{y=L} + (\rho_v v_v)\big|_{y=0} = h_m\left(\rho_L - \rho_{air}\right) \tag{64b}$$

$$P_{tot} = P_{atm} \tag{64c}$$

Before elaborating and explaining the difference with Reardon's proposed boundary conditions, it is necessary to convert these boundary conditions to this specific situation. Nasrallah et al. [16] present a more elaborate model, where a separate continuity equation for dry air is incorporated. In the present study, this continuity equation is omitted. Therefore, eqs.(63c) and (64c) do not have to be used. The adiabatic permeable wall should be replaced by a heated impermeable one. This is achieved by substituting eq.(63a) with eq.(65).

$$-\lambda \frac{\partial T}{\partial y}\bigg|_{y=0} + \Delta H_{evap}(\rho_l v_l)\big|_{y=0} = h_c\left(T_c - T_0\right) \tag{65}$$

5.6.2 Low and high mass transfer theory

At the open side of the paper web, both Reardon [11] and Nasrallah [16] assume only a diffusive contribution (eq.(62b) and eq.(64b)). They approximate the evaporation from the web according to eq.(66). This corresponds to low mass transfer theory described in section 3.3.5.1.

$$\frac{\dot{m}_{ev}}{A} = h_m\left(\rho_{v,\,(L)} - \rho_{v,\,(bulk)}\right) \tag{66}$$

The temperature range in which Reardon [11] and Nasrallah et al. [16] performed their experiments to validate their models was below $100°C$. This means that the saturation pressure of water vapour was well below the atmospheric pressure (see figure 3.1). This results in a relative small difference in vapour densities between the paper web surface and the pockets, justifying the use of low mass transfer theory.
However, in the field survey performed, the outer cylinder wall temperature frequently exceeds $100°C$. Therefore, the saturated vapour pressure near the surface of the cylinder approaches (and possibly exceeds) the atmospheric pressure. Therefore, the convective component cannot be neglected and should be taken into account. By assuming a stagnant layer of air in the boundary layer just above the paper, the evaporation rate can be described in analogy to the theory described in section 3.3.5.2.

$$\frac{\dot{m}_{ev}}{A} = \frac{h_m P_{tot}}{R_v T} ln\left(\frac{P_{tot} - P_{v,e}}{P_{tot} - P_{v,s}}\right) \tag{67}$$

Karlsson [5] did not mention the different theories between low and high mass transfer. However, he proposes the use of eq.(67) to quantify the evaporation rate. In order to check if neglecting the convective component is justified, eqs.(66) and (67) will both be evaluated in the sensitivity analyses.

5.6.3 Concluding remarks on boundary conditions for single-sided drying

Several differences exist between sets of boundary conditions proposed by Reardon [11] and Nasrallah et al. [16]. Firstly, the set proposed by Reardon [11] assumes that there is no water vapour transfer and no liquid water transfer over the cylinder wall, while the set of boundary conditions proposed by Nasrallah et al. [16] assumes that the sum of water vapour and liquid water transfer over the cylinder wall is zero. This difference is also present in the boundary conditions for the open side: Reardon [11] proposes a boundary conditions for each individual transfer mechanism, while Nasrallah et al. [16] propose a boundary conditions for the sum of the different transfer mechanisms. This reasoning also explains the different number of boundary conditions proposed. The effect of the number of boundary conditions will be addressed in section 8.

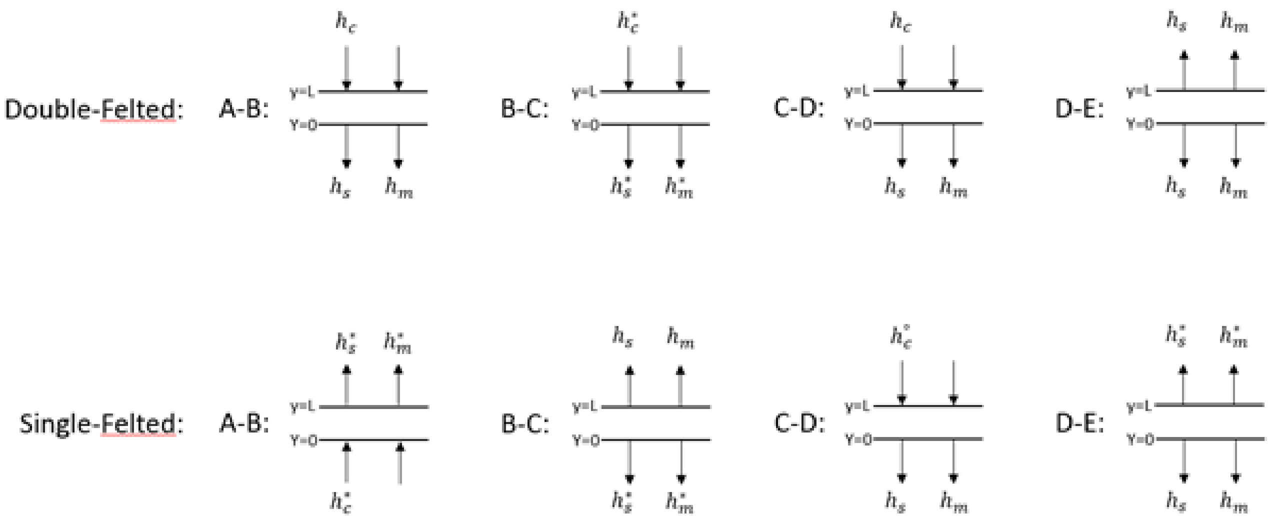

Figure 5.6: Different transfer coefficients depending on the location in the dryer section for a single- and double-felted configuration. The superscript '*' denotes that the transfer coefficient is influenced by the presence of a felt.

5.6.4 Extension to multicylinder drying

In order to simulate a complete dryer section, the external conditions need to be adjusted for the location of the paper web. Therefore, location-dependant boundary conditions are required.These location-dependent boundary conditions can be converted to time-varying boundary conditions for a given configuration and machine speed. In section 4.3 the cyclic variation in drying phases in multicylinder drying for a single- and double-felted configuration are elaborated. Figure 5.6 shows the coupled transfer coefficients applicable to each drying phase as presented in figures (4.4a) and (4.4b) for a double- and single-felted configuration.

5.7 Numerical discretization

In order to solve eqs.(57) and (60) with time varying boundary conditions, the use of a computational method is a necessity. The complexity of the equations makes it impossible to find an analytical solution. Therefore, a numerical method is chosen to solve the problem. For this model the finite difference method (FDM) is chosen. This means that the thickness of the paper web is subdivided into a finite number of layers. The one-dimensional grid is shown in figure 5.7. Each point in the grid represents a small layer of the paper sheet. Within such a layer, the same thermodynamic properties apply. Discretized time steps are used to solve the problem in the time domain. The derivatives in the spacial domain are approximated by central differencing. Although central differencing requires more points, it is more accurate compared to forward or backward differencing. Forward and backward differencing are first order accurate, whereas central differencing gives second order accuracy. An example of central differencing is shown in eq.(72), where the spatial derivative of function f at time j and point i is approximated.

$$\left(\frac{\partial f}{\partial y}\right)_i^j = \frac{f_{i+1}^j - f_{i-1}^j}{2\Delta} \tag{68}$$

In the same way the second derivative is approximated by:

$$\left(\frac{\partial^2 f}{\partial y^2}\right)_i^j = \frac{f_{i+1}^j - 2f_i^j + f_{i-1}^j}{\Delta^2} \tag{69}$$

In order to solve the model in the time domain, most paper drying models reported in the literature use a fully implicit scheme, ([11], [22], [24] and [52]). Using an implicit method instead of an explicit one, makes the model unconditionally stable. However, the computational effort increases, because an iterative numerical solver is required to obtain the solution at the next time level. For this model the Crank-Nicolson method is used to perform time integration. This method averages the forward- and backward Euler method performed at time j and $j+1$, respectively. The scheme is demonstrated in eq.(70) for the time derivative at point i. Note that F_i represents the right-hand side of eq.(57) evaluated at point i, The forward and backward Euler methods are both first order accurate in time, whereas the Crank-Nicolson method is second order accurate.

$$\frac{M_i^{j+1} - M_i^j}{\Delta t} = \frac{1}{2}\left[F_i^j + F_i^{j+1}\right] \tag{70}$$

By applying the central difference method in the spatial domain and the Crank-Nicolson method in the time domain, the model becomes second order accurate in both space and time.

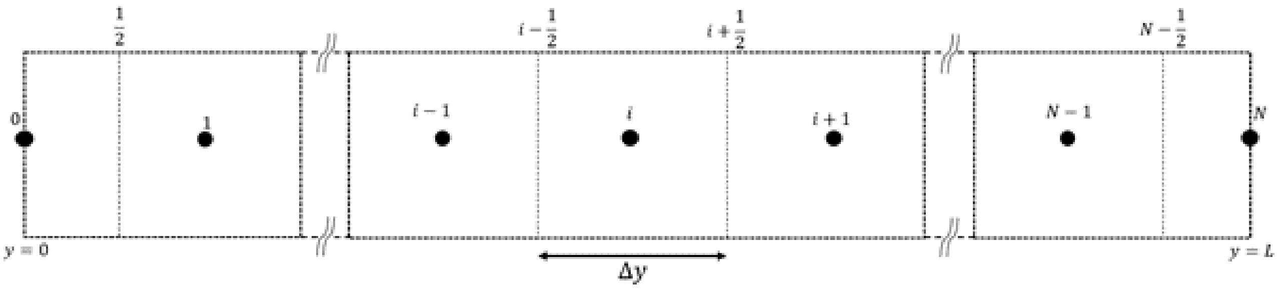

Figure 5.7: Numerical grid

5.7.1 Integral level of the conservation equations

Up to this point the conservation equations have been reported at differential level. These equations can also be evaluated at the integral level:

$$(1-\epsilon)\rho_{fibres}\frac{\partial M}{\partial t}\Delta y = \left[-\frac{k_w K}{\nu}\left(\frac{\partial P_c}{\partial y}\right) - \rho_g D_{eff}\left(\frac{\partial m_v}{\partial y}\right) + \frac{k_{nw}K}{\mu}\left(\frac{\partial P_v'\phi}{\partial y}\right)\right]_y \tag{71a}$$

$$- \left[-\frac{k_w K}{\nu}\left(\frac{\partial P_c}{\partial y}\right) - \rho_g D_{eff}\left(\frac{\partial m_v}{\partial y}\right) + \frac{k_{nw}K}{\mu}\left(\frac{\partial P_v'\phi}{\partial y}\right)\right]_{y+\Delta y} \tag{71b}$$

$$(1-\epsilon)\rho_{fibres}\frac{\partial M}{\partial t}\Delta y = \left[-\frac{k_w K}{\nu}\left(\frac{\partial P_c}{\partial y}\right) - \rho_g D_{eff}\left(\frac{\partial m_v}{\partial y}\right)\right]_y \tag{71c}$$

$$- \left[-\frac{k_w K}{\nu}\left(\frac{\partial P_c}{\partial y}\right) - \rho_g D_{eff}\left(\frac{\partial m_v}{\partial y}\right)\right]_{y+\Delta y} \tag{71d}$$

In this form, the transfer between control volumes can be tracked more carefully. In addition, mass and energy can easily be conserved. The control volumes can also be seen in figure 5.7. In the spatial domain, the first order derivatives can be approximated by:

$$\left(\frac{\partial f}{\partial y}\right)_{i+\frac{1}{2}}^j = \frac{f_{i+1}^j - f_i^j}{\Delta y} \tag{72}$$

The thermodynamic properties should also be evaluated at the boundaries. Therefore, the average value of the thermodynamic properties between two adjacent control volumes is assumed to represent the thermodynamic properties at the boundaries (eq.(73)). In this equation, G represents the different thermodynamic properties (enthalpy, diffusivity, thermal conductivity, etc.).

$$G_{i+\frac{1}{2}}^j = \frac{G_{i+1}^j + G_i^j}{2} \tag{73}$$

By defining the conservation equations at the integral level, second order derivatives are omitted. The Crank-Nicolson can also be used at the integral level to obtain second order accuracy in time. In this case F_i in equation (70) represents the right-hand side of eq.(71b) or (71d) evaluated at point i. The boundary conditions presented by Nasrallah et al. [16] are evaluated using the integral level equations. The results are presented in section 8.

6 Thermodynamic properties

In this section the thermodynamic properties used in the conservation equations will be discussed. The aim is to express the thermodynamic properties in terms of the moisture content (or volumetric saturation) and the temperature, so they can be used directly in the conservation equations.
The following thermodynamic properties will be discussed in this section:

- The sorptive behaviour of the paper web.
- The absolute permeability and the relative permeabilities.
- The diffusivity and the diffusibility.
- The average heat capacity
- The thermal conductivity.
- The fibre saturation point. This is necessary to explain the shrinkage occurring in the sheet.
- The different heat and mass transfer coefficients.

6.1 Sorptive behaviour

According to Reardon [11], sorption characteristics of a material, such as paper, describe the degree of adsorption of a particular sorbate, water for example, to the surface of that material. These characteristics become visible when the moisture content approaches the hygroscopic region. As mentioned earlier, there exists an equilibrium between the moisture content in the paper web and the humidity of the surrounding air. This means that bone-dry fibres tend to adsorb water in order to reach equilibrium.
This sorptive behaviour affects the transport of water through the paper in two ways. Firstly, the sorptive behaviour will reduce the vapour pressure above the water-air interface inside the pores. Consequently, the driving force for convective vapour flow will be reduced. This reduction factor is also referred to as the relative humidity of air [5] and its correlation to the moisture content for a specific temperature is shown by means of a sorption isotherm.
Secondly, the sorptive behaviour will require more energy for evaporation in order to break the strong hydrogen bonds between the pore walls and the water. This increase in energy is referred to as the latent heat of sorption [11]. In case of evaporation, the weaker bonds between fibre walls and water will be broken first, as this requires less energy. Therefore, for decreasing the moisture content, the heat of sorption will increase as only the stronger bonds remain.

6.1.1 Sorption isotherms

Sorption isotherms describe the relation between the vapour pressure reduction and the moisture content for a given temperature. These curves exists in different forms, based on the adsorption or desorption mechanics involved. The International Union of Pure and Applied Chemistry (IUPAC) has classified six types of isotherms. These are shown in figure 6.1. The different type of sorption isotherms can be derived from different adsorption (or desorption) models and are applicable in different situations.

6.1.2 Literature review on pulp and paper sorption isotherms

Due to the complexity and the inhomogeneity of the paper web, it is hard to fully describe the sorptive behaviour by simple mathematical relations. Therefore, experimental results are often used to construct sorption isotherms. For paper drying, only the desorption isotherms are used. The data obtained by Prahl [13] are widely used in the literature to construct empirical relations between the vapour pressure and the moisture content. Reardon [11], Lampinen and Toivonen [65] and Heikkilla [14] based their empirical correlations on Prahl's data. These correlations are shown in figure 6.2.

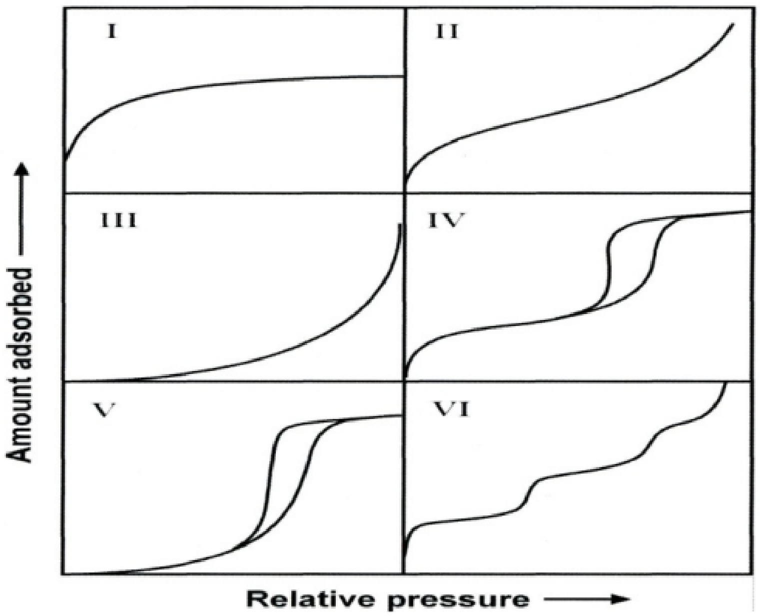

Figure 6.1: Different types of sorption isotherms, classified by IUPAC. [12]

Karlsson and Soininen [15] and Reardon [11] fitted the data using the following correlation:

$$\phi = \exp\{(\beta_1 T - \beta_2)\} \tag{74}$$

Where Reardon [11] determined β_1 and β_2 using a least square fitting:

$$\beta_1 = \exp\Big\{(-17.255M + 0.121\sqrt{M} - 3.640)\Big\} \tag{75a}$$

$$\beta_1 = \exp\Big\{(-14.313M + 2.167\sqrt{M} - 2.772)\Big\} \tag{75b}$$

Karlsson and Soininen [15] obtained the following values for β_1 and β_2:

$$\beta_1 = \exp\Big\{(-15.03M - 1.37\sqrt{M} - 3.41)\Big\} \tag{76a}$$

$$\beta_1 = \exp\Big\{(-13.53M - 2.90\sqrt{M} + 2.90)\Big\} \tag{76b}$$

Heikkila [14] proposed the following equation to fit the data from Prahl:

$$\phi = 1 - \exp\{-\left(47.58M^{1.877} + 0.10085TM^{1.0585}\right)\} \tag{77}$$

Reardon indentified that the desorption data from Prahl gave the best fit to a type II isotherm, indicating that a wide range of pore sizes is present [22]. In a type II isotherm, unrestricted monolayer-multilayer adsorption occurs. First a monolayer of water molecules is adsorbed by the fibre structure via strong hydrogen bonds. Monolayer formation occurs at very low moisture ratios (0 to 0.02 $\left[\frac{kg}{kg}\right](dry)$). Once the monolayer formation is almost complete, multilayer adsorption starts. This is the formation of additional layers of water molecules on top of the monolayer. Due to the increased Van der Waals forces existing between the vapour molecules in the pores, condensation happens at a lower pressure. This phenomenon is called capillary condensation. Once enough vapour has condensed, the pore becomes filled with liquid water creating a curved interface i.e. a meniscus. This meniscus allows an equilibrium to be reached below the saturated vapour pressure.

6.1.3 Heat of sorption

In order to break the strong van der Waals and hydrogen bonds, more energy is required to evapourate the molecules. In the desorption process, the weakest bonds are broken first. This results in an

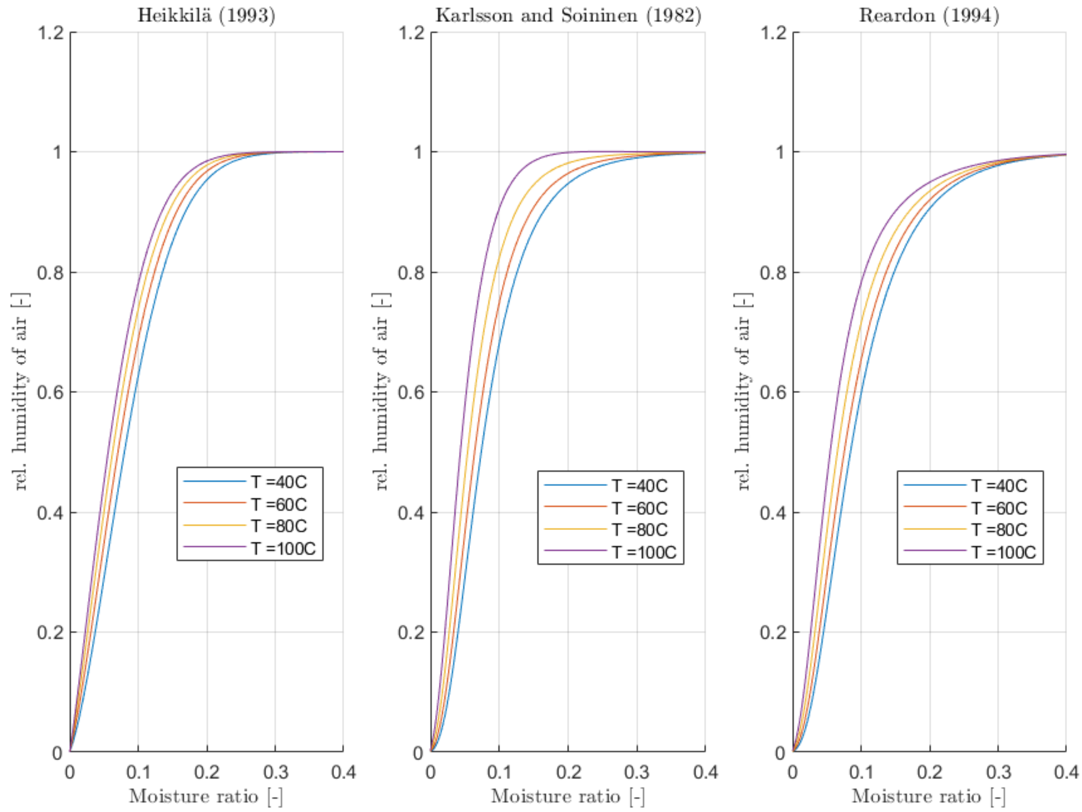

Figure 6.2: Sorption isotherms based on the data of Prahl [13] according to Heikkilä [14], Karlsson and Soininen [15] and Reardon [11].

increased heat of sorption for decreasing moisture content.
The Clausius-Clapeyron equation is widely used to calculate the heat of sorption. Assuming the water vapour as ideal gas, the Clausius-Clapeyron can be formulated as function of the relative humidity of air:

$$H_s = \frac{T^2 R}{M_v} \frac{\partial \ln \phi}{\partial T} \tag{78}$$

Applying eq.(78) to the data of Prahl [13] results in the heat of sorption curves presented in figure 6.3.

6.2 Permeability

The permeability of the sheet is an important property that affects the vapour and capillary flow through the sheet. Dullien [66] defines permeability as the conductivity of porous media with respect to permeation by a Newtonian fluid. By looking at eq.(57) it can be seen that the permeability is incorporated in the terms related to the pressure-driven Darcy flow. As mentioned earlier, the permeability can be subdivided into an absolute and relative term. The absolute term describes the permeability in case a single phase is present. The relative term takes into account the multiphase flow occurring in the paper sheet. This relative term is highly dependent on the moisture content.

6.2.1 Absolute permeability

Although several models exist to determine the permeability of a solid structure, permeability values are usually determined experimentally. Nevertheless, the well-known Kozeny-Carmen permeabilty theory will be discussed first, because this model may provide good predictions of the absolute permeability.

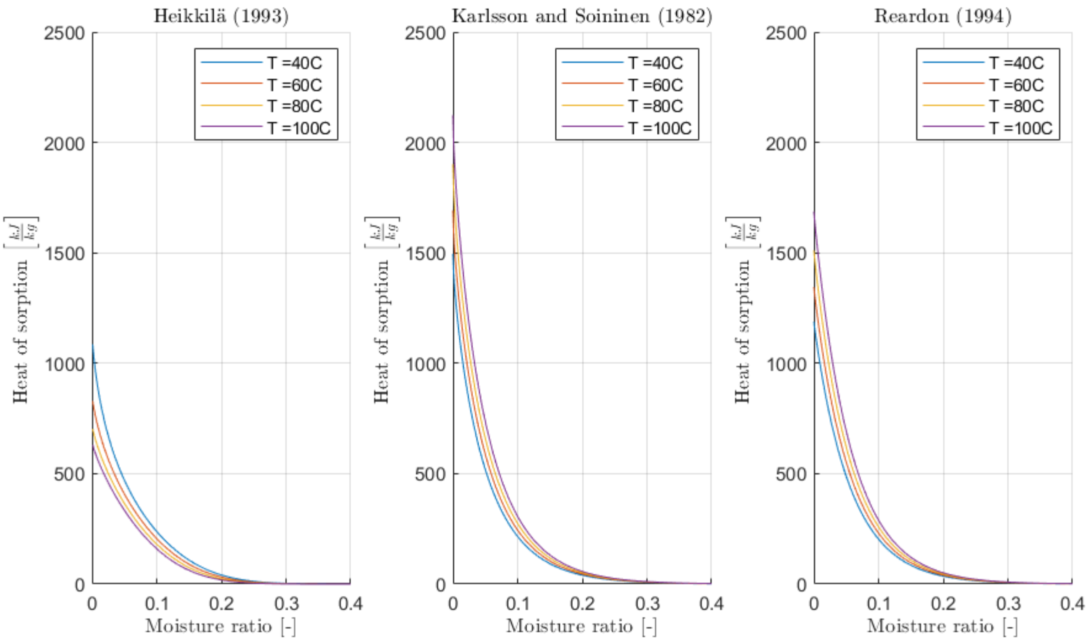

Figure 6.3: Heat of sorption curves based on the data of Prahl [13] according to Heikkilä [14], Karlsson and Soininen [15] and Reardon [11].

6.2.1.1 Kozeny-Carman permeability model

The Kozeny-Carman equation [67] [68] is defined as:

$$K = \frac{\epsilon^3 S_v^2}{k_c S_a^2 (1-\epsilon)^2} \tag{79}$$

Where:

- K = Absolute permeability. $[m^2]$
- ϵ = Porosity. $[-]$
- S_v = Specific volume. $\left[\frac{m^3}{kg}\right]$
- S_a = Specific area. $\left[\frac{m^2}{kg}\right]$
- k_c = Kozeny-Carman factor. $[-]$

In this equation the Kozeny-Carman factor, k_c, is added to account for the shape and the tortuosity. Ramaswamy [24] concluded that this factor was dependent on the porosity of the system and proposed the following correlation:

$$k_c = 5.0 + \exp\{14.0(\epsilon - 8)\} \tag{80}$$

Ramaswamy [24] also concluded that a fixed value for this factor could be assumed if ϵ = 0.5-0.8. The surface area is often determined experimentally. However, applicable values are often difficult to determine as this depends highly on the pulp examined and the method used.
Reardon [11] assumed cylindrical pores only and calculated its surface area based on the pore size distribution. Having determined the surface area, He found the Kozeny-Carman equation to be grossly overestimating the absolute permeability by a significant amount.
Kassenbeck [69] found that the surface area of once dried pulp may differ from never-dried pulp. The lumens in the fibres may not fully recover after rewetting and stay in collapsed position. This explains why the specific area of never-dried pulp may be larger compared to once-dried pulp [69].

6.2.1.2 Literature review on absolute permeability

A substantial amount of experimental values for the absolute permeability of pulp have been reported over the years. Asensio [1] summarized the different values reported in the literature.

Medium	Value $[m^2]$	Reference
Linerboard Lightweight coated paper Newsprint Fine paper Pulp sheet (softwood) Pulp sheet (hardwood) Handsheets (softwood)	$7-23 \times 10^{-15}$ 1.7×10^{-15} $2-10 \times 10^{-15}$ 13.5×10^{-15} 460×10^{-15} 48×10^{-15} $1-5 \times 10^{-15}$	Nilsson [70]
Newsprint	$5-12 \times 10^{-15}$	Reardon [11]
Handsheets (softwood) Handsheets (hardwood)	$0.1-1 \times 10^{-13}$ $0.5-6 \times 10^{-15}$	Lindsay and Brady [71]
Handsheets (softwood) Handsheets (tissue weight)	2.75×10^{-14} 9.35×10^{-14}	Polat et al. [72]
Newsprint Linerboard	4×10^{-14} 8×10^{-16}	Asensio et al. [73]

Table 6.1: An overview of absolute permeability values for different kinds of paper grades. This overview was provided by Asensio [1].

6.2.1.3 Concluding remarks on absolute permeability

Although the Kozeny-Carman theory was used by several in the literature, it has been found to overestimate the absolute permeability. Furthermore, the absolute permeability is dependent on numerous properties, which are hard to determine (surface area, porosity, etc.). Therefore, the Kozeny-Carman theory will not be used, but instead values reported in the literature are applied. Referring to table 6.1, Nilsson [70] performed the most recent and most elaborate experimental research. However, depending on the furnish type, a large difference exists between the values reported. The paper type investigated in the field survey was folding box board, with a pulp mixture of hard- and softwood fibres. This makes it extremely difficult to determine the right value for the absolute permeability. Therefore, it was chosen to investigate the effect of three different values for the absolute permeability: $33 \times 10^{-15}, 100 \times 10^{-15}, 300 \times 10^{-15}$ $[m^2]$.

6.2.2 Relative permeability

The pores in the paper web are filled with liquid and gas. This affects the effective permeability of one phase and, therefore, a relative permeability term is introduced. It can be described as a ratio of the effective permeability and the absolute permeability. It is a function of saturation and exists for the wetting fluid (liquid water) and for the non-wetting fluid (moist air). In order to determine the relationship between the saturation and the relative permeability, several models have been proposed over the years.
A well-known relation for the relative permebilities for the wetting and non-wetting phase was proposed by Brooks and Corey [10]:

$$k_w = (S^*)^{\frac{2+3\lambda}{\lambda}} \tag{81a}$$

$$k_{nw} = (1-S^*)^2 \left[1-(S^*)^{\frac{2+3\lambda}{\lambda}}\right] \tag{81b}$$

$$S^* = \frac{S-S_r}{1-S_r} \tag{81c}$$

In this case, λ represents the dimensionless pore size distribution index. Spolek and Plumb [64] found the best fit for the pore size distribution index, λ, to be -1.64.

Norouzi et al. [74] performed a more recent study on the wetting-phase relative permeability of porous media. By evaluating high resolution images of porous structures following a Gaussian pore size distribution, they correlated the relative permeability to the volumetric saturation. They modified the Corey-Brooks equation for the wetting phase (eq.(81a)) to:

$$k_{rw} = (S_w^*)^{n_w} \tag{82}$$

Where S_w^* is defined similar to eq.(81c). For a residual saturation, S_r, of 0.31, the best fit for n_w is found to be 1.98, with a root-mean-square-error of 0.01985. This corresponds to $\lambda = -1.96$ in eq.(81c).

The models presented above were derived on a theoretical basis with coefficients obtained through experiments. These relative permeability correlations were not specified for drying of paper sheets. Over the years, only little has been published about the relative permeabilities of different paper types. Sadeghi [22] and Ramaswamy [24] reported a correlation for the wetting relative permeability based on earlier work by Robertson [75] (eq.(83)). In this equation the saturation is calculated according to eq.(33). Unfortunately, no relative permeability correlation for the non-wetting phase was reported.

$$k_w = \begin{cases} 4.51 \times 10^{-12} \exp(25.86S), & 0.82 < S \leq 1 \\ 6.93 \times 10^{-6} \exp(8.54S), & 0.36 < S \leq 0.82 \\ 1.0 \times 10^{-11} \exp(46.05S), & 0.15 < S \leq 0.36 \\ 0, & 0 < S \leq 0.15 \end{cases} \tag{83}$$

Hashemi [76] calculated the relative permeability of air (being the non-wetting phase) for ten different furnish types at different moisture contents. To each furnish type a curve was fitted as a function of the moisture content. In addition, one general curve was fitted, because the relative permeabilities were closely correlated. The formula for the general curve was given as:

$$k_{nw} = 1 - 0.52(M_{free})^{1.35} \tag{84a}$$

$$M_{free} = M - M_{irr} \tag{84b}$$

By calculating the moisture content for which k_{nw} goes to zero (M_{max}), the normalized saturation can be calculated according to:

$$S_w^* = \frac{M - M_{bound}}{M_{max} - M_{bound}} \tag{85}$$

In this case, M_{max}, represent the maximal dry-basis moisture content that can be attained in the sheet.

In some models also the type of furnish is taken into account. According to Sadeghi [22], Asensio [1] reported relative permeabilities correlations for the wetting and non-wetting phase including the type of furnish:

$$k_w = a(M - M_{irr})^b \exp\{(M - M_{irr})^c\} \tag{86a}$$

$$k_w = a\frac{(M - M_{irr})^b}{2} \exp\left\{\left(\frac{(M - M_{irr})}{2}\right)^c\right\} \tag{86b}$$

$$k_{nw} = a + \frac{b}{1 + \left(\frac{(M - M_{irr})}{c}^d\right)} \tag{86c}$$

Here a, b, c, d are constants depending on the paper type. The coefficients can be found in the appendix (Table A.10.2 and A.10.3). As mentioned in section 5.4.2.3, Asensio [1] performed drainage experiments to obtain curves for the capillary pressure as function of moisture content. Subsequently, the relative permeabilities were calculated based on capillary pressure data, by using the same theory as Brooks and Corey [10]. The correlations for the relative permeabilities were proposed in the form of eqs.(86a), (86b), (86c).

Asensio [1] uses the irreducible moisture content, M_{irr}, to indicate the moisture content beyond which

capillary flow ceases. In the present study,, the FSP is used to denote this point. Therefore, it is important to replace the irreducible moisture contents, presented in tables A.10.2 and A.10.3, with the FSP.
Similar as above, the relative permeabilities can be written as functions of the normalized saturation. In this case, by finding the maximum moisture content, M_{max}, for which k_w goes to zero, the normalized saturation could be written according to eq.(85).

6.2.2.1 Concluding remarks on relative permeability

Numerous correlations have been proposed to describe the relative permeabilities for the wetting and non-wetting phases. An overview of the relative permeabities is presented in figures 6.4a and 6.4b. Only two of the ten correlations proposed by Asensio [1] are presented. These correlations represent the furnish type used in the field survey the best.
Brooks and Corey [10] and Asensio [1] presented similar correlations for the relative permeablities for the wetting phase. This is because they were derived from the same theory. The correlation proposed by Nozouri [74] is also derived from this same theory, but with different coefficients. The correlation proposed by Robertson [75] is directly derived from experimental data, but differs significantly. Therefore, it was chosen to include the correlations proposed by Brooks and Corey [10] and Robertson [75] in the sensitivity analysis.
For the relative permeability of the non-wetting phase, there is only little difference between the correlations for different furnish types according to Asensio [1]. However, there is a noticable difference between the correlations proposed by Brooks and Corey [10], Asensio [1] and Hashami [76]. Therefore, it was chosen to include the correlations proposed by Hashemi [76], Brooks and Corey [10] and Asensio (NSWK ($24°C$)) in the sensitivity analysis.

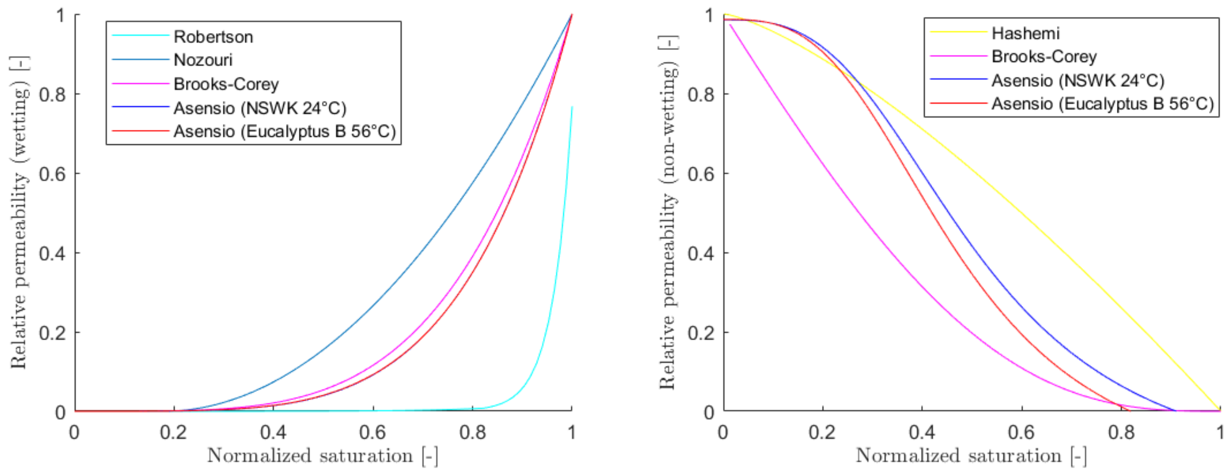

(a) Relative permeabilities of the wetting phase. **(b)** Relative permeabilities of the non-wetting phase.

Figure 6.4: Wetting and non-wetting relative permeability correlations as function of the volumetric saturation.

6.3 Diffusivity

Diffusive vapour flow is the only concentration-driven transport term in the mass balance. In order to quantify this term correctly, an effective diffusivity needs to be defined, that describes how the concentration gradient is related to the resulting mass flow. The effective diffusivity is different from the bulk diffusivity, because it takes into account the presence of the solid structure. A reduction factor between zero and unity is often used to relate the bulk diffusivity to the effective diffusivity. Before exploring this reduction factor, the bulk diffusivity for water vapour in air will be examined.

6.3.1 Bulk diffusivity of water vapour in air

Almost 100 years ago, Boynton and Brattain [77] investigated the effect of the temperature and pressure variations on the diffusivity of gasses. They related the diffusivity to a standardized diffusivity at 1 atm and $0°C$ using the following equation:

$$D_v = D_{v0}\left(\frac{T}{T_0}\right)^n \frac{P_0}{P} \tag{87}$$

This equation holds given the conditions that the operating pressure is far from its critical pressure. The use of this equation has proven to be an good approximation to the more exact formulation based on the theory of gases according to Massman [78].
Several values are reported in the literature for the standardized diffusivity, D_{v0}. For this work, the standardized diffusivity proposed by Massman [78] is used. He reported a standardized diffusivity of $D_{v0} = 0.2178\left[\frac{cm^2}{s}\right]$ at $T_0 = 0°C$ and $P_0 = 101.325\ [kPa]$.
Several values are reported for the exponential constant, n. Massman [78], Schirmer [79] and Wintergerst [80] reported a constant value of 1.81. This value was adopted in the present project.

6.3.2 Diffusibility

The diffusibility accounts for the presence of the solid structure. This factor takes into account the available flow in the cross sectional area and the vapour flow path, according to Incropera et al. [81]. Several relations have been proposed over the years. Kobari et al. [82] used a fixed value ($\frac{1}{1.4}$) together with a linear relation on saturion. Hartley and Richards [51] formulated a linear dependency on porosity, tortuosity and saturation. Ramaswamy [24] proposed two non-linear relations depending on the saturation. The correlations are summarized in table 6.2.
The diffusibility increases for decreasing saturation for two reasons. Firstly, the tortuousity of the vapour flow path decreases upon drying. Secondly, the cross sectional area available for vapour flow increases when the web is dried.
The correlations proposed by Kobari et al. [82] and Hartley and Richards [51] vary linearly with saturation and they are closely related. The correlations proposed by Ramaswamy [24] show a nonlinear behaviour. Therefore, it was chosen to include the correlations proposed by Hartely and Richards [51] and Ramaswamy [24] in the sensitivity analysis. Both correlations are shown in figure 6.5.

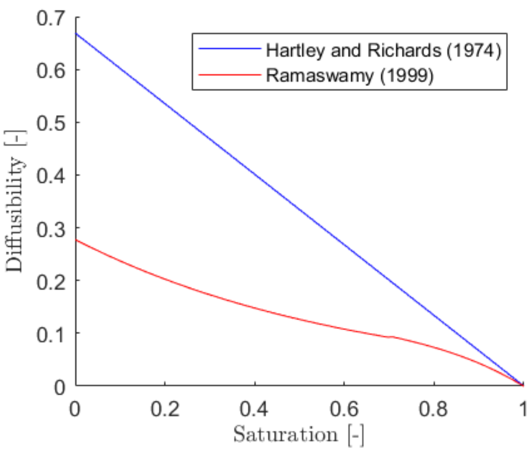

Figure 6.5: Two diffusibility correlations as function of volumetric saturation.

Reference	$\frac{D_{eff}}{D_v}$
Kobari et al. [82]	$= \frac{1}{1.4}(1-S)$
Hartley and Richards [51]	$= \Psi\epsilon(1-S)$
Ramaswamy [24]	
• $0 < S < 0.7$	$= 0.4\frac{\epsilon^{1.23}}{\exp\{1.574S\}}$
• $0.7 < S < 1$	$= \frac{\epsilon^{1.23}(1-S)^{1.08}}{4.33-3.33S}$

Table 6.2: Different diffusibilities proposed in the literature.

6.4 Heat capacity

In order to solve the energy balance (eq.(60)), it is imperative that an average specific heat capacity is defined. The average specific heat capacity can be calculated as a function of the specific heat capacities of the constituent components that exist in an REV point. The relative contribution of each individual component can be determined using the relations depicted in figure 4.2.

$$(\rho C_p)_{average} = (C_{p,\,(f)}\rho_f(1-\epsilon) + C_{p,\,(w)}\rho_w\epsilon S + C_{p,\,(v)}\rho_v\epsilon(1-S) + C_{p,\,(a)}\rho_a\epsilon(1-S)) \tag{88}$$

The average specific heat capacity per unit volume can at each point be approximated by eq.(88). Reardon [11] reported a value varying between 1.17-1.34 $[\frac{kJ}{kgK}]$ for the heat capacity of bone-dry fibres; an average value of 1.255 $[\frac{kJ}{kgK}]$ was chosen in this model. The specific heat capacities of water and water vapour were considered to be constant: 4.19 and 2.08 $[\frac{kJ}{kgK}]$, respectively. Although the heat capacity of the dry air is not taken into account by Reardon [11], it affects the average heat capacity and should be taken into account.
Besides specific heat values for fibres, Reardon [11] also reviewed several densities of bone-dry cellulose fibres. He reported values between 1500-1560 $[\frac{kg}{m^3}]$. Therefore, a value of 1530 $[\frac{kg}{m^3}]$ was chosen for this model.

6.5 Thermal conductivity

The conduction term in eq.(60) follows Fourier's law of conduction and an effective thermal conductivity is required. Determining the right thermal conductivity through experiments can be difficult, because of other thermal transport mechanisms involved.
Neverdeen et al. [83] measured the effective thermal conductivity for a number of paper sheets. Linear variation with paper density was found at lower moisture content. A large temperature dependence was reported for higher moisture contents, with values exceeding the thermal conductivity of pure water. The types of paper under investigation were groundwood handsheets and handsheets made from mixed waste paper. The accuracy of the presented data was considered to be insufficient to allow a good comparison with theory.
As obtaining good experimental results is difficult, deriving the effective thermal conductivity from theory can be a good alternative. The effective thermal conductivity will be a combination of the individual thermal conductivities. By using a combination of a serie- and parallel geometric lay-out, the effective thermal conductivity can be related to its individual components. In this case, the volume fraction of each individual component is used.
For a series and parallel geometry model the thermal conductivities can be described by eqs.(89a) and (89b), respectively. Nederveen et al. [83] and several others combined the two geometric structures according to eq.(89c), where x is a weight factor varying between 0 and 1. Parlosaari [84] reports a value of 0.46. Reardon [11] and Asensio [1] both reported a value of 0.5. This value was adopted in the present study. For future referencing, the subscript $_{eff}$ is dropped for convenience.

$$\lambda_{serie} = \frac{1}{\dfrac{1-\epsilon}{\lambda_f} + \dfrac{}{\lambda_w} + \dfrac{\epsilon(1-S)}{\lambda_v} + \dfrac{\epsilon(1-S)}{\lambda_a}} \tag{89a}$$

$$\lambda_{parallel} = \lambda_f(1-\epsilon) + \lambda_w + \lambda_v\epsilon(1-S) + \lambda_a\epsilon(1-S) \tag{89b}$$

$$\lambda_{eff} = \frac{1}{\dfrac{1-x}{\lambda_{parallel}} + \dfrac{x}{\lambda_{serie}}} \tag{89c}$$

6.5.1 Reported values for thermal conductivity of dry paper

Over the years, the thermal conductivity of dry paper has been studied for various furnish types. Reardon [11] and Sadeghi [22] have both separately summarized various values. The reported values can be found in table 6.3. Note that is hard determine the amount heat transferred by diffusion experimentally. Often additional transfer mechanisms are captured, resulting in overestimated values of the thermal conductivity. For this work a value of 0.105 $[\frac{W}{mK}]$ was chosen.

Author(s)	Sheet specification	Thermal conductivity $\left[\frac{W}{mK}\right]$
Lau and Prattes (1969)	Dry newsprint, 8% moisture	0.041
Depoy (1972)	Dry paper: • M<0.04 • 8% moisture	 0.121 0.161
Kirk and Tatlicibasi (1972)	Bleached sulfite handsheets	0.084 to 0.0117
Powell and Strong (1974)	Dry newsprint	0.069
Hartley and Richards (1974)	Cellulose	0.335
Kerekes (1980)	Dry Newsprint, 8% moisture: • uncalendered • calendered	 0.127 0.169
Nakagawa and Shafizadeh (1984)	Dry sulphite pulp	0.067
Soininen et al. (1985)	Dry paper	0.105
McAdams (1985)	Unspecified paper type	0.130

Table 6.3: Reported values for thermal conductivity of dry paper reported by Reardon [11] and Sadeghi [22].

6.6 Fibre saturation point (FSP)

As described in section 4.2.3.1, the FSP denotes the onset of the hygroscopic region. It does not represent a discontinuity in pore sizes, but denotes a moisture content below which the sorptive effects become significant. Furthermore, this point denotes the start of the shrinkage process as will be described in the next section.
According to Reardon [11] and Sadeghi [22] the value of the FSP decreases for increasing temperature.

This can also be deduced from the sorption isotherms presented in figure 6.2. For a given temperature at a certain moisture content, the value of the relative humidity approaches 1 asymptotically. This point indicates the onset where the hygroscopic effect become visible, i.e. the FSP. At higher temperatures, the asymptotic value is reached at lower moisture content, indicating that sorptive effects become significant at lower moisture content. Reardon [11] reported FSPs varying from 0.2 to 0.4 $\left[\frac{kg}{kg}\right]$ (dry), based on the sorption isotherms presented in figure 6.2.

Another parameter affecting the FSP is the pulp type and treatment. Luukko [85] reports FSP values ranging from 0.3 to 1.5 $\left[\frac{kg}{kg}\right]$ (dry), depending on the fibrillar content, lignin content and pulping process. Furthermore, the FSP of virgin fibres differ significantly from recycled fibres.
There are no data available for the pulp dried in the field survey. Therefore, it was chosen to include FSPs of 0.2, 0.3 and 0.4 $\left[\frac{kg}{kg}\right]$ (dry) in the sensitivity analysis performed in section 9.

6.7 Shrinkage

As the paper web is transferred through the dryer section the web shrinks in thickness-, machine- and cross- direction. However, the paper web is strained in the machine direction, which causes that the web will mainly shrink in the thickness- and cross-direction.
Heikkila [14], Reardon [11], Harrmann et al. [56], Sadeghi [22] and others report that shrinkage is mainly controlled by water located in the fibres walls. Shrinkage occurs when the moisture content reaches the FSP. The onset of the hygroscopic region is, therefore, an excellent point for initiating shrinkage.
During the evaporation of bound water, the fibres collapse because of internal or frozen-in stresses. The collapsing fibres affect the porosity and thickness of the web. A complete understanding on the shrinkage process requires an extensive knowledge on the structure and consistency of the fibres itself. This knowledge is beyond the scope of the present study. Here it is sufficient to know that water is

forced into the fibres in the pulping process. This causes the fibres to swell.
During the forming process the fibres are mainly aligned with the paper web. This causes that during desorption the relative shrinkage in the thickness direction will be the largest. Sadeghi [22] reports a distribution between shrinkage in machine-, cross- and thickness-direction of 1:2:50, respectively. Wahlström [86] reports a shrinkage in-plane of 2 to 6%, while the thickness direction can shrink 40 to 60%. Therefore, it is imperative that the thickness-direction shrinkage is taken into account when modeling the paper drying process.
To determine the thickness of the sheet as function of moisture content, Asensio and Seyed-Yagoobi [73] proposed eq.(90a). This equation was derived on the premise that the total thickness consists of a fibre, air and water layer. Eqs.(90b) and (90c) were proposed to capture the effect of shrinkage on porosity. They did not take into account the onset of the hygroscopic region and assumed shrinkage to happen in the early stage of drying as well. In this case L_{ref} and ϵ_{ref} denote the reference thickness and porosity, respectively, measured at a dry-basis reference moisture content M_{ref}.

$$L = L_{ref} + \frac{b_{wt} M}{\rho_l} \tag{90a}$$

$$\epsilon = 1 - \frac{1-\epsilon_{ref}}{1 + \frac{b_{wt} M}{\rho_l L_{ref}}} \tag{90b}$$

$$\epsilon_{ref} = 1 - \frac{1}{\rho_f - \rho_{air}} \left(\frac{b_{wt}(1-M_{ref})}{L_{ref}} - \rho_{air} \right) \tag{90c}$$

Reardon [11] did take the FSP into account and proposed eq.(91) to relate the thickness to the moisture content. He did not incorporate a varying porosity in his model. In this case, L_{bd} denotes the thickness of bone-dry paper.

$$L = L_{bd} + min(M, M_{FSP}) \frac{b_{wt}}{\rho_l(1-\epsilon)} \tag{91}$$

Sadeghi [22] also incorporated the idea that shrinkage only occurs in the hygroscopic region. He omitted the use of an equilibrium moisture content, but used properties of bone-dry paper instead. He modified the eqs.(90) to eqs.(92).

$$L = \begin{cases} L_{bd}\left[1 + \dfrac{M\rho_{bd}}{\rho_l(1-\epsilon_{bd})}\right] & M < M_{FSP} \\ L_{bd}\left[1 + \dfrac{M_{FSP}\rho_{bd}}{\rho_l(1-\epsilon_{bd})}\right] & M \geq \mathrm{M}_{FSP} \end{cases} \tag{92a}$$

$$\epsilon = \begin{cases} 1 - \dfrac{1-\epsilon_{bd}}{1 + \dfrac{M\rho_{bd}}{\rho_l(1-\epsilon_{bd})}} & M < M_{FSP} \\ 1 - \dfrac{1-\epsilon_{bd}}{1 + \dfrac{M_{FSP}\rho_{bd}}{\rho_l(1-\epsilon_{bd})}} & M \geq \mathrm{M}_{FSP} \end{cases} \tag{92b}$$

In this case, ρ_{bd} and ϵ_{bd} denote the bone-dry density and porosity, respectively. Assuming that bone-dry paper only consists of cellulose fibres, the relation between the density of bone-dry paper and cellulose fibres can be written as:

$$\rho_{bd} = \rho_f\,(1-\epsilon_{bd}) \tag{93}$$

The importance of the onset of the hygroscopic region it emphasised in numerous papers. In addition, the thickness variation substantially contributes to the porosity property of the sheet. Therefore, only the relation proposed by Sadeghi (eq.(92)) will be used in this model.

6.8 Heat and mass transfer coefficients

In order to complete the model, relations for the various heat and mass transfer coefficients should be defined. These coefficients depend on the configuration that applies to a specific location in the dryer

section.
As explained in section 3.3.2, a flow-over-a-flat-plate configuration is used to obtain a relationship for the heat transfer coefficient between the paper web and air pocket. By using the Chilton-Colburn relation a similar relationship was obtained for the mass transfer coefficient. In order to complete the model, the presence of the felt needs to be taken into account. Only double-felting occurs in the dryer section investigated. Therefore, three more transfer coefficients need to be addressed:

- web-cylinder heat transfer coefficient
- web-felt-air heat transfer coefficient
- web-felt-air mass transfer coefficient

6.8.1 For the paper web cylinder heat transfer coefficient

The contact heat transfer coefficient (h_c) describes the resistance to heat transfer as a result of the interface between the paper web and the cylinder wall. This transfer coefficient accounts for both the direct contact of the fibres with the cylinder wall and the heating of the gas-filled or water-filled pores that exist between the fibres and the cylinder wall. This coefficient is heavily dependent on the following parameters according to [14]:

- Moisture content
- Felt tension
- Air film accumulation between the web and dryer surface
- Cylinder and paper web surface smoothness

The first two parameters will be discussed in more detail below, because several correlations have been reported in the literature.

6.8.1.1 Moisture content

When the moisture content is high, pores in direct contact with the heated cylinder surface are filled with water. Due to the higher thermal conductivity of water, this contributes to a higher heat transfer coefficient. Upon drying, the number of water filled pores is reduced. As the paper dries, the moisture content near the cylinder wall is reduced and less direct contact between liquid water and cylinder wall exists. Therefore, the contact heat transfer coefficient reduces for lower moisture content. There are several correlation proposed in the literature describing this phenomenon.
Lemaitrre [87] constructed a paper drying model for a double-felted configuration. He did not take into account the internal transport mechanisms, but experimentally found a heat transfer coefficient for each dryer cylinder. Together with the moisture content at each dryer, the moisture content was related to the heat transfer coefficient.
Yeo et al. [23] constructed a comparable model, where lightweight newsprint was under investigation. They used a double-felted configuration, but did not report the effect of felt tension and the range of moisture content for which this correlation is accurate.

$$\frac{h_c}{4184} = 0.1661e^{1.512M} - 0.4775e^{-15.67M} \tag{94}$$

Rhodius and Göttsching [88] experimentally determined the relationship between moisture content and heat transfer coefficient between paper web and cylinder for a double-felted configuration to be:

$$h_c = 1556.6M + 52.87 \tag{95}$$

No information about the felt tension and valid range of moisture contents was given.
Wilhelmsson and Stentstrom [89] wrote an extensive paper about the different transfer coefficients that play a role in multicylinder paper drying. For the heat transfer coefficient between paper web and cylinder, the following relationship was proposed:

$$h_c = h_{c0} + 955M \tag{96}$$

h_{c0} was reported to vary between 100-500 $[\frac{W}{m^2K}]$ depending on the furnish type under investigation. The specifications of the felt were not reported.
Reardon [11] also assumed a linear correlation with the moisture content. By solving a heat balance, he was able to estimate the losses per dryer section and determine the sheet temperatures. Combining this with the energy input by the steam, he was able to correlate the contact heat transfer coefficient for two different drying sections according to eqs.(97a) and (97b).

$$h_c = 261M + 577 \tag{97a}$$

$$h_c = 186M + 597 \tag{97b}$$

All correlations proposed above are included in figure 6.6. Although there is a substantial difference between the correlations proposed, a global trend can be seen. For increasing moisture content, the contact heat transfer coefficient between the paper web and the cylinder increases as well. Three proposed correlations will be investigated in the sensitivity analysis. Yeo et al. [23] proposed the only non-linear correlation, as is reported the most recently. Rhodius and Göttsching [88] proposed the linear correlation with the highest moisture content dependency. Reardon [11] proposed the linear correlation with the lowest moisture content dependency (PM2). Therefore, the fitness of these three correlations will be added to the sensitivity analysis in section 9.

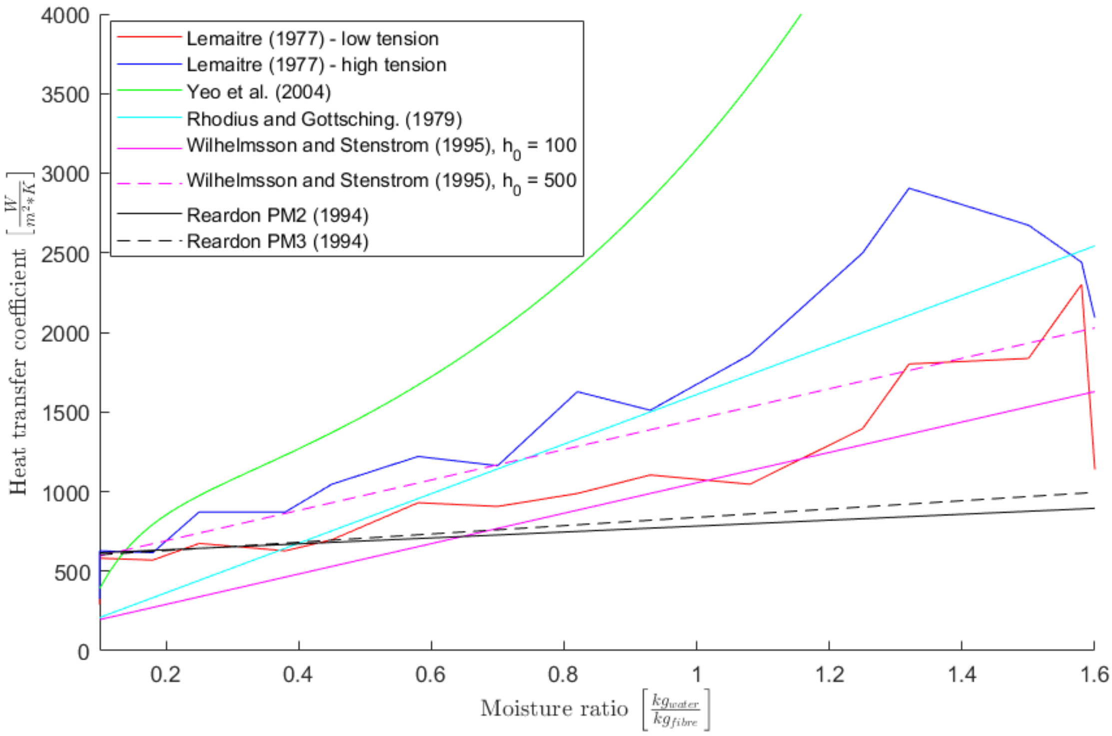

Figure 6.6: paper web-cylinder heat transfer coefficient correlations for varying moisture ratios.

6.8.1.2 Felt tension

As described earlier, the characteristics of the felt have a considerable effect on the drying rate. Two main characteristics can be distinguished: the felt tension and its permeability. For the heat transfer coefficient between the paper web and the cylinder only the felt tension is of influence. Before exploring correlations proposed in the literature, it is important to address the normal operating conditions for felt tension.
In 2002, the Technical Association of the Pulp and Paper Industry (TAPPI) released an technical information paper to provide guidelines for selecting the right felt tension [90]. In this paper the minimum recommended tension for any dryer section was reported to be 0.7$[\frac{kN}{m}]$. However, according to TAPPI [90], modern paper machines are typically designed for operating felt tensions in the range

of 1.8-3.5 $\left[\frac{kN}{m}\right]$.
In the literature, several authors have investigated the effect of felt tension on the contact heat transfer coefficient. Amar et al. [91] found that increasing the felt tension up to 300-400 $\left[\frac{N}{m}\right]$ leads to a higher contact heat transfer coefficient. Increasing the tension above 400 $\left[\frac{N}{m}\right]$ has no effect on the contact heat transfer coefficient. Reardon [11] reported similar results. He performed static laboratory tests in order to find correlations for the contact heat transfer coefficient. Only slightly increased contact heat transfer coefficients were reported for a felt tension beyond 1780 $\left[\frac{N}{m}\right]$.

The felt tension is considered to have no effect on the contact heat transfer coefficient, because modern paper machines are typically designed for felt tensions above 1.8 $\left[\frac{kN}{m}\right]$.

6.8.1.3 Unfelted dryers

In the literature a contact heat transfer coefficient for unfelted dryers has not been specified. This value will typically be lower compared to felted dryers. In this case, the contact heat transfer coefficient depends on the tension of the pape rweb itself. This is typically 200-300 $\left[\frac{N}{m}\right]$ according to Wilhemsson [89]. In this range the effect of the web tension is significant as an air film can form between the web and the cylinder, deteriorating the contact heat transfer coefficient. For this model a constant value of 250 $\left[\frac{W}{m^2K}\right]$ for the web-cylinder heat transfer coefficient is chosen if no felt is pressing the paper web against the cylinder.

6.8.2 web-felt-air heat transfer coefficient

According to Wilhelmsson and Stenstrom [89], the felt reduces the web-air heat transfer coefficient by only a small extent. Therefore, the web-felt-air heat transfer coefficient is assumed to be equal to the web-air heat transfer coefficient. Ghodbanan et al. [92] used this same assumption in his model and managed to get accurate results. This assumption will be copied in this model.

6.8.3 web-felt-air mass transfer coefficient

Reardon [11] did extensive research on the web-felt-air mass transfer coefficient. He investigated the effect of the cylinder temperature, air velocity, felt tension, felt permeability, pulp furnish and basis weight on the mass transfer coefficient. On a static curved heated plate he applied a sheet, which was supported by a felt. By forcing air flow over the felt, the cylinders were imitated. In case of no felt he found that the value for the mass transfer coefficient for various velocities was located between the flow-over-a-flat-plate and flow-over-a-cylinder configuration. Furthermore, he found that the mass transfer coefficient was relatively independent of the basis weight, pulp furnish, felt tension and cylinder temperature. However, he noticed that the permeability of the felt was of significant influence on the mass transfer coefficient. His findings are shown in figure 6.7. Note that in this figure the nylon felt represents the situation where no felt is applied. The nylon threads ensured pressure was applied on the paper web throughout the experiment. The mass transfer coefficients reported by Reardon can not be adopted directly. He performed experiments, where the applicable characteristic length was only 0.225 $[m]$, which is one order of magnitude smaller compared to the industrial case.

A linear reduction factor was derived from Reardon's data and applied to this model. Depending on the permeability of the felt, the reduction factor varies between 2.4-3.9 compared to the no-felt arrangement. For the industrial drying case, the mass transfer coefficient was estimated to be 0.0170 $\left[\frac{m}{s}\right]$ (assuming a transient Reynolds number of 500000, a velocity of 403 $\left[\frac{m}{s}\right]$, a characteristic length of 5 $[m]$, atmospheric pressure and a temperature of $80°C$). Using the reduction factors in combination with eq.(98), the reduced mass transfer coefficient for a double-felted arrangement varies between 0.0044-0.0071 $\left[\frac{m}{s}\right]$.
Similar values were reported by Stenström [33], who did a recent the literature study on paper drying. He reported mass transfer coefficients varying between 0.004-0.011 $\left[\frac{m}{s}\right]$ for modern felts.

$$h_m^* = \frac{h_m}{f_{reduc}} \tag{98}$$

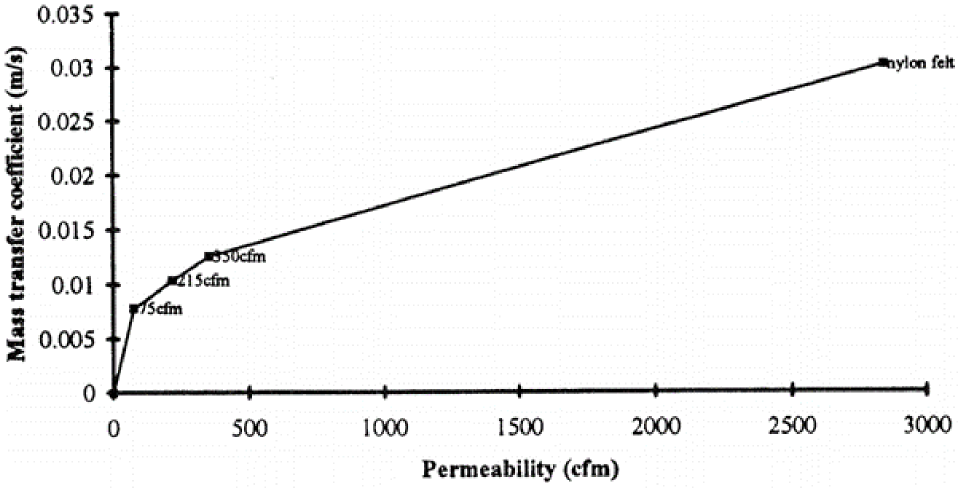

Figure 6.7: The effect of felt permeability on the mass transfer coefficient. 75, 215 and 350 cfm correspond to permeabilities of 1371, 3931 and 6400 $\left[\frac{m^3}{m^2h}\right]$ at 127 $[Pa]$, respectively. The nylon felt corresponds to the configuration where no felt is present.

Hhere:

- h_m^* = corrected mass transfer coefficient to account for the felt $\left[\frac{m}{s}\right]$
- h_m = uncorrected mass transfer coefficient $\left[\frac{m}{s}\right]$
- f_{reduc} = reduction factor $[-]$

In the present study, the reduced mass transfer coefficients was assumed to be 0.0085 $\left[\frac{m}{s}\right]$. This corresponds to a reduction factor of 2.

7 Field survey

In order to validate the model and find the optimal set of transport properties, its validation against actual industrial data is essential. Therefore, a field survey was conducted at a Dutch board producer. The paper machine under investigation was the PM2. First, the lay-out of the dryer section of the machine will be elaborated. This includes the configuration of the cylinders and felts and the the lay-out of the ventilation. A detailed lay-out of the steam and condensate system will not be shown, because these are quite complex. For this project, understanding which cylinders are grouped together and connected to which steam supply suffices. This will be explained together with the technical specifications.
Next, the technical specifications of the paper grade are summarized. Subsequently, heat and mass balances will be formulated so that a static analysis of the different dryer sections can be computed. Lastly, an overview of the measured conditions per pocket will be discussed. At this point, it is important to note that this field survey was extensive and thorough. Therefore, only relevant measurements to help verifying the model will be discussed.

7.1 Lay-out dryer section

7.1.1 Configuration of the cylinders

A detailed lay-out of the dryer section of the PM2 is depicted below. It is split into three figures (7.1, 7.2 and 7.3), each representing different smaller sections of the complete dryer section. The different elements of the cylinder and felt configuration are listed in table 7.1.

Figure 7.1 presents the pre-dry section. In this section, the paper web enters from the press section and is dried over 34 cylinders to a specific moisture content so the drying effect over the MG is optimal. Note that in this figure, the first five bottom cylinders are represented with felts. However, in reality these felts were removed due to runnability problems for specific paper grades.

Figure 7.2 presents the MG, the first after-dry section and the speedsizer. In this case, the MG is used to provide smooth surface properties. The first after-dry section ensures the paper web is sufficiently dry before entering the size press. In the size press, the sizing solution is added to the paper. In this case, the paper web is squeezed between two pressing cylinders. By feeding the sizing solution in the closing nip, it is pressed into the paper web. The sizing solution provides good printability, sufficient surface strength and water resistance to the paper web.

Figure 7.3 includes the following sections: second after-dry section, calander, two coaters, two infrared dryer groups, two correction groups and a cooling section. Due to the application of the sizing solution, the moisture content in the paper is increased. Therefore, more after-dry sections are used to ensure sufficient drying, before being calendered.
In the calendering process, the paper web is pressed between two rotating rolls ensuring smooth surfaces and a constant thickness, enhancing the printability of the paper web. In the coaters, final solutions are added to meet the final requirements. After applying the coating, the paper web is dried using non-contact infrared dryers. By avoiding contact with the paper web, a good adhesion of the coating, to the paper web is ensured.
By adding coating to the paper the moisture content is increased. Therefore, correction groups are installed to dry the paper to the right moisture content. Finally, the paper web is transported over cooling groups to cool the paper web.

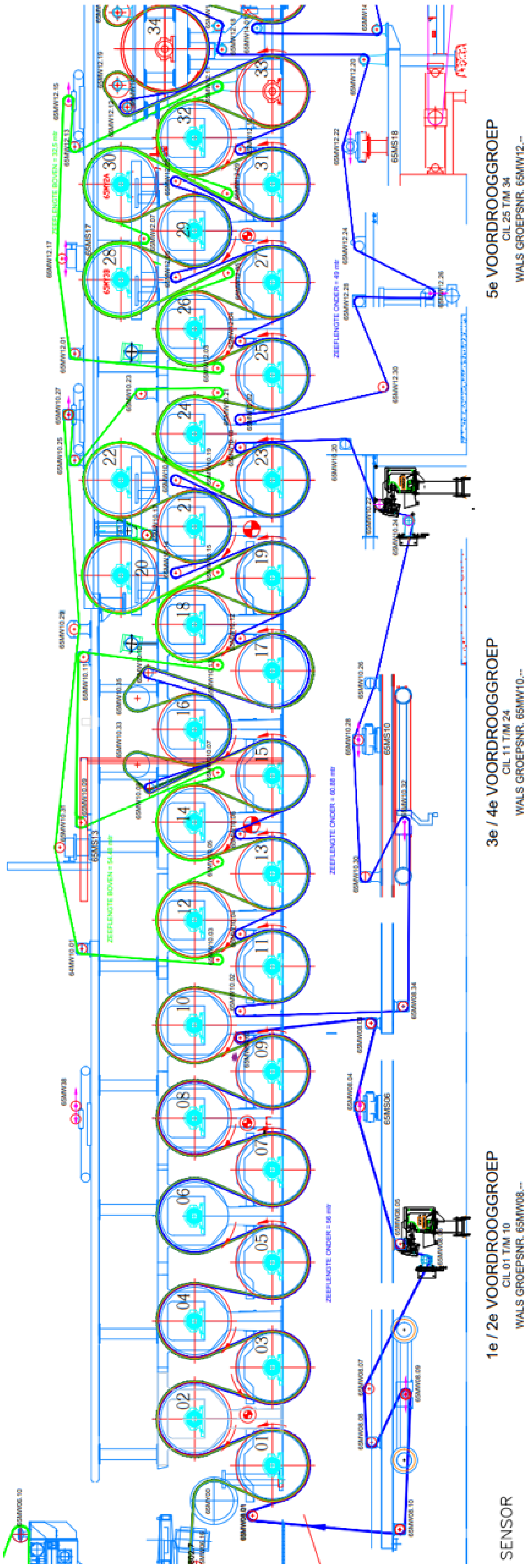

Figure 7.1: Lay out of the Predryer section. The wet paper enters the dryer section on the left. After cylinder 34, the paper web is transferred to the pre-MG.

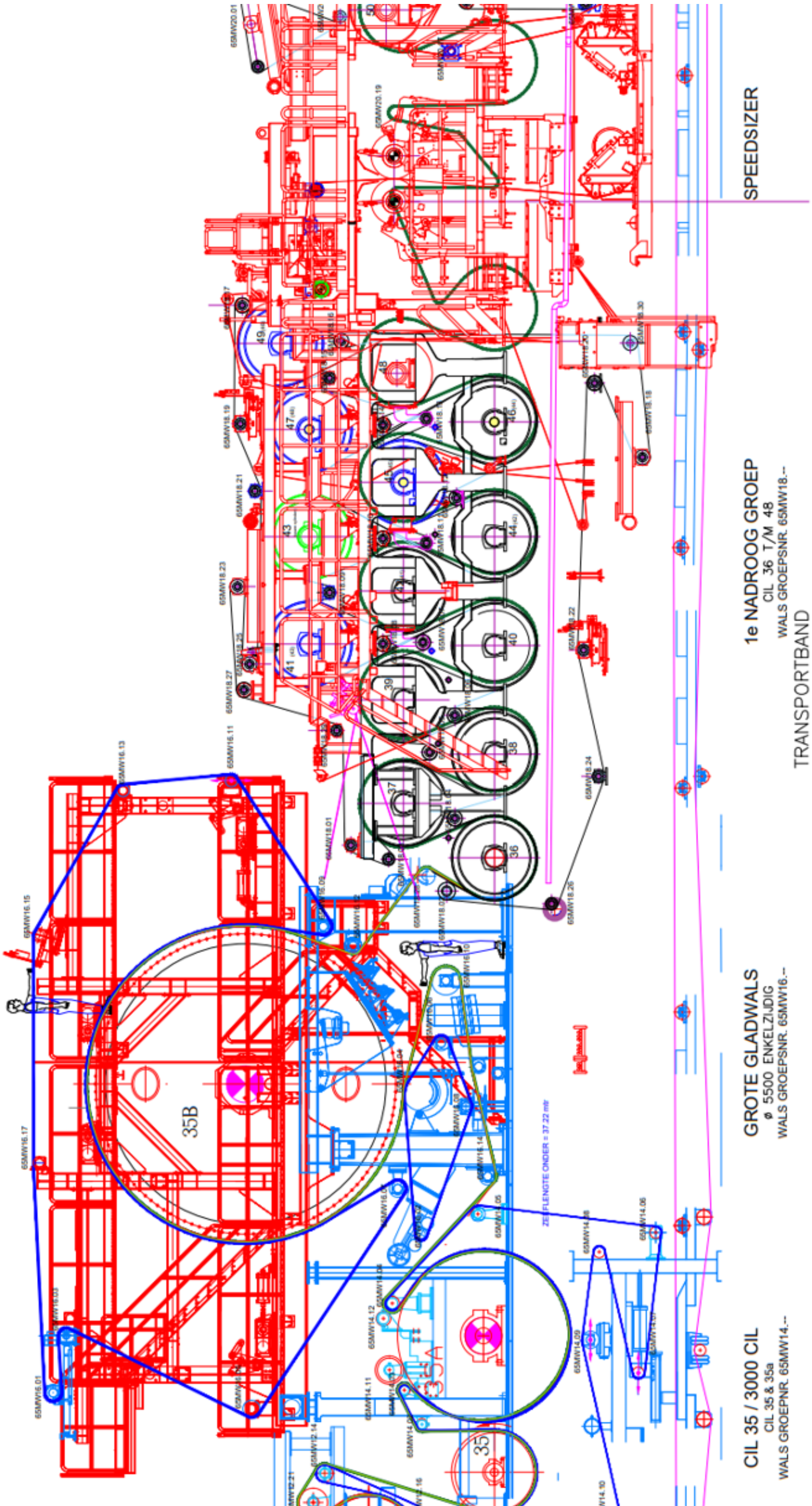

Figure 7.2: Lay out of the Pre-MG (cylinder 35A), MG (cylinder 35B) and the first after dryer section. Notice that on the right the speedsizer, located between the two after dryer sections, is shown.

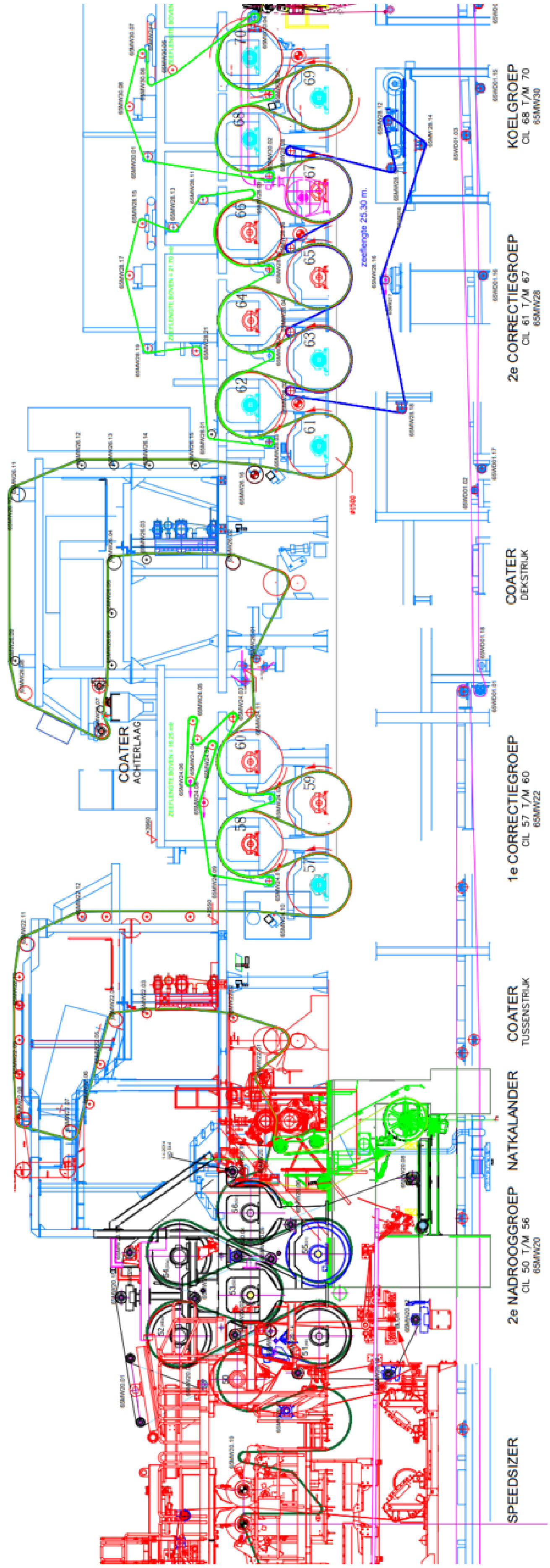

Figure 7.3: Lay out of second after dryer section, the correction groups and cooling cylinders. Notice that before the correction groups the coaters are located.

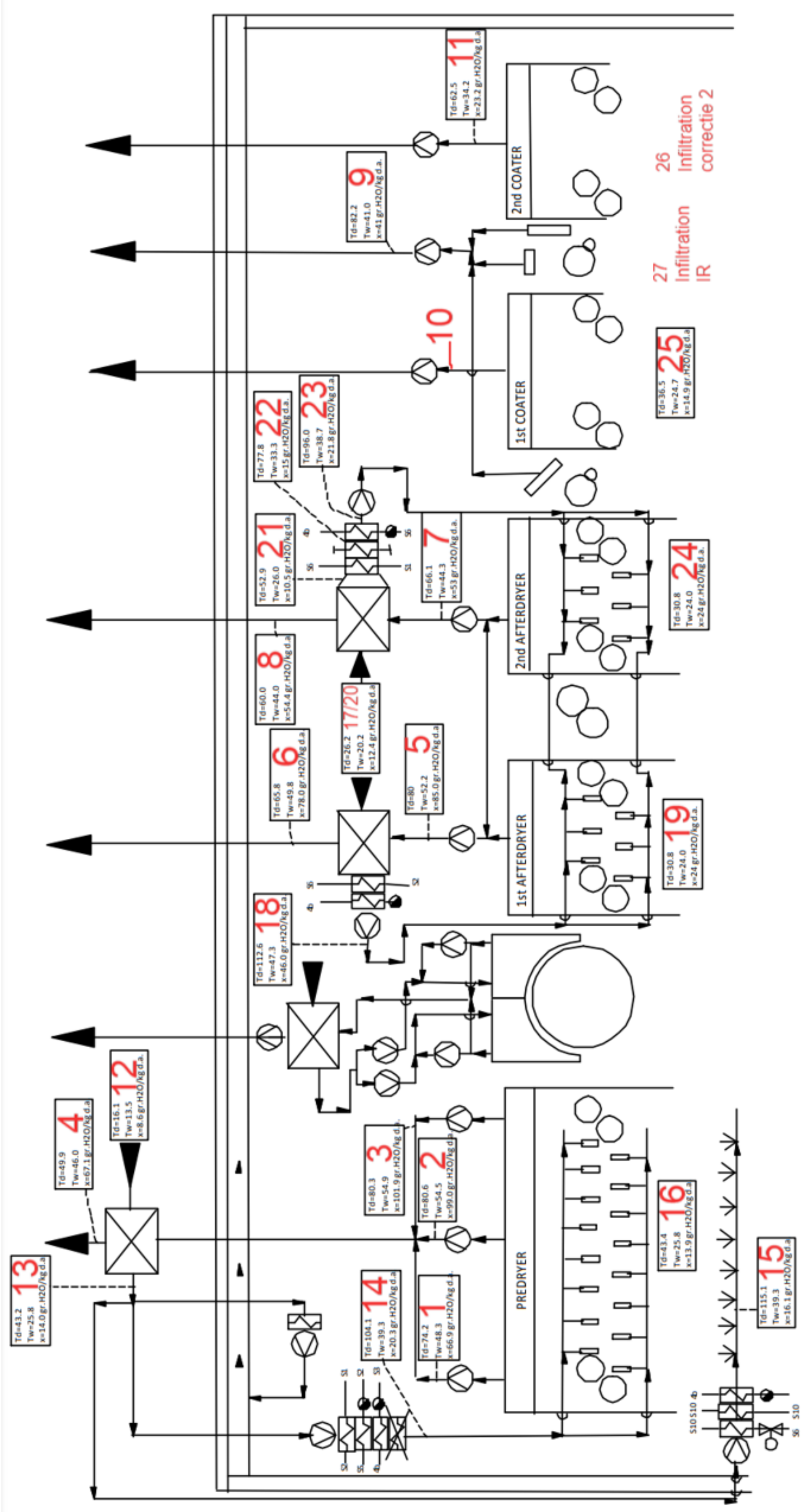

Figure 7.4: Lay-out of the ventilation. The numbers refer to relevant air streams used to compute heat- and mass balances. In each relevant air stream, the wet- and dry bulb temperature is measured to compute the humidity's.

Dryer section	Cylinders	Felt arrangement	Remarks
pre-dry section	0-10	Unfelted	
pre-dry section	11-35	Double-felted	Cylinders 16 and 34 are bottom-felted
Pre-MG	35A	Bottom-felted	
MG	35	Top-felted	
1^{st} After-dry section	36-49	Double-felted	
2^{nd} After-dry section	50-56	Double-felted	
1^{st} Correction	57-60	Top-felted	
2^{nd} Correction	61-67	Double-felted	Cylinder 61 is unfelted
Cooling	68-70	Top-felted	

Table 7.1: Summary of the felt configurations used. Note that the numbering corresponds to the cylinders presented in figures 7.1, 7.2 and 7.3.

7.1.2 Configuation of the felts

The configuration of the felt throughout the dryer section can be deduced from figures 7.1,7.2 and 7.3 as well. The information is summarized in table (7.1). As can be seen in the figures, the angle at which the felt approaches the cylinder (i.e. the contact angle) differs throughout the dryer section. In the model, this contact angle is not taken into consideration. Instead, a percentage of the total contact time between the paper web and cylinder is assigned to each cylinder.

7.1.3 Lay-out of the ventilation

The lay-out of the ventilation can also be found in the appendix (figure 7.4). The lay-out distinguishes the smaller dryer sections (Pre-dry section, after-dry section, etc.). As can be seen in the figure, the dry- and wet bulb temperature were measured in order to get information about the temperature and the the humidity of the air flows. However, several air flows were unreachable and measurements were impossible. Every measured flow was assigned a number for convenience. In total, six sections were evaluated: the pre-dry section, the first- and second after-dry section, the infrared dryers and the first- and second correction group. Below, the air flows will be discussed in detail per section using the numbering from figure 7.4.

In the pre-dry section, the supply air is preheated by the exhaust air ($12 > 13$). After being preheated, the hot air is supplied to the pre-dry section through pocket ventilation (14 and 15). The leakage air (16) completes the total air supply to the pre-dry section. Through three ventilators in exhaust air streams 1, 2 and 3, the moist air is transported from the pre-dry section. Subsequently, the moist air is transported through an air-air heat exchanger, where the water vapour releases it latent heat, causing efficient heat transfer to the supply air.

In the after-dry sections, the supply air is preheated by a combination of exhaust air and steam ($17 > 18$ and $20 > 23$), before being transported to the pockets. The leakage air streams in these sections are represented by 19 and 24. The moist air is transported from the after-dry sections through exhaust air streams 5 and 7. Similar to the pre-dry section, the water vapour in the moist exhaust air releases its latent heat to the supply air in an air-air heat exchanger, before being transported to the outside air (6 and 8).

There is no supply air stream to ventilate the infrared dryers sections and both correction groups. This means that only leakage air is used to ventilate these sections. The leakage air is represented by air stream 25. Both infrared dryer sections are ventilated through a single ventilator located in exhaust air stream 9. The first- and second correction group are ventilated through exhaust air streams 10 and 11, respectively.

7.2 Technical specifications and measurements

7.2.1 Basic information

In table 7.2 the basic information on PM2 and the paper grade investigated are reported. The thickness, moisture content and basis weight at the reel were measured with an accurate scanner. No scanner was located at the inlet of the dryer section. Therefore, the reported moisture content at the inlet is only an estimation and prone to error. Detailed information about the cylinder groups and specifications of the speedsizers and coaters can be found in appendices A.12 and A.13.

Specification	Unit	Value
Grade produced		Folding box board
Furnish		100% virgin
Speed	$\left[\frac{m}{min}\right]$	402.39
Trim (Reel)	$[m]$	3.29
Grammage (Reel)	$\left[\frac{kg}{m^2}\right]$	0.23016
Moisture content (Reel)	$\left[\frac{kg}{kg}\right]$ (wet)	0.0713
Dry weight (Reel)	$\left[\frac{kg}{m^2}\right]$	0.21375
Thickness (Reel)	$[\mu m]$	392.94
Moisture content (Inlet)	$\left[\frac{kg}{kg}\right]$ (wet)	0.48
Temperature (Inlet)	$[^\circ C]$	55
Dryer diameters		
• Cylinder 0	$[m]$	0.8
• Cylinder 34	$[m]$	1.8
• Cylinders 48 & 50	$[m]$	1.25
• Pre-MG	$[m]$	3.0
• MG	$[m]$	5.0
• Other cylinders	$[m]$	1.5

Table 7.2: Basic information on the dryer section of the PM2. Values measured on 24 September 2020.

7.3 Mass balances

One of the ways to validate the model is to compare the amount of evaporation measured in the field survey with the amount calculated by the model. The amount of evaporation in a dryer section can be calculated by performing a static mass balance. Two mass balances can be formulated: a total mass balance and a mass balance for water only. It is assumed that no reaction occurs. Furthermore, no accumulation of mass and vapour is assumed. The mass flows that occur in each of dryer sections are shown in figure 7.5a.

7.3.1 Mass flow in air streams

The total mass flow of each stream is a function of the volumetric flow rate and density (eq.(99a)). The volumetric flow rates are omitted here, but given in appendix A.14. These values are approximated from fan specifications located in the air streams.

Note that the volumetric flow rates for streams 14 and 15 are corrected for leakage in the pre-heaters. In these heaters water vapour leaks from the steam side to the supply air streams. This explains the difference in humidity measured between streams 13-14 and 13-15 (see figure 7.4). The dry- and wet bulb temperatures are measured in the different air streams. Using eq.(14) the moisture content is determined. In the air streams, the pressure is assumed to be atmospheric. The density of the air

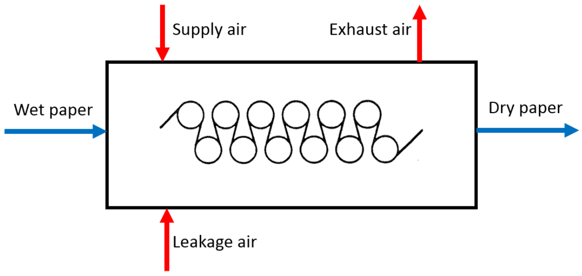

(a) mass flows from- and to a dryer section.

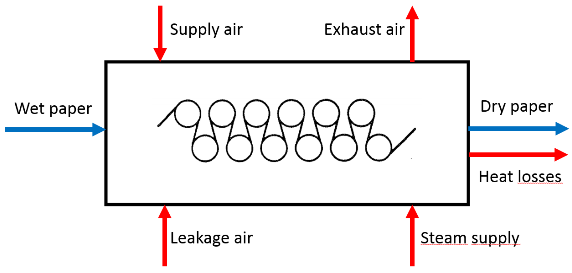

(b) Heat flows from- and to a dryer section.

Figure 7.5: Mass flows 7.5a and heat flows 7.5b occurring in a dryer section

streams can be calculated using eq.(10). The mass flow of water vapour and dry air can be calculated using eq.(99b) and (99c), respectively. The information on the air streams is summarized in table A.14.1.

$$\dot{m}_{tot,\ (i)} = \frac{1}{3600} Q_{(i)} \rho_{(i)} \tag{99a}$$

$$\dot{m}_{w,\ (i)} = \dot{m}_{tot,\ (i)} \left(\frac{x}{1+x} \right) \tag{99b}$$

$$\dot{m}_{da,\ (i)} = \dot{m}_{tot,\ (i)} \left(1 - \frac{x}{1+x} \right) \tag{99c}$$

Where:

- i = Air stream considered
- $\dot{m}_{tot,\ (i)}$ = Total mass flow of air stream considered $\left[\frac{kg}{s}\right]$
- $Q_{(i)}$ = Volumetric flow rate of air stream considered $\left[\frac{m^3}{s}\right]$
- $\rho_{(i)}$ = Density of air stream considered $\left[\frac{kg}{m^3}\right]$
- $\dot{m}_{w,\ (i)}$ = Mass flow of water vapour in air stream considered $\left[\frac{kg}{s}\right]$
- $\dot{m}_{da,\ (i)}$ = Mass flow of dry air in air stream considered $\left[\frac{kg}{s}\right]$
- x = Air humidity $\left[\frac{kg_w}{kg_{d.a.}}\right]$

7.3.2 Mass balances per dryer section

The total mass balance can written according tot eq.(100a). Eq.(100a) can be expanded into eq.(100b) by taking figure 7.5a into account.

$$\dot{m}_{tot,\ (out)} = \dot{m}_{tot,\ (in)} \tag{100a}$$

$$\dot{m}_{tot,\ (paper\ out)} + \dot{m}_{tot,\ (exhaust\ air)} = \dot{m}_{tot,\ (paper\ in)} + \dot{m}_{tot,\ (supply\ air)} + \dot{m}_{tot,\ (leakage\ air)} \tag{100b}$$

Assuming no reaction and accumulation, the vapour mass balance over a dryer section can be written according to eq.(101).

$$\dot{m}_{w,\ (in)} = \dot{m}_{w,\ (out)} \tag{101}$$

Eq.(101) can be expanded into eq.(102a). The evaporation rate over a section can be written according to eq.(102b). Substituting both equations results in eq.(102c).

$$\dot{m}_{w,\ (paper\ out)} + \dot{m}_{w,\ (exhaust\ air)} = \dot{m}_{w,\ (wet\ paper)} + \dot{m}_{w,\ (supply\ air)} + \dot{m}_{w,\ (leakage\ air)} \tag{102a}$$

$$\dot{m}_{evap} = \dot{m}_{w,\ (wet\ paper)} - \dot{m}_{w,\ (paper\ out)} \tag{102b}$$

$$\dot{m}_{evap} = \dot{m}_{w,\ (exhaust\ air)} - \dot{m}_{w,\ (leakage\ air)} - \dot{m}_{w,\ (supply\ air)} \tag{102c}$$

In table 7.3 the dryer section and air stream functions are reported for each air stream. At this point, eqs.(100b) and (102c) can be solved for $\dot{m}_{tot,\ (exhaust\ air)}$ and $\dot{m}_{evap}$ per section. A full calculation of

the mass flows per dryer section can be found in appendix A.15. The mass flows per dryer section are reported in table 7.3.
In the dryer sections it is assumed that the amount of dry solids is unchanged (eq.(103)). This assumption is valid, because chemicals are added in the speedsizer and coaters located in between the different sections. For example, in the fist after-dry section, the dry solids content between in- and outlet is the same. However, the dry solids content at the end of the first after-dry section and at the beginning of the second after-dry section differs. This is because the speedsizer adds solids. The mass flows involving additives are discussed per dryer group in appendix A.15.

$$\dot{m}_{ds,\ (in)} = \dot{m}_{ds,\ (out)} \tag{103}$$

Dryer section	$\dot{m}_{supply}$	$\dot{m}_{leakage}$	$\dot{m}_{exhaust}$	$\dot{m}_{evap}$ $\left[\frac{kg}{s}\right]$	$\dot{m}_{leakage}$ $\left[\frac{kg}{s}\right]$
pre-dryer	14, 15	16	1, 2, 3	2.5624	10.6228
1st After-dry section	18	19	5	0.7532	7.2316
2nd After-dry section	23	24	7	0.4523	5.6988
Coating	N.A.	27	9	0.0324	1.6175
1st Correction	N.A.	25	10	0.0451	5.7173
2e Correction	N.A.	26	11	0.0451	5.7173

Table 7.3: Mass flows per section. The numbers in columns 2,3 and 4 refer to figure 7.4. $\dot{m}_{evap}$ represent the amount of evaporation per dryer section. $\dot{m}_{leakage}$ represents the total amount of leakage air entering a dryer section.

7.3.3 Calculating moisture content per dryer section

In order to calculate the moisture content at the beginning and end of each section, the mass flows of dry solids and water in the paper web should be calculated at the beginning and end of each dryer section. Only the water- and dry solids contents at the reel are known. Therefore, mass flow calculations were performed in upstream direction. This means that the mass flows in the second correction group were evaluated first, while mass flows in the predyer section were evaluated lastly. The moisture content at the in- and outlet of every dryer section can be calculated according to eq.(104). The result is shown in figure 7.6. This is based on data from 24/09/2020.

$$M_{wet} = \frac{\dot{m}_w}{\dot{m}_w\ +\ \dot{m}_{d.s.}} \tag{104}$$

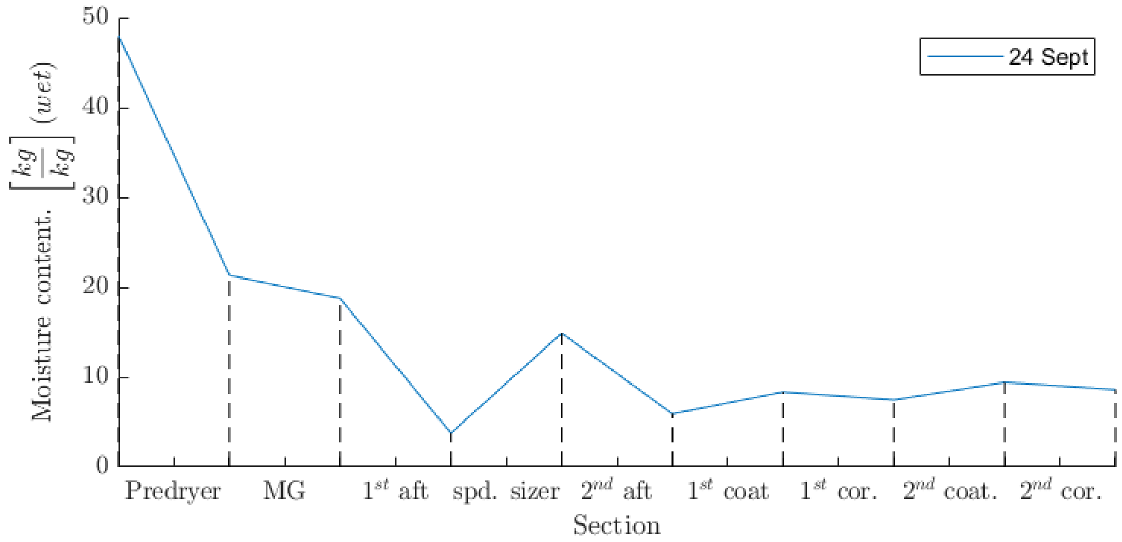

Figure 7.6: Moisture content at the in- and outlet of the different dryer sections based on data from 24/09/2020.

7.4 Heat balance per dryer section

The heat balance per dryer section can be computed in a similar way as the mass balance. The heat flows occurring in each dryer section are shown in figure 7.5b. In this case, the heat consumption per cylinder should be taken into account. This is calculated by using the data provided in table A.12.1. Note that in table A.12.1 there is no information provided on the steam supply to the correction groups. In addition, information was missing on the ventilation of the MG. This means that only a heat balance on the pre-dryer and after-dry sections could be performed. It was concluded that this would provide too little information to be of use.

7.5 Measured temperatures

In total, five types of temperature measurements were performed: paper web temperatures before and after each cylinder, outer cylinder wall temperatures and wet- and dry bulb pocket temperatures. These temperatures are reported in the appendix (table A.16.1 and figure A.16.1). By assuming saturated steam in each cylinder, the steam temperature was derived from the pressure in the cylinder.

7.5.1 Paper web temperatures

Besides an accurate moisture content, an accurate model should also closely follow the measured sheet temperatures. These temperatures are measured directly before and after each cylinder. In this way, two temperature profiles are constructed indicating the sheet temperatures before and after each cylinder. The sheet temperatures were measured as close to the contact points of the paper web and cylinder as possible. However, a distance of approximately $0.3[m]$ was inevitable. This value was also used in the model to represent the measurement points. This distance will be referred to as the temperature measurement distance (TMD). The measured sheet temperatures can be found in table (A.16.1) and are shown in figure A.16.1.

7.5.2 Outer cylinder wall temperatures

The outer cylinder wall temperatures were measured for two reasons. Firstly, together with the steam temperature, the conditions of the cylinder can be determined. A large temperature difference between the steam and cylinder wall temperature indicates that the heat transfer coefficient between steam and cylinder is reduced. This could indicate that the condensate is drained insufficiently or that the cylinder is flooded. The measured values are presented in table(A.16.1) and shown in figA.16.1.

7.5.3 Pocket temperatures

In order to check the humidities in the pockets, the dry- and wet bulb temperatures inside the pockets are measured. By using eqs.(14) the humidities in the pockets is determined. The temperatures and humidities can be found in table A.16.1. Notice that each pocket has the same number as the cylinder right above or below it.

7.5.4 Concluding remarks temperature measurements

As can be seen in figure A.16.1, several temperature measurements are missing. Especially in the first and second after-dry sections, measurements for the cylinder wall are missing. This makes it hard for the model to closely follow the same sheet temperature profile, because these are closely correlated. If a cylinder temperature is missing, it is estimated to be the same as that of cylinders operating at the same steam pressures. In case of missing pocket temperatures, it is assumed to be equal to the previous pocket.
At cylinder 23, the temperature difference between the steam- and the outer cylinder wall is very large. This indicates a large resistance in heat transfer, often caused by a flooded cylinder. Therefore, this cylinder should be checked for malfunctioning.
The warm-up period for the paper web is ten cylinders. This number is quite high and should only be two or three cylinders. This long warm-up period results from unfelted cylinders. These unfelted cylinders give a very slow heating of the web. By applying felts over these cylinders this problem can easily be overcome.

7.6 Concluding remarks on the field survey

The moisture content at the beginning and end of each dryer section will be used in combination with the measured sheet temperatures, in order to validate the model. The moisture content in the paper web is computed by solving mass balances for each dryer section. The sheet temperatures are measured directly before and after each cylinder, resulting in a temperature profile of the paper web. From the measured temperatures it is concluded that cylinder 23 is malfunctioning. In addition, the heating up period of the paper web is too long. This could be reduced by applying felts over the first ten cylinders.

8 Boundary condition validation

In this section the most applicable boundary conditions will be chosen. The boundary conditions which will be investigated can be found in section 5.6. First, a validation case will be defined. Next, the result for each set of boundary conditions will be presented by using the moisture content and temperature profiles. Conservation of mass will be calculated to track the error. Thereafter, the most applicable set of boundary conditions will be chosen. Finally, the order of accuracy will be established.

8.1 Validation case

For validation, a single-sided drying configuration of one cylinder is chosen, because this configuration includes both sets of boundary equations. Validating these boundary conditions for a single-sided drying over one cylinder automatically means they apply for the whole drying section, because no other boundary conditions occur.
Reardon [11] proposed two sets of boundary conditions as defined in eqs.(61) and (62). Nasrallah [16] proposed the boundary conditions in eqs.(63) and (64). For the validation case, it is assumed that the total pressure difference across the paperweb is negligible. This means means that eqs. (61d), (62d), (63c) and (64c) do not apply.
At this point, it is important to recall that the boundary conditions proposed by Reardon were solved at the differential level, while the boundary conditions proposed by Nasrallah were solved at intergral level.

8.1.1 Conservation of mass

For both sets of boundary conditions, conservation of mass should apply. This means that mass transferred over the boundaries of the sheet during a single time step should be equal to the difference between the moisture content before and after each timestep. After each timestep, this balance is computed and should be within the allowable limits. The mass transferred over the boundaries of the sheet per time step can be calculated according to eq.(105). The average moisture content is calculated using the midpoint rule. Notice that this numerical integration rule is second order. This is necessary, because the model is second order accurate in the spatial domain as well.

$$\dot{m}_{evap,\,(step)} = \frac{h_m^{j+1}\left(\rho_{(0)}^{j+1} - \rho_{pocket}^{j+1}\right) + h_m^{j}\left(\rho_{(0)}^{j} - \rho_{pocket}^{j}\right)}{2}\, dt \tag{105}$$

In this equation, $\rho_{(0)}$ represents the density of the vapour just above the sheet. The validation case will have an initial moisture content and temperature of 0.923 $\left[\frac{kg}{kg}\right]$ (dry) and 50 $[^{\circ}C]$, respectively, and will be run for 0.5 seconds. The heat- and mass transfer coefficients and pocket conditions are assumed to be constant. At this moisture content, the sorptive behaviour does not occur. Therefore, the porostiy, thickness, basis weight, are assumed to be constant. Furthermore, the isotherm and heat of sorption are not relevant at this high moisture content.

8.2 Results

8.2.1 Boundary conditions proposed by Reardon

In figure 8.1, the outcome of applying Reardon's boundary conditions is shown. The open side, represented by eqs.(61), is located at thickness $y = 0[m]$. The heated cylinder, represented by eqs.(62), is located at thickness $y = 0.001[m]$. Ghost points were used to solve the model. The value of the capillary pressure at the ghost points is plotted along with the other nodes. Several conclusions can be drawn from the result.

8.2.1.1 Diverging solution for increasing nodes

From the moisture profile it can be seen that the solution does not converge towards a specific profile. For an increasing number of nodes in the spatial domain, the moisture content profile starts to diverge

at the open side of the paper web.
This is due to boundary condition specified for the capillary pressure at the open side (eq.(61c)). According to Reardon [11], eq.(61c) was derived on the premise that the sheet does not offer any resistance to mass transfer from the web. However, he may have overlooked the convergence of his model when adopting this assumption. In this model, a correlation presented by Brooks and Corey [10] was used to compute the capillary pressure directly from moisture content. This explains the diverging behaviour in the capillary pressure profile.

8.2.1.2 Loss of mass

A valid model should obey the conservation equations. However, it can be seen in figure 8.1 that conservation of mass is not satisfied. The error is calculated according to eq.(106), which is the amount transferred over the boundaries subtracted from the difference between the initial and current moisture content. The moisture content is calculated using the midpoint rule.

$$Error = [M_{initial} - M_{midpoint}] - \frac{M_{evap}}{b_{wt}} \tag{106}$$

Where:

- $Error$ = Error in mass balance $\left[\frac{kg}{kg}\right]$ (dry)
- $M_{initial}$ = Initial moisture content $\left[\frac{kg}{kg}\right]$ (dry)
- $M_{midpoint}$ = Moisture content calculated via the midpoint rule $\left[\frac{kg}{kg}\right]$ (dry)
- M_{evap} = Water evapourated from the web $\left[\frac{kg_{water}}{m^2}\right]$ (dry)
- b_{wt} = Basis weight of the sheet $\left[\frac{kg_{fibres}}{m^2}\right]$ (dry)

From figure 8.1 it can be seen that a positive error is encountered for an increasing number of nodes. This means that water also leaves the paper web in another way than diffusion. This additional flow of moist can be explained by looking at the pressure gradient occurring at the open side of the paper: this gradient causes a flow of liquid water according to eq.(51).

8.2.1.3 Contradicting boundary conditions

At the heated side, the capillary pressure profile shows a discontinuity at the boundary. When using ghost points, it is imperative that the ghost points are approached in a smooth way, so that the profile becomes a smooth function. In this case, contradicting boundary conditions prevent this from happening.
As mentioned before, the density of the vapour can be approximated by combining the reduced vapour pressure (eq.(54)) with the ideal gas law (eq.6c). Therefore, the density of the vapour can be written as a function of the moisture content and the temperature.
As described in section 5.4.1 the capillary pressure is a function of the moisture content and the temperature as well. Reardon [11] proposes three boundary conditions, while all derivatives can be written as a function of two variables: the moisture content and the temperature. Therefore, it can be concluded that Reardon prescribes one boundary conditions too much, resulting in contradicting boundary conditions.

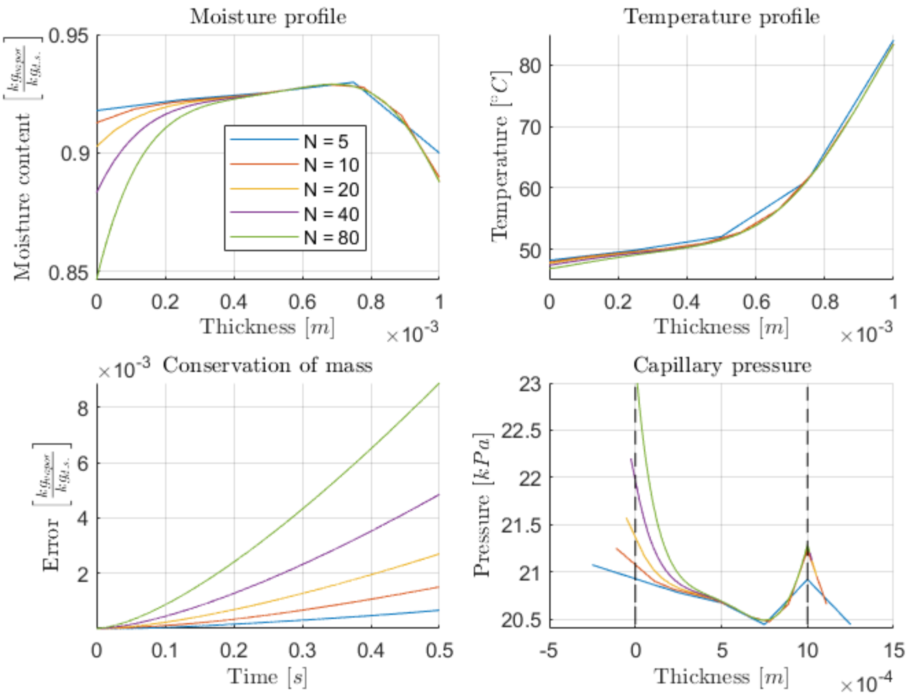

Figure 8.1: Moisture content, temperature and capillary pressure profiles for different numbers of nodes, when applying Reardon's [11] boundary conditions. Also the error in the mass balance is shown. The validation case was run for $0.5[s]$ with a time step of $0.001[s]$. Note the diverging behaviour for the moisture content and for the capillary pressure profiles. In addition, the error in the mass balance becomes significant for an increasing number of nodes.

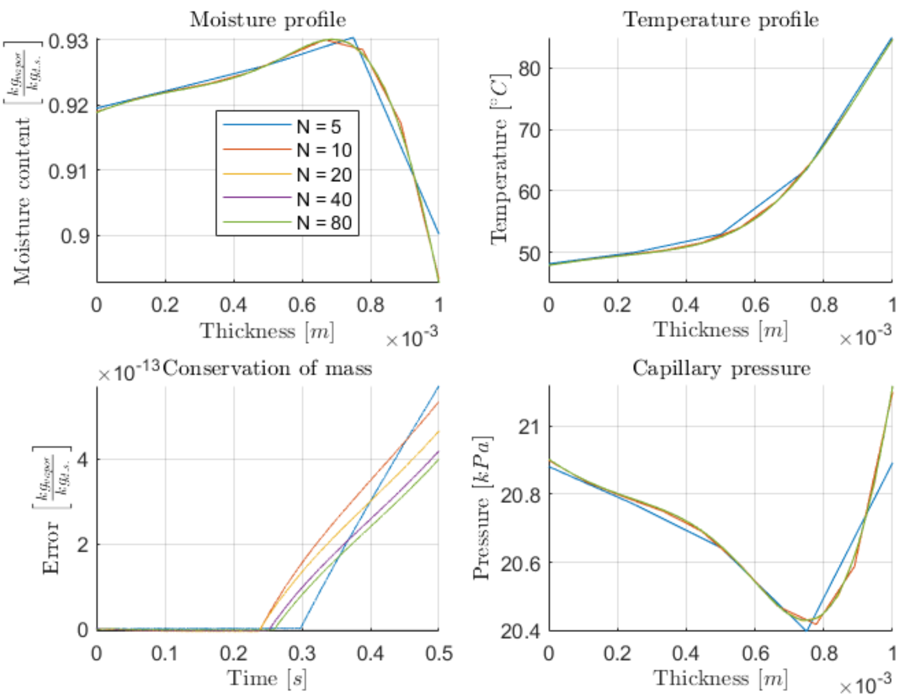

Figure 8.2: Moisture content, temperature and capillary pressure profiles for different numbers of nodes, when applying the set of boundary conditions proposed by Nasrallah et al. [16]. Also the error in the mass balance is shown. The model converges for increasing number of nodes. Also the mass balance is negligible.

8.2.2 Boundary conditions proposed by Nasrallah

Figure 8.2 shows the results when applying Nasrallah's boundary conditions (eqs.(63) and (64)). The surface open to evaporation and the heated surface are located at thickness $y = 0[m]$ and $y = 0.001[m]$, respectively. It can be seen that the moisture content converges for an increasing number of nodes. Furthermore, the error in the mass conservation equation is negligible. In this case, no contradicting boundary conditions are prescribed, because only two boundary conditions are prescribed: for the temperature and the moisture content.

8.2.3 Concluding remarks

For an increasing number of nodes, the solution should converge to a particular solution, while still obeying the conservation equations. The set of boundary conditions proposed by Reardon [11] showed a diverging and contradicting behaviour. In addition, the conservation equations could not be obeyed. The boundary conditions proposed by Nasrallah et al. [16]were proven to be appropriate. Therefore, the boundary conditions proposed by Nasrallah et al. [16] will be used in the present model.

8.3 Order of accuracy

The boundary conditions proposed by Nasrallah et al. [16] were discretized according to section 5.7.1, which should result in a second order accurate model in time and space. In this section, the order of accuracy is evaluated. In this case, the moisture content is evaluated at six points ($y = 0$,$y = 0.2$,...,$y = 1$) and its convergence is checked.

8.3.1 Order of accuracy in space

In order to check the order of accuracy in space, six different spatial resolutions are evaluated. By doubling the number of nodes, the distance between the nodes (Δy) is halved. In this case, the exact solution is unknown. Nevertheless, for an increasing number of nodes and a small timestep, the moisture content should asymptotically approach a final value. It should be evaluated how fast this asymptotic value is approached. This can be done using eq.(107).

$$2^\alpha = \frac{J_{(N)} - J_{(2N)}}{J_{(2N)} - J_{(4N)}} \tag{107}$$

Where:
- α = Order of accuracy in spatial domain
- J = Solution at a certain location depending on number of nodes
- N = Number of nodes

Note that it is impossible to evaluate the same point when doubling the number of grid points. The number of nodes evaluated will be 6, 11, 21, 41, 81, 161. For a larger number of nodes the order should still approach 2.

In table, 8.1 moisture contents for increasing number of nodes is shown at different locations in the sheet. Eq.(107) is used to calculate the order of accuracy in the spatial domain. From table 8.2 it can be seen that the order to the scheme approaches 2 asymptotically for an increasing number of nodes. Therefore, it is concluded that the scheme is second order accurate in space. For these calculations a time step of $5 \times 10^{-5}[s]$ was chosen.

J_N	Location of point					
	y=0	y=0.2	y=0.4	y=0.6	y=0.8	y=1
N=6	0.919253	0.922165	0.924380	0.928463	0.928713	0.896301
N=11	0.918924	0.921952	0.924224	0.928691	0.927029	0.893141
N=21	0.918853	0.921888	0.924180	0.928756	0.926498	0.892791
N=41	0.918836	0.921871	0.924169	0.928770	0.926367	0.892711
N=81	0.918831	0.921867	0.924166	0.928773	0.926334	0.892691
N=161	0.918830	0.921866	0.924166	0.928774	0.926326	0.892686

Table 8.1: Value of the moisture content $\left[\frac{kg}{kg}\right]$ (dry) at specific locations in the paper web. At every point the value of the moisture content, J_N, converges to a certain value asymptotically for an increasing number of nodes. A time step of 0.05 milliseconds was chosen.

$\log_2\left(\frac{J_{(N)} - J_{(2N-1)}}{J_{(2N-1)} - J_{(4N-3)}}\right)$	Location of point					
	y=0	y=0.2	y=0.4	y=0.6	y=0.8	y=1
N=6	2.2126	1.7355	1,8348	1.8287	1.6645	3.1734
N=11	2.0586	1.9272	2.0351	2.1468	2.0180	2.1270
N=21	2.0128	1.9809	2.0175	2.0641	2.0083	2.0263
N=41	2.0031	1.9949	2.0029	2.0198	2.0025	2.0065

Table 8.2: Order of accuracy in space. Eq.(107) is used to determine the order of accuracy. For an increasing number of nodes, second order accuracy in space is obtained. A time step of 0.05 milliseconds was chosen.

8.3.2 Order of accuracy in time

The exact same reasoning applies to check the order of accuracy in time. For decreasing time steps, a unique value should be approached. Eq.(107) should be modified to eq.(108):

$$2^{\alpha} = \frac{J_{(\Delta t)} - J_{(\frac{\Delta t}{2})}}{J_{(\frac{\Delta t}{2})} - J_{(\frac{\Delta t}{4})}} \tag{108}$$

The results are shown in tables 8.3 and 8.4. In this case,the difference in the moisture content between time steps is reported, because of the very small differences in moisture content. These small differences approach machine accuracy, causing the accuracy in time to differ slightly from second order. Still, it can be concluded that the scheme is second order accurate in time. For these calculations 41 nodes were used.

$J_{\Delta t} - J_{\frac{\Delta t}{2}}$	Location of point					
	y=0	y=0.2	y=0.4	y=0.6	y=0.8	y=1
$\Delta t = 0.0016$	2.66e-06	7.86e-07	-6.22e-06	-1.04e-05	1.17e-05	1.12e-05
$\Delta t = 0.0008$	-1.89e-09	-1.32e-09	7.39e-09	1.96e-08	-1.29e-08	-1.87e-08
$\Delta t = 0.0004$	-4.63e-10	-2.78e-10	2.10e-09	5.28e-09	-3.61e-09	-5.13e-09
$\Delta t = 0.0002$	-1.21e-10	-7.07e-11	6.43e-10	1.36e-09	-1.07e-09	-1.28e-09
$\Delta t = 0.0001$	-2.36e-11	-7.79e-12	9.82e-11	3.60e-10	-1.84e-10	-3.97e-10

Table 8.3: Difference in moisture content $\left[\frac{kg}{kg}\right]$ (dry) for different timesteps at specific locations in the paper web. The calculating were performed with 41 nodes.

$\log_2\left(\frac{J_{\Delta t} - J_{\frac{\Delta t}{2}}}{J_{\frac{\Delta t}{2}} - J_{\frac{\Delta t}{4}}}\right)$	Location of point					
	y=0	y=0.2	y=0.4	y=0.6	y=0.8	y=1
$\Delta t = 0.0016$	-	-	-	-	-	-
$\Delta t = 0.0008$	2.0331	2.2495	1.8156	1.8905	1.8342	1.8636
$\Delta t = 0.0004$	1.9307	1.9757	1.7070	1.9520	1.7597	1.9987
$\Delta t = 0.0002$	2.3640	3.1832	2.7100	1.9198	2.5365	1.6929

Table 8.4: Order of accuracy in time. Eq.(108) is used to determine the order of accuracy. For decreasing time steps, second order accuracy in time is obtained. The moisture content differences between time step sizes approach machine accuracy. Therefore, the order of accuracy may not fully approach 2 for very small time steps. The calculations were performed with 41 nodes.

8.3.3 Concluding remarks on the accuracy

It has been proven that the numerical method has second order accuracy in space and time. Furthermore, the chosen time steps result in very small differences in the moisture content. Therefore, larger time steps might be chosen, while still keeping sufficient accuracy.

9 Parameter selection

Several correlation and values for numerous transport properties have been proposed. In this section these will be tested and validated against data from the field survey. Firstly, the test criteria to examine the fitness of various parameters will be described. Next, the various transport correlations and values are summarized. Subsequently, the procedure for the parameter selection is explained. Lastly, an overview of the chosen correlations and parameters is given.
However, there is one problem that needs addressing first: the model does not cover transport phenomena that capture the effect of adding chemical additives to the web. When adding additives, the permeability, thermal conductivity, porosity, tortuosity and other properties at the outer sides of the paper web change, affecting the overall transport of heat and mass. Therefore, this model can only be tested and validated against dryer sections where no additives are added. This is only the case in the pre-dry and MG section only. In th epresent study, it was chosen to test the model against the pre-dry section only, because only limited data are available for the MG section.
The estimated average moisture content at the beginning of the pre-dry section was estimated to be $0.923 \left[\frac{kg}{kg}\right] (dry)$ or $0.480 \left[\frac{kg}{kg}\right] (wet)$. At the end of the pre-dry section the average moisture content was estimated to be $0.271 \left[\frac{kg}{kg}\right] (dry)$ or $0.213 \left[\frac{kg}{kg}\right] (wet)$.

9.1 Test criteria

Two test criteria are used to asses the fitness of the different transport properties: the sheet temperatures and the moisture content.

9.1.1 Sheet temperatures

The sheet temperatures in the field survey were measured before and after each cylinder. By adapting the model to specifications from the field survey, calculated the sheet temperatures should closely match the measured sheet temperatures. The temperature measurement distance (TMD) was approximated to be $0.3[m]$. Therefore, this distance should be taken into account when comparing measured sheet temperatures to calculated ones. Two temperature profiles are constructed: one comparing sheet temperatures before each cylinder and the other comparing sheet temperatures after each cylinder. A mean average error (MAE) is used to assess how well the calculated temperature profiles follow measured values. A MAE is provided for each temperature profile.

$$MAE = \frac{\sum_{i=1}^{n} |T_{calc}(i) - T_{meas}|}{n} \tag{109}$$

In this case, n, T_{calc} and T_{meas} represent the number of cylinders, calculated sheet temperatures and measured sheet temperatures, respectively.

However, there is a significant disadvantage when using sheet temperature measurements as test criteria. The error on these measurements can be significant. The temperatures were measured using a infra red thermometer. The hot surroundings may have affected the temperature readings, due to the emission of the radiative heat. Furthermore, a TMD of $0.3[m]$ was only an approximation and, therefore, differs per cylinder.
Due to possible inaccurate measurements, the sheet temperature is considered as secondary test criterion. This means that the moisture content is checked for various parameters first. Afterwards, the calculated sheet temperatures are compared to the measured values.

9.1.2 Moisture content

A better way to test the different transport parameters is to check the moisture content at the end of the pre-dry section. By applying mass balances, the moisture content at the end of this dry section is determined. This value should closely match the value based on data from the field survey.

The average moisture content at the end of the pre-dry section if referred to as the final moisture content. The average moisture content is defined as the weighted sum of moisture content for each slice (see fig.(5.7)):

$$M_{av} = \frac{\sum_{i=2}^{n-1} M(i)dy \ + \sum_{i=1,n} M(i)\frac{dy}{2}}{L} \tag{110}$$

In this case, M_{av}, $M(i)$, n and dy represent the average moisture content, moisture content of each individual slice, number of slices and thickness of a slice, respectively.
Based on data from the field survey, the average moisture content after the pre-dry section was determined to be 0.271 $\left[\frac{kg}{kg}\right]$ (dry). The error in the moisture content is calculated according to:

$$M_{error} = |M_{av} \ - \ 0.271| \tag{111}$$

9.2 Possible transport correlations

As described in previous sections, multiple correlations can be applied to the different transport properties. In this section, an overview of these correlations per transport property is provided.

1. For the contact heat transfer coefficient between the paper web and cylinder, h_c, three possible correlations were found:

- Yeo et al. [23] $$\frac{h_c}{4184} = 0.1661e^{1.512M} - 0.4775e^{-15.67M} \tag{94}$$
- Rhodius and Ghörring [88] $$h_c = 1556.6M + 52.87 \tag{95}$$
- Reardon [11] $$h_c = 186M + 597 \tag{97b}$$

2. For the relative permeability of the wetting phase, k_w, two possible correlations were found:

- Brooks and Corey [10] $$k_w = S^{*\left(\frac{2+3\lambda}{\lambda}\right)} \tag{81a}$$
- Robertson [75] $$k_w = \begin{cases} \left(4.51 \times 10^{-12}\right) e^{(25.86S)}, & 0.82 < S \leq 1 \\ \left(6.93 \times 10^{-6}\right) e^{(8.54S)}, & 0.36 < S \leq 0.82 \\ \left(1.0 \times 10^{-11}\right) e^{(46.05S)}, & 0.15 < S \leq 0.36 \\ 0, & 0 < S \leq 0.15 \end{cases} \tag{95}$$

3. For the relative permeability of the non-wetting phase, k_{nw}, three possible correlations were found:

- Brooks and Corey [10] $$k_{nw} = (1 - S^*)^2 \left[1 - S^{*\left(\frac{2+3\lambda}{\lambda}\right)}\right] \tag{81b}$$
- Hashemi [76] $$k_{nw} = 1 - 0.52(M_{free})^{1.35} \tag{84a}$$
- Asensio [1] $$k_{nw} = a + \frac{b}{1 + \left(\frac{(M - M_{FSP})}{c}^{d}\right)} \tag{86c}$$

4. For the capillary pressure, P_c, two possible correlations were found:

- Brooks and Corey [10] $$P_c = p_e S^{*\left(\frac{1}{\lambda}\right)} \tag{45a}$$
- Asensio [1] $$P_c = c\left(\frac{b}{M_{tot} - M_{FSP}} - 1\right)^{\frac{1}{d}} \tag{46a}$$

5. For the diffusibility, $\frac{D_{eff}}{D_v}$, two possible correlations were found:

- Hartley and Richards [51] $$\frac{D_{eff}}{D_v} = \Psi\epsilon(1-S) \tag{6.2}$$
- Ramaswamy [24] $$\frac{D_{eff}}{D_v} = \begin{cases} 0.4\dfrac{\epsilon^{1.23}}{\exp\{1.574S\}}, & 0 < S \leq 0.7 \\ \dfrac{\epsilon^{1.23}(1-S)^{1.08}}{4.33-3.33S}, & 0.7 < S \leq 1 \end{cases} \tag{6.2}$$

6. To simulate the mass transfer from the sheet, two theories were proposed:
- Low mass transfer theory $$N_{1,s} = h_m(\rho_{1,s} - \rho_{1,e}) \tag{27b}$$
- High mass transfer theory $$N_{1,s} = \frac{h_m P_{tot}}{R_v T} ln\left(\frac{P_{tot} - P_{v,e}}{P_{tot} - P_{v,s}}\right) \tag{32}$$

No clear values were reported for the absolute permeability (K), FSP and fixed remaining partial pressure of air (P_{air}). Therefore, a range of applicable values for each of these properties is investigated as well. These values can be found in table 9.1.

Property			Value		
Absolute permeability	K	$[m^2]$	30×10^{-15}	100×10^{-15}	$300 * 10^{-15}$
FSP	M_{FSP}	$\left[\frac{kg}{kg}\right]$ (dry)	0.2	0.3	0.4
Partial pressure of air	P_{air}	$[kPa]$	0.1	0.01	

Table 9.1: Values for different properties.

9.3 Procedure for parameter selection

The correlations and parameters proposed above are all dependent on each other. In order to test the sensitivity of each individual parameter, a significant computational time is required. In order to cross-check every component, $2^5 * 3^4 = 2592$ simulations would have to be run. With an estimated average computational time of 45 minutes per simulation, the total required computational time would be 1944 hours or 81 days. In order to reduce the computational time, a procedure was followed to find the optimal parameters. This procedure involves cross-checking multiple parameters, while keeping other parameters constant.

First, it was investigated if there exists a significant difference between the different mass transfer theories. Next, the sensitivity of the correlations for the contact heat transfer coefficient, relative permeabilities and capillary pressure was evaluated. All other correlations and values were kept constant. According to Sadeghi [22], the moisture content and sheet temperatures are less sensitive to the diffusibility of the vapour. Therefore, these correlations were evaluated lastly. Once the right correlations are obtained, the model needs calibration to match the measured values as close as possible. Therefore, last cross-check was performed for different values of the absolute permeability, FSP and the partial pressure of air.

9.4 The effect of the mass transfer theory

In table 9.2, final moisture contents are reported for different values of the remaining partial pressure of air, the FSP and the absolute permeablity. Furthermore, the two mass transfer theories are incorporated.

In these simulations the contact heat transfer correlation given by Rhodius and Göttching [88] was used. For the capillary pressure and relative permeabilities of the wetting and non-wetting phase, correlations proposed by Brooks and Corey [10] were used. For the diffusibility the correlation proposed by Hartley and Richards [51] was used. From these data several conclusions can be drawn.

Firstly, the value for the remaining partial pressure of air does not affect the calculated average moisture content for the correlations used. This does not mean that this value can be chosen arbitrarily for any correlation. For this particular set of correlations used, the maximum vapour pressure rises above atmospheric only during a very short time, limiting the influence of the remaining partial pressure of air. Note that for other correlations, this value may have considerable influence, because the remaining partial pressure of air may exceeds the atmospheric pressure more often.

The distinction between the high and low mass transfer theory is of importance here. High mass transfer theory results in lower final moisture contents, indicating that the convective component in the evaporating process cannot be neglected.
Furthermore, the difference between these theories may become even more significant if other fixed correlations were chosen. Therefore, future simulations will only be run by using high mass transfer theory.

Furthermore, it can be seen that the model gives a lower moisture content for increasing absolute permeability and decreasing FSP. The values reported in table 9.2 are well above the final moisture content determined in the field survey ($0.271 \left[\frac{kg}{kg}\right] (dry)$). Therefore, the FSP will probably be relatively low, while the absolute permeability will be relatively high. To determine better values for the FSP and absolute permeability, the sensitivity of other correlations is checked first.

		Low mass trans. theory			High mass trans. theory		
M_{dry} $\left(\left[\frac{kg}{kg}\right] (dry)\right)$		K $(\times 10^{-15})$ $\left[m^2\right]$			K $(\times 10^{-15})$ $\left[m^2\right]$		
		30	100	300	30	100	300
$P_{air} = 0.1[kPa]$	$M_{FSP} = 0.2 \left[\frac{kg}{kg}\right] (dry)$	0.48	0.47	0.47	0.43	0.42	0.41
	$M_{FSP} = 0.3 \left[\frac{kg}{kg}\right] (dry)$	0.50	0.48	0.47	0.48	0.45	0.43
	$M_{FSP} = 0.4 \left[\frac{kg}{kg}\right] (dry)$	0.55	0.53	0.50	0.53	0.50	0.48
$P_{air} = 0.01[kPa]$	$M_{FSP} = 0.2 \left[\frac{kg}{kg}\right] (dry)$	0.48	0.47	0.47	0.43	0.42	0.41
	$M_{FSP} = 0.3 \left[\frac{kg}{kg}\right] (dry)$	0.50	0.48	0.47	0.48	0.45	0.43
	$M_{FSP} = 0.4 \left[\frac{kg}{kg}\right] (dry)$	0.55	0.53	0.50	0.53	0.50	0.48

Table 9.2: Final moisture contents ($\left[\frac{kg}{kg}\right] (dry)$) for different values of the FSP, the absolute permeability, the remaining partial pressure of air and different mass transfer theories.

M_{dry} $\left[\frac{kg}{kg}\right]$ (dry)	k_w	Robertson			Brooks and Corey		
P_c	h_c / k_{nw}	Hashemi	Brooks and Corey	Asensio	Hashemi	Brooks and Corey	Asensio
Brooks and Corey	Yeo et al.	0.61	0.61	0.61	0.38	0.38	0.38
	Rhodius and Göttsching	0.68	0.68	0.68	0.45	0.45	0.45
	Reardon	0.62	0.62	0.62	0.50	0.50	0.50
Asensio	Yeo et al.	0.61	0.61	0.61	0.38	0.38	0.38
	Rhodius and Göttsching	0.68	0.68	0.68	0.45	0.45	0.45
	Reardon	0.62	0.62	0.62	0.50	0.50	0.50

Table 9.3: Final moisture contents ($\left[\frac{kg}{kg}\right]$ (dry)) for different capillary pressure, (non-)wetting relative permeability and contact heat transfer coefficient correlations. In this case, Hartley and Richards' diffusibility correlation was used. In these simulations P_{air}, M_{FSP} and K, were fixed at 0.1 $[kPa]$, 0.3 $\left[\frac{kg}{kg}\right]$ (dry) and $100 \times 10^{-15}[m^2]$, respectively.

M_{dry} $\left[\frac{kg}{kg}\right]$ (dry)	k_w	Robertson		Brooks and Corey	
M_{FSP} $\left[\frac{kg}{kg}\right]$ (dry)	K $[m^2]$ / $\frac{D_{eff}}{D_{tot}}$	Hartley and Richards	Ramaswamy	Hartley and Richards	Ramaswamy
0.2	100×10^{-15}	0.54	0.57	0.33	0.38
	300×10^{-15}	0.51	0.54	0.31	0.37
0.3	100×10^{-15}	0.61	0.64	0.38	0.42
	300×10^{-15}	0.60	0.62	0.36	0.40

Table 9.4: Final moisture contents ($\left[\frac{kg}{kg}\right]$ (dry)) for different diffusibility and wetting relative permeability correlations. These correlations are evaluated for different FSP and absolute permeability values. In this case, Brooks and Corey's [10] correlations were used for the capillary pressure and the non-wetting relative permeablitiy. Yeo et al.'s [23] equation was used for the contact heat transfer coefficient. The remaining partial pressure of air was fixed at 0.1 $[kPa]$.

9.5 The effect of relative permeabilities

In table 9.3, the final moisture contents at the end of the pre-dry section are reported for the (non-)wetting relative permeability, capillary pressure and contact heat transfer correlations. In these simulations P_{air}, M_{FSP} and K, were assumed to be 0.1 $[kPa]$, 0.3 $\left[\frac{kg}{kg}\right]$ (dry) and $100 \times 10^{-15}[m^2]$, respectively. From these data several conclusions can be drawn regarding the relative permeabilities.

9.5.1 Relative permeability of the wetting phase

As can be seen from table 9.3, there exists a large difference in moisture content between the correlations proposed for the wetting relative permeability. This phenomenon can be explained by the following reasoning.
From figure 6.4a it can be seen that the correlation proposed by Robertson [75] approaches zero at a higher moisture content. This means that the capillary movement is reduced already at a high moisture content (eq.(51)). On the cylinder side, the capillary transport tries to balances the evaporated water. When the capillary flow is reduced, the moisture content drops, resulting in larger moisture contents gradients. According to figure 6.6, the contact heat transfer coefficient between the paper web and the cylinder is reduced for low moisture content. Therefore, reducing the capillary flow affects

the heat transfer coefficient negatively. Subsequently, if less heat is supplied to the paper web, the temperature rise is minimal and so will be the increase in saturated vapour pressure. This results in less mass transfer from the sheet.

In figure 9.1 this process can be seen. Large gradients in the moisture content profile are reported for Robertson's [75] correlation. This ultimately results in lower vapour pressures in the sheet.

At this point it is too early to reject Robertson's correlation, because other parameters may be of influence as well. Therefore, correlations for the wetting relative permeability and diffusibility need to be cross-checked as well. In table 9.4 this cross-checking is performed. In this case the influence of a lower FSP and a higher absolute permeability are included. By adjusting these values, the transport in the sheet is enhanced, making it easier for moist to reach the surface of the paper web and to evaporate.

In these simulations the remaining partial pressure of air was fixed at 0.1 [kPa]. The correlations proposed by Brooks and Corey [10] were used for the capillary pressure and the non-wetting relative permeability. Yeo et al.'s [23] equation was used for the contact heat transfer coefficient.

From table 9.4 it becomes clear that Robertson's correlation for the wetting relative permeability grossly overestimates the final moisture content. Although the values for the FSP and absolute permeability were set to enhance the capillary effect, the final moisture content is almost twice the measured value. Using Robertson's correlation, the total pressure in the web did no exceed atmospheric values at any time in the drying process.. Therefore, changing the non-wetting relative permeability correlation used will not affect the outcome.

In this case, the calculated sheet temperatures are not compared to the measured value, because the calculated final moisture content is grossly overestimated. The correlation proposed by Brooks and Corey [10] for the wetting relative permeability will be used in future calculations.

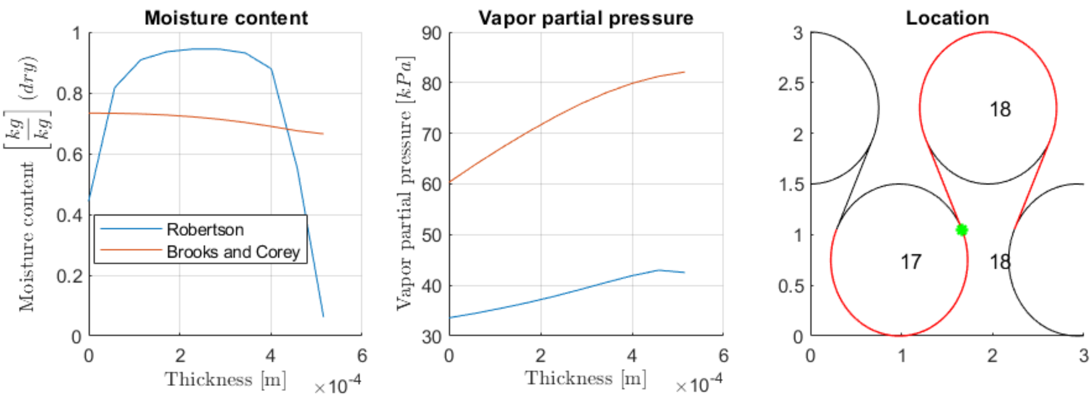

Figure 9.1: Moisture content and vapour pressure profiles for both correlations proposed for the wetting relative permeability.

9.5.2 Relative permeability of the non-wetting phase

By looking at table 9.3, varying the non-wetting relative permeability does not affect the final moisture content, because constant values for the non-wetting relative permeability are reported. This can be explained by evaluating the amount of time the total pressure in the sheet exceeds atmospheric pressure. For the correlations used, the atmospheric pressure is exceeded only 1% of the time, meaning that convective vapour flow is enabled only for a very short duration during drying. Therefore, the effect of the non-wetting relative permeability is minimal.

However, by choosing different fixed parameters, the total pressure may exceed atmospheric more often. In table 9.4, the influence of other parameters was investigated. When using Brooks and

Corey's [10] wetting relative permeability correlation in combination with Ramaswamy's [24] diffusibility correlation, the atmospheric pressure is exceeded the most (7 to 10% of the total drying time depending on the absolute permeability and the FSP). This is a considerable amount and it is important to investigate the effect of varying the non-wetting relative permeability correlation.

This is done in table 9.5. Besides the effect of the non-wetting relative permeability correlation, also the effect of the remaining partial pressure of air is reported. Although, the atmospheric pressure was exceeded 7 to 10% of the total drying time, the non-wetting relative permeability and the remaining partial pressure of air showed negligible influence.

M_{dry} $\left[\frac{kg}{kg}\right]$ (dry) / $P_{air}[kPa]$ \ k_{nw}	Hashemi	Brooks and Corey	Asensio
0.1	0.3716	0.3729	0.3720
0.01	0.3718	0.3730	0.3722

Table 9.5: Final moisture contents for different non-wetting relative permeability correlations. In this case, Ramaswamy's [24] diffusibility correlation and Brooks and Corey's [10] wetting relative permeability were used.

9.5.3 Concluding remarks on relative permeability

Between the wetting relative permeability correlations, there exists a large difference in moisture content. The correlation for the wetting relative permeability proposed by Brooks and Corey [10] was favorable, because the capillary transport remained significant at lower moisture content. This prevents steep moisture gradients from occurring, resulting in final moisture contents closer to the measured values.

The non-wetting relative permeability was found to have a negligible influence on the final moisture content. Although convective vapour flow occurred up to 10% of the drying time for some correlation combinations, the final moisture content remained unaffected.

9.6 The effect of contact heat transfer coefficient

Table 9.3 also shows the effect of applying different contact heat transfer coefficient correlations. Regardless of the capillary pressure correlation chosen, the correlation proposed by Yeo et al. [23] gives the lowest final moisture content. By looking at figure 6.6, the correlation proposed by Yeo et al. [23] provides higher values for the contact heat transfer coefficient at all moisture contents, ensuring more heat flow into the sheet. This results in more evaporation and, thus, a lower final moisture content.

In figure 9.2 temperature profiles calculated before and after each cylinder are shown with their corresponding mean average error (MAE). Yeo et al.'s [23] correlation provides the lowest MAE overall. However, it can be noted that for the first 7 felted cylinders, the temperature after each cylinder is overestimated. At these cylinders the moisture content is still significant. According to figure 6.6, this results in high heat transfer coefficients, explaining the overestimation of the temperature.

Nevertheless, the correlation proposed by Yeo et al. [23] will be used in future calculations.

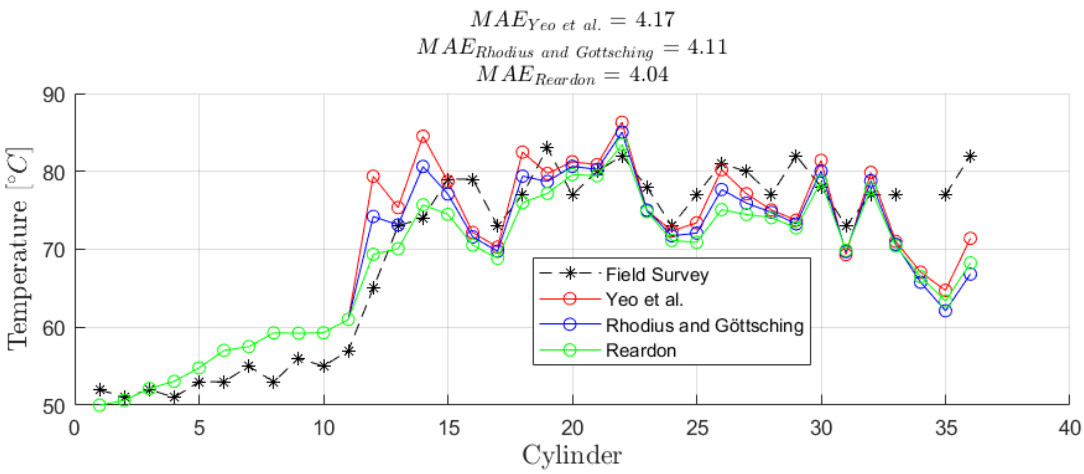

(a) Temperature profile before each cylinder

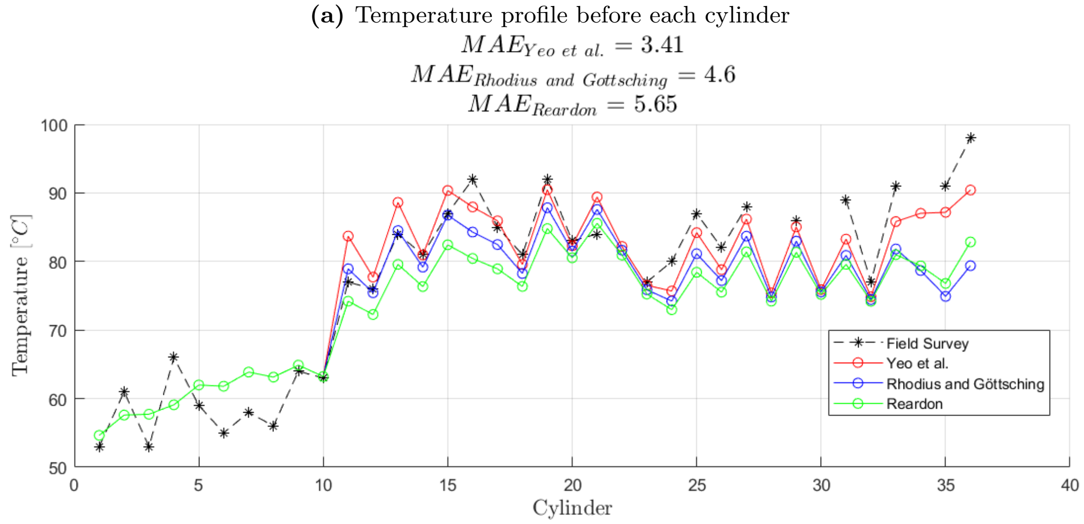

(b) Temperature profile after each cylinder

Figure 9.2: Temperature profiles in the dryer section for different contact heat transfer coefficient correlations. Correlations proposed by Brooks and Corey [10] were used for the relative permeabilities and the capillary pressure.

9.7 The effect of the capillary pressure correlation

In figure 5.4 capillary pressure correlations as function of moisture content are shown. Both correlations provide the same final moisture content (see table 9.3). This can also be seen in both temperature profiles in figure 9.3. The temperature profiles coincide at almost all points. As there exists almost no difference, it was chosen to use the correlation proposed by Brooks and Corey [10] for future calculations.

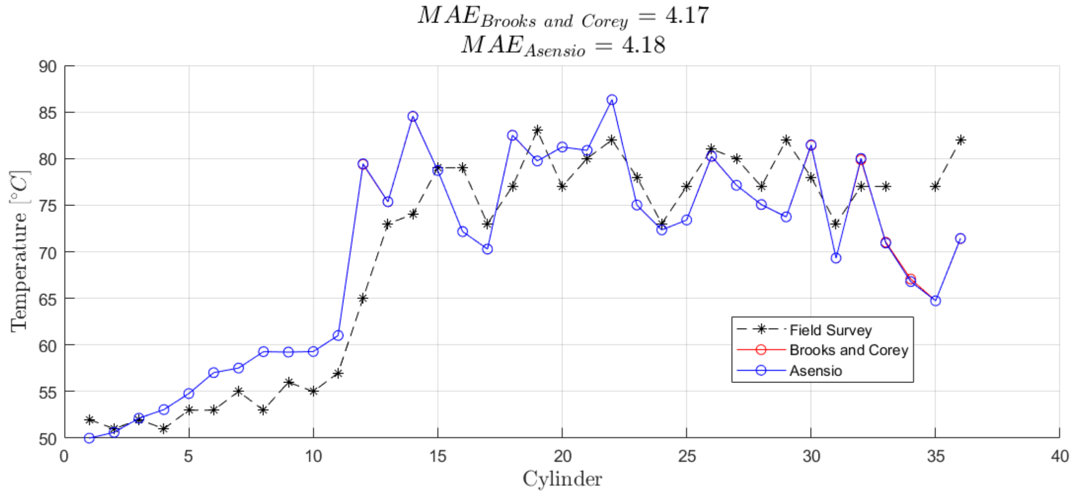

(a) Temperature profile before each cylinder

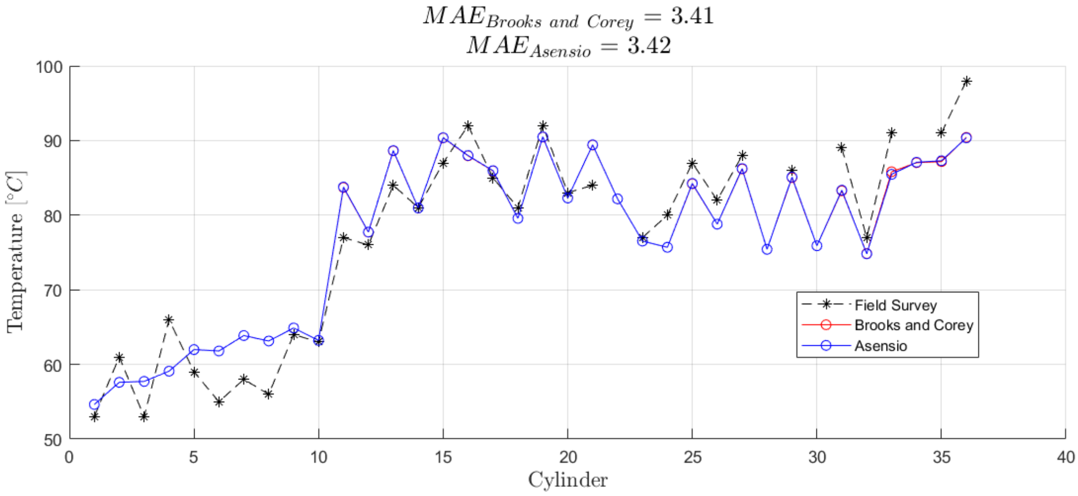

(b) Temperature profile after each cylinder

Figure 9.3: Temperature profiles throughout the pre-dry section for two capillary pressure correlations proposed. (a) shows a temperature profile before each cylinder. (b) shows a temperature profile after each cylinder. The mean average error (MAE) for both correlations is indicated as well.

9.8 The effect of diffusibility

In table (9.4) the effect of different diffusibility correlations is tabulated. Regardless of the FSP, the absolute permeability and the wetting relative permeability, higher moisture contents were calculated using Ramaswamy's correlation. This can be explained by the following reasoning.

Figure 6.5 reports lower diffusibilities for Ramaswamy's correlation, regardless of the volumetric saturation. This means that it becomes harder for the vapour to diffuse through the paper web if Ramaswamy's relation is applied. The evaporated water near the surface cannott easily be transferred into the sheet, reducing the heat pipe effect. This means that less heat and moist is transferred into the sheet, causing larger temperature- and moisture gradients. This can be seen in figure 9.4. Ramaswamy's correlation causes larger temperature- and moisture gradients in the early stage of drying. In a developed drying stage, a difference in average moisture content exists, while larger temperature gradients still exists.

Regardless of the FSP and the absolute permeability, Ramaswamy's correlation reports higher MAEs for both temperature profiles (see figure 9.5). The diffusibility correlation proposed by Hartley and Richards [51] will be used for future calculations, because the calculated final moisture contents for this correlation come closest to measured values. Furthermore, the MAE for both temperature profiles indicate lower values if Hartley and Richards's [51] correlation is applied.

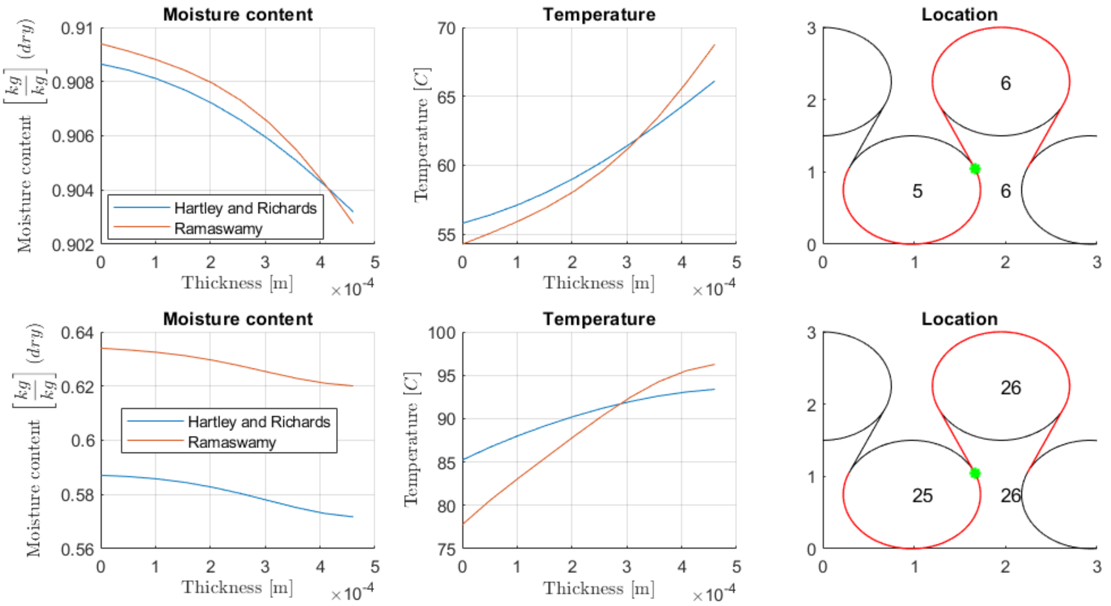

Figure 9.4: Moisture content and temperature in the sheet for different diffusibility correlations at different locations in the predyer section.

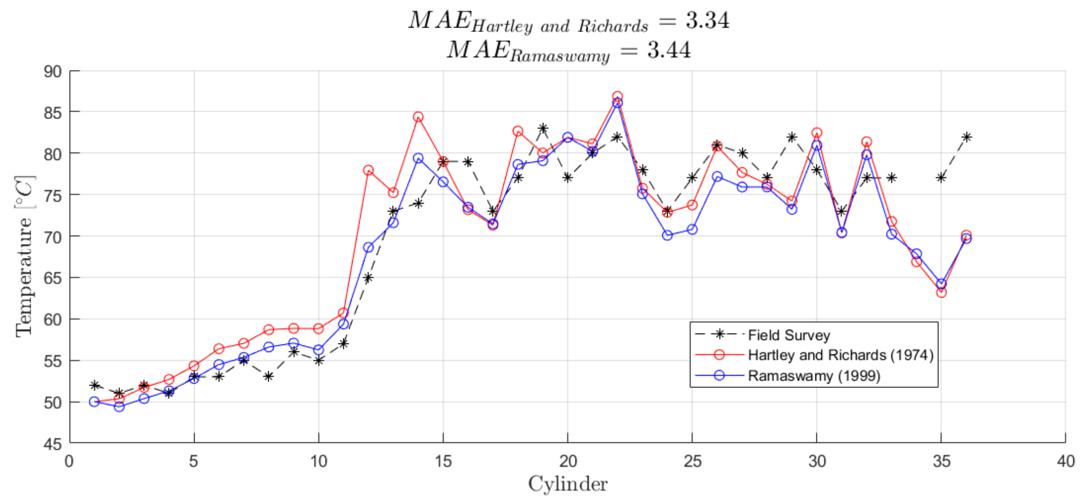

(a) Temperature profile before each cylinder.

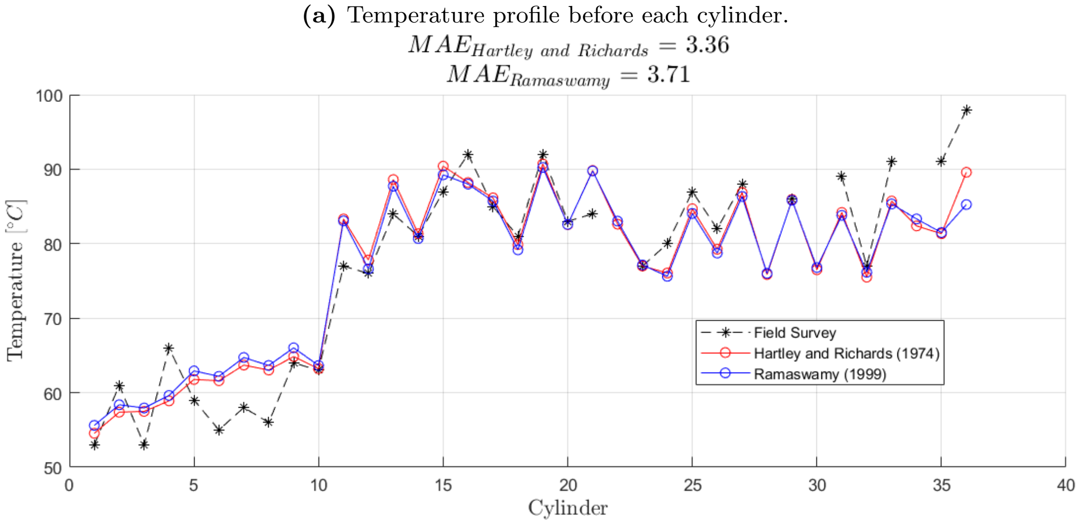

(b) Temperature profile after each cylinder.

Figure 9.5: Temperature profiles for different diffusibility correlations.

9.8.1 Determining the remaining parameters

Remaining partial pressure of air, P_{air}
Varying the remaining partial pressure of air has a negligible influence on the calculated average moisture content. This conclusion is based on the simulation results provided in table 9.5. In these simulations the atmospheric pressure is exceeded 7 to 10% of the total drying time.
However, for the correlations chosen above, the total pressure in the sheet only exceeds atmospheric pressure 1% of the total drying time. Therefore, the value of the remaining partial pressure of air will not affect the drying process and is set to 0.1 $[kPa]$ for future calculations.

Fibre saturation point, M_{FSP}
In table 9.4 it was found that by lowering the FSP, lower final moisture contents could be reached. In order to find the most applicable value, an even lower value of the FSP was explored. The result can be found in table 9.6. More accurate moisture contents and temperature profiles were obtained if the FSP was set to and lower 0.1 $\left[\frac{kg}{kg}\right]$ (dry).
However, a FSP of 0.1 $\left[\frac{kg}{kg}\right]$ (dry) is outside the range reported by Reardon [11] and Luukko [85]. Therefore, it was chosen to select a slighly less accurate value of 0.2 $\left[\frac{kg}{kg}\right]$ (dry) for the FSP.

Absolute permeability, K
In table 9.4 also the effect of varying the absolute permeability is reported. For an increased absolute permeability, lower final moisture contents are achieved. Similar to the FSP, a more extreme value is investigated to see the effect on the final moisture content and temperature profiles. This is shown in table 9.6. Increasing the absolute permeability to 400×10^{-15} $\left[m^2\right]$, results in negligible change in the temperature profiles and final moisture content. Therefore, a value of 300×10^{-15} $\left[m^2\right]$ is used in future calculations.

M_{FSP} $\left[\frac{kg}{kg}\right]$ (dry)	K $\left[m^2\right]$	M_{av} $\left[\frac{kg}{kg}\right]$ (dry)	MAE before	MAE after
0.1	300×10^{-15}	0.2965	3.52	3.37
	400×10^{-15}	0.2959	3.52	3.37
0.2	300×10^{-15}	0.3069	3.99	3.52
	400×10^{-15}	0.3021	3.98	3.51

Table 9.6: Final moisture contents and mean average errors in the temperature profiles for different FSPs and absolute permeabilities.

9.9 Accuracy

In order to finalize the model, its accuracy has to be checked in the spacial and time domain. Furthermore, the sensitivity to the temperature measurement difference (TMD) has to be evaluated.

9.9.1 Accuracy in space

A similar test as described in section 8.3.1 is performed to check the accuracy in the spatial domain. The moisture content at six evenly distributed nodes is evaluated for an increasing number of nodes at an arbitrary location at the end of the pre-dry section. The results are shown in table 9.7. It can be seen that the model is still second order accurate in space. For future calculations eleven nodes were chosen, because this was found to be a good balance between computational time and accuracy.

M_{dry}	Location of point					
	Node 1	Node 2	Node 3	Node 4	Node 5	Node 6
N=6	0.4639	0.4620	0.4567	0.4474	0.4329	0.4114
N=11	0.4648	0.4629	0.4576	0.4482	0.4338	0.4123
N=21	0.4651	0.4632	0.4578	0.4484	0.4340	0.4125
Order	2.03	2.02	2.01	1.99	1.97	1.97

Table 9.7: Calculated moisture content $\left[\frac{kg}{kg}\right]$ (dry) at six thickness points for an increasing number of nodes. Values were calculated at an arbitrary point at the end of the pre-dry section. By applying eq.(107) the order of accuracy in space was calculated.

9.9.2 Accuracy in time

In a similar way, the order of accuracy in the time domain was checked. The calculated moisture contents are reported in table (9.8). It can be seen that the model is not second order accurate in time in the end of the pre-dry section. This is probably caused by time-varying boundary conditions. No further investigation was done, because accurate results were obtained using the time steps investigated. Although the numerical scheme is unconditionally stable, a minimal time step of $0.0005[s]$ was required to ensure convergence in each time step iteration.

M_{dry}	Location of point					
	Node 1	Node 2	Node 3	Node 4	Node 5	Node 6
dt = 0.0005	0.4648	0.4630	0.4576	0.4482	0.4338	0.4123
dt = 0.00025	0.4648	0.4630	0.4576	0.4482	0.4338	0.4123
dt = 0.000125	0.4648	0.4629	0.4576	0.4482	0.4338	0.4123
Order	-0.3795	-0.4049	-0.3902	-0.1994	0.3519	1.5621

Table 9.8: Moisture content $\left[\frac{kg}{kg}\right]$ (dry) at 6 points in the paper web for different time step sizes. Values were calculated at an arbitrary point at the end of the pre-dry section. By applying eq.(108) the order of accuracy in time was calculated.

9.9.3 Temperature measurement distance (TMD)

As mentioned before, the TMD is defined as the distance between the contact point of the paper web with the cylinder and the temperature measurement point. This distance was estimated to be $0.3[m]$. However, this is an estimation and subject to error. Therefore, the effect of this distance should be investigated. Table (9.9) reports the effect of the TMD on the temperature profiles. It can be seen that a TMD of $0.3[m]$ results in the lowest MAE for both temperature profiles.

	TMD $[m]$				
	0.1	0.2	0.3	0.4	0.5
MAE (before)	4.0547	4.0213	3.9858	4.0226	4.0642
MAE (after)	3.8556	3.5173	3.5140	3.6886	3.9467

Table 9.9: The effect of the temperature measurement distance on the mean average error of both temperature profiles.

9.10 Concluding remarks

An overview of the most applicable correlations and values is given in table 9.10. A calculated final moisture content of 0.3079 $\left[\frac{kg}{kg}\right]$ (dry) or 0.2354 $\left[\frac{kg}{kg}\right]$ (wet) was obtained. The measured average moisture content in the field survey was 0.213 $\left[\frac{kg}{kg}\right]$ (wet), meaning that the model overestimates the

calculated wet basis moisture content by 0.0224 $\left[\frac{kg}{kg}\right]$ (wet).
MAE values of 3.98 and 3.51 $[K]$ were calculated for the temperature profiles before and after each cylinder, respectively. Some error in the temperature profiles is allowed, because temperature measurements were performed with a signicant amount of uncertainty.
Kadant Johnson already uses a model that predicts the temperature profile throughout the dryer section. In figure 9.6 the measured- and calculated temperature after each cylinder is depicted. It can be shown that both models are able to track the temperatures relatively well.

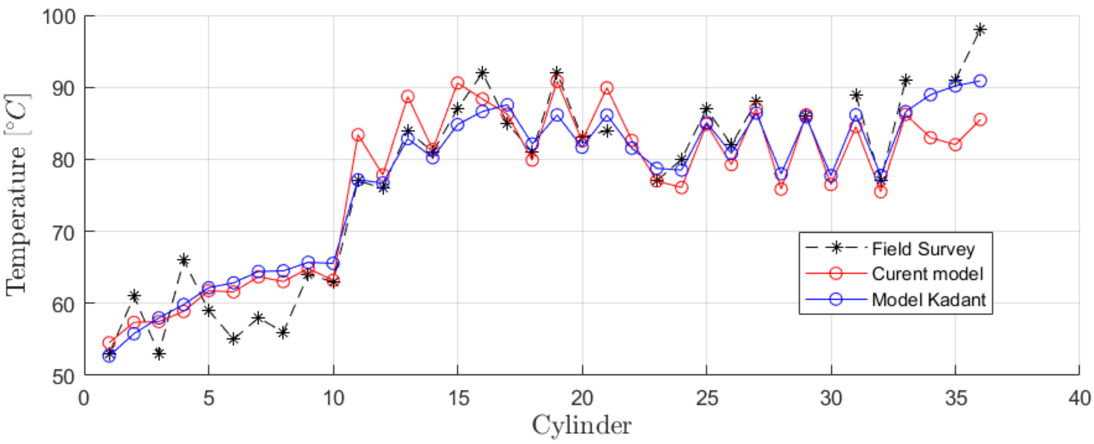

Figure 9.6: Temperature profiles calculated after each cylinder

Having obtained the final model, it is possible to determine the energy consumption per cylinder. This value does not include any losses, but purely states the energy that is transferred from the cylinder to the paper web. The results are given in appendix A.18.

Parameter	Symbol	Correlation / value	
Contact heat transfer coefficient	h_c	Yeo et al. [23]	
Wetting relative permeability	k_{rw}	Brooks and Corey [10]	
Non-wetting relative permeability	k_{rnw}	Brooks and Corey [10]	
Capillary pressure	P_c	Brooks and Corey [10]	
Diffusibility	$\frac{D_{eff}}{D_v}$	Hartley and Richards [51]	
Mass transfer theory	$[-]$	High (eq.(67))	
Absolute permeability	K	300×10^{-15}	$[m^2]$
Fibre saturation point (FSP)	M_{FSP}	0.2	$\left[\frac{kg}{kg}\right]$ (dry)
Remaining partial pressure of air	P_{air}	0.1	$[kPa]$
Temperature measurement distance (TMD)	$[-]$	0.3	$[m]$

Table 9.10: An overview of the different correlations and values used in the final model.

10 Changing operating conditions

At this point, the effect of different operating conditions can be evaluated. As mentioned before, a large number of operating conditions can be altered. However, in this work only three varying operating conditions are evaluated. Firstly, the effect of double-felting the first 10 cylinders will be investigated. Thereafter, the effect of increasing the relative humidity will be checked. The effect of various machine speeds will be considered lastly.

10.1 Felting first 10 cylinders

As mentioned before, the first 10 cylinders were not felted in the dryer section investigated. The reason for not felting these cylinders is unclear, but this has probably to do with the runnability of the dryer section. A certain heating time is required to prevent the fibres from sticking to the hot cylinder wall. Sticky fibres may cause breakage down the dryer section. By adding a felt, the heat transfer is increased enormously, thus causing sticky behaviour.
Normally the heating-up time required is only 1 or 2 cylinders instead of 10. In figure 10.1 the effect of felting the beginning of the pre-dry section is shown. By applying felts, the paper web reaches higher temperatures in the beginning due to a reduced mass transfer and a tremendous increase in contact heat transfer coefficient. After cylinder 10 the temperature profiles almost coincide. By adding the felt, the dry-basis moisture content at the end of the pre-dry section is 0.214 $\left[\frac{kg}{kg}\right]$ (wet). This is an increase of 8.9% compared to current operating conditions (0.2354 $\left[\frac{kg}{kg}\right]$ (wet)). Furthermore, it can be seen that the warm-up time is reduced by 50%, because only five cylinders are required to raise the sheet temperature to constant levels.

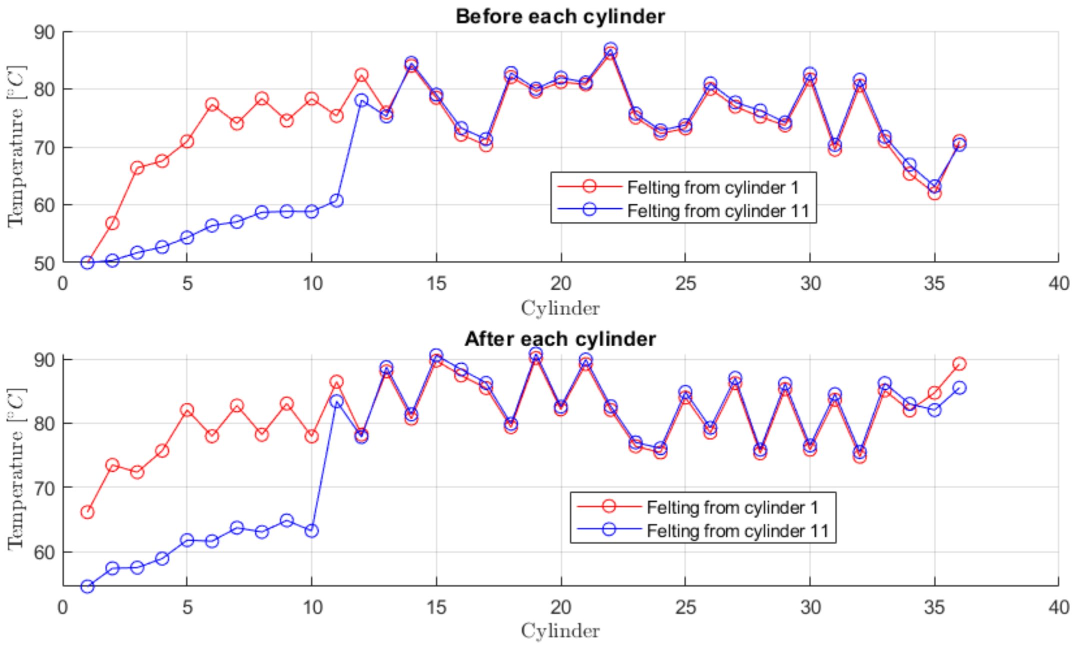

Figure 10.1: The effect of felting the first 10 cylinders on both temperature profiles.

10.2 Fixing the relative humidity

In the field survey, the relative humidities in the pockets vary between 20% and 70%. By keeping the relative humidity at a fixed high level, the overall costs may be reduced. This may be counter intuitive as this reduces the driving force for evaporation. However, a higher relative humidity means that less air is needed to transport the moist away from the paper web. This means that fans can be turned down, reducing the electric consumption and increasing the lifetime of the fans. Furthermore, the energy density of the exhaust air is increased. This is favorable for the heat recovery.

One should be careful when raising the relative humidity too close to unity. At unity the air is fully saturated and the dew point is reached. This means that condensation starts. Condensation in the hood is dangerous, because this may cause dripping on the sheet resulting in uneven drying and runnability issues.
In appendix A.17, a calculation is performed to investigate the effect of using a fixed high relative humidity. It was found that fixing the relative humidity at 80% results in a volumetric flow rate reduction of 60%.
At a relative humidity of 80%, the average wet-basis moisture content calculated was 0.282 $\left[\frac{kg}{kg}\right]$ (wet). Compared to the normal conditions (0.235 $\left[\frac{kg}{kg}\right]$ (wet)), this is an increase by 20%.

The effect of fixing the relative humidity on the temperature profiles is shown in figure 10.2. It can be seen that higher temperatures occur in the drying section. As less moist is evapourated and transported from the web, less heat for evaporation is required. This means that the temperature of the sheet drops to a smaller extent in between the cylinders. This results in a higher overall temperature of the sheet.

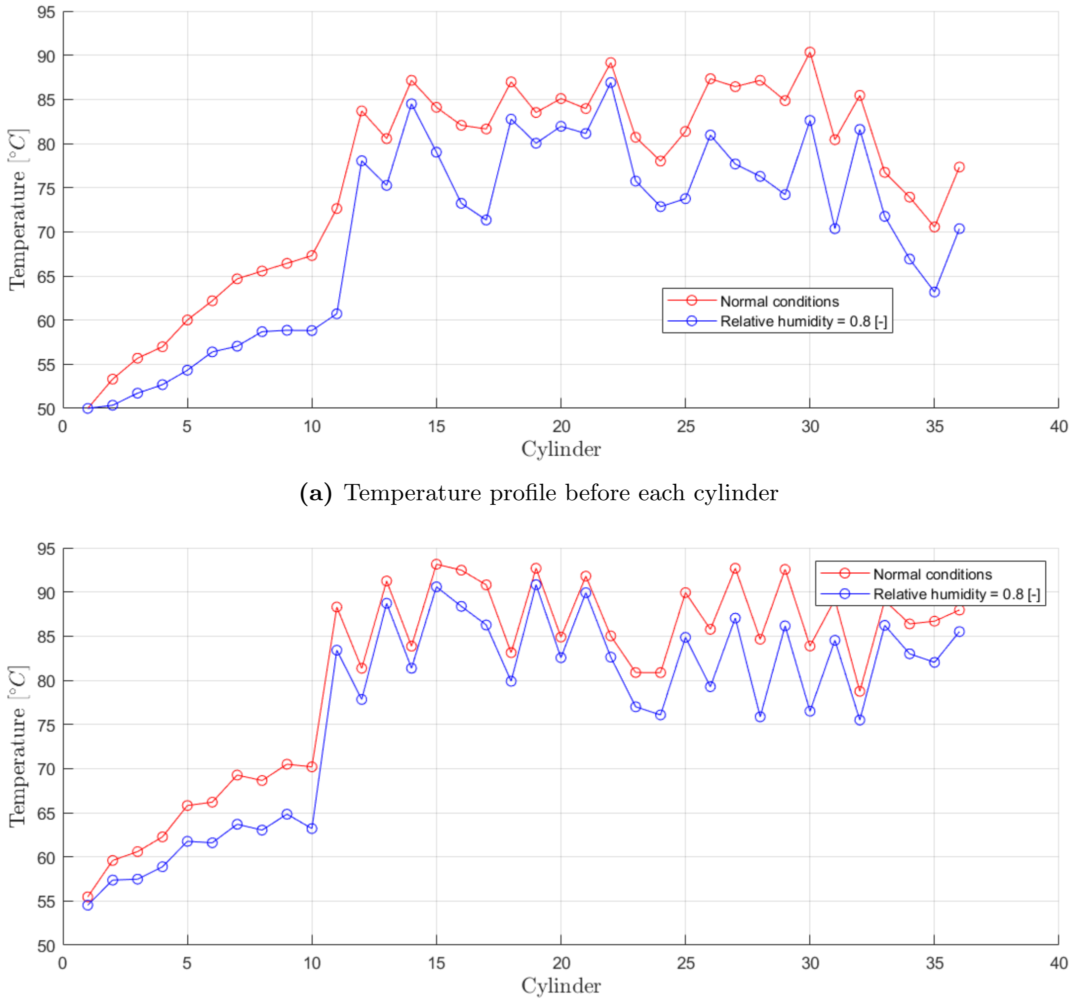

(a) Temperature profile before each cylinder

(b) Temperature profile after each cylinder

Figure 10.2: The effect of fixing the relative humidity of the pockets at 0.8 for both temperature profiles.

10.3 Varying the machine speed

From table 10.1 it can be seen that for increasing machine speeds, the average moisture content at the end of the pre-dry section increases. By increasing the machine speed, the drying time is reduced. This means that the total evapourating- and heating time is reduced. Therefore, less water is removed from the paper web.

Figure 10.3a shows the corresponding temperature profiles. It can be seen that lower temperatures are reported for increased machine speeds.

Machine speed [%]	Moisture content $\left[\frac{kg}{kg}\right]$ (wet)
90	0.2223
95	0.2294
100	0.2354
105	0.2421
110	0.2501

Table 10.1: Calculated average moisture content at the end of the pre-dry section for various machine speeds

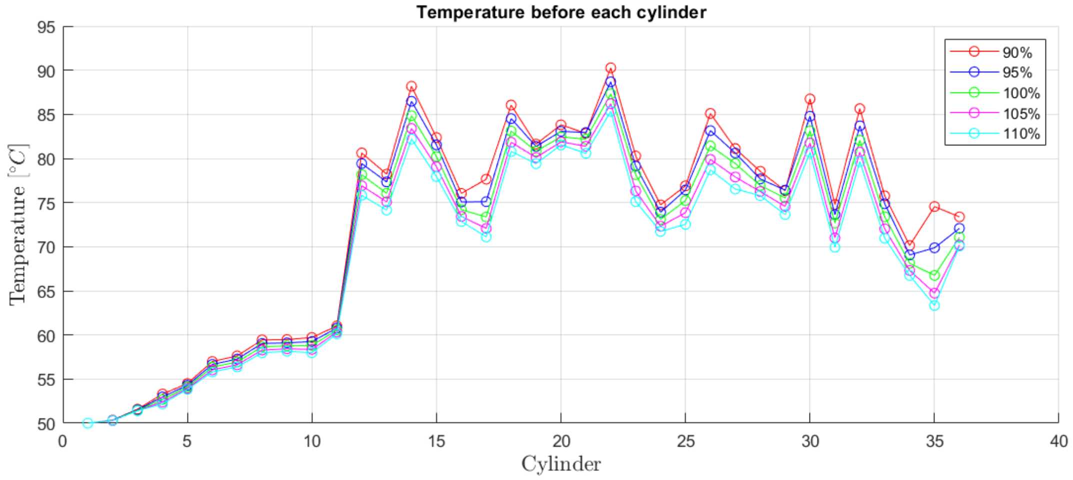

(a) Temperature profiles measured before each cylinder for various machine speeds.

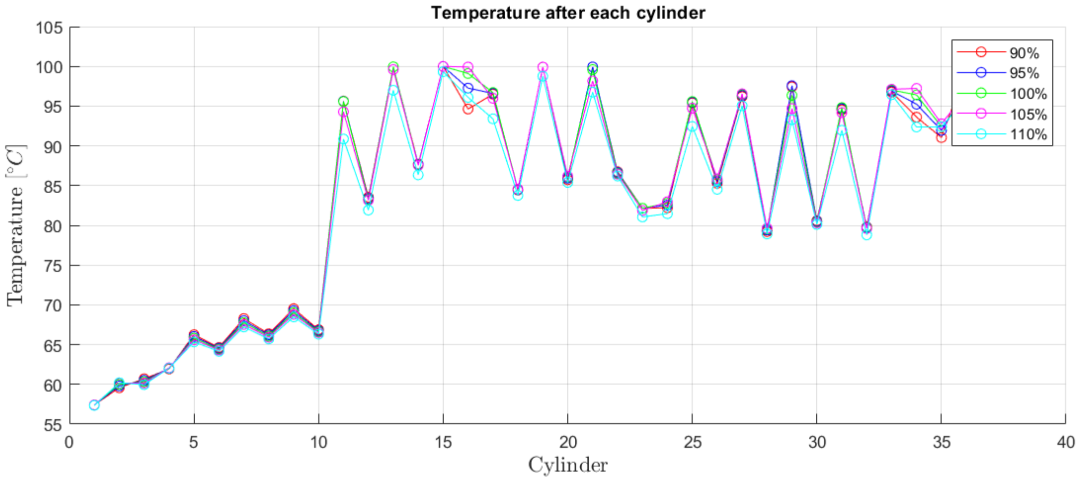

(b) Temperature profiles measured after each cylinder for various machine speeds.

Figure 10.3: Calculated and measured temperatures before (10.3a) and after (10.3b) each cylinder.

10.4 Concluding remarks

The effect of varying three operating conditions is investigated in this section. Adding a felt to the first 10 cylinders reduces the wet basis moisture content by 8.9%. However, this may result in fibres sticking to the cylinders, causing runnability problems.

By fixing the relative humidity at 80% it was found that the wet basis moisture content of the paper web increased by 20%. However, the volumetric flow rate through the fans could decrease by 60%. Therefore, a cost analysis should be done comparing the reduction of the fans costs (electric consumption, depreciation, maintenance, etc.) to the required additional investment costs.
The same reasoning applies to increased machine speeds. If an increase in machine speed is desired, one should compare the additional income to the required additional investment costs to meet the required dryness. Such cost analyses are omitted in this work, because these are outside the scope of this project.

11 Conclusions

The aim of this study was to develop, test and validate a one-dimensional model that captures all essential internal- and external transfer phenomena occurring in the paper web during multi-cylinder drying. The moisture content and the temperature were calculated in the thickness direction of the sheet, by relating the initial conditions, sheet properties, drying conditions and dryer section configuration. In this model five species were considered: free water, bound water, water vapour, air and fibres. Only water vapour and free water were considered to contribute to the mass transfer. The ultimate goal of this work is to see the effect of changing operating conditions on the dryer performance. This work consists of six parts. In the first part, a detailed description of the paper drying process is given. In the second part, a mathematical model is developed to describe the different heat- and mass transfer phenomena occurring in the sheet. The third part covers the thermodynamic properties and correlations used to complete the transfer equations. Analysing the results of the field survey performed is described in part four. In the fifth part, the model is validated against data from the field survey. The last part describes the effect of changing three operating conditions on the moisture content and temperature in the sheet.

Description of the drying process
Firstly, an overall summary of the drying process was given. In this summary, the cylinders, ventilation, steam and condensate systems and heat recovery were described. Subsequently, the definitions and fundamentals used in this paper were treated.

Model development
Mass and heat transfer equations were developed by applying conservation equations for mass and heat. Capillary forces accounted for free water transport, while water vapour was transported through diffusion and a possible pressure gradient. This pressure gradient occurs when the total pressures rises above atmospheric. Two sets of time-varying boundary conditions were proposed, to simulate the external conditions. Furthermore, both low- and high mass transfer theory were used to describe evaporation from the web. By applying time-varying boundary- and initial conditions, a dryer section was created. The model was discretized by central-differencing in space and using the Crank-Nicolson method for the time integration. This resulted in a second order accurate scheme in space and time. Both two- and three-tier configurations with unfelted and double-felted cylinders are incorporated in the model, making it extensive and suitable for other dryer section configurations.

Sheet properties and thermodynamic relations
All sheet properties and thermodynamic relations were obtained through studying the literature. The effect of the hygroscopic region was fully accounted for. Sorption isotherms and heat of sorption curves were used to describe the sorptive effect on the vapour partial pressure and the heat of evaporation. The fibre saturation point was assumed to be the onset of the hygroscopic region. It was assumed that this point marks the point beyond which capillary flow ceases. Furthermore, the change of web structure was accounted for in the hygroscopic region by means of shrinkage and changing porosity. Relations for the effective diffusivity, thermal conductivity, specific heat capacitiy, density, diffusibility, absolute permeability and relative peremability were found in the literature.

Field survey
An extensive field survey was performed on the dryer section of a Dutch board producing paper machine. The temperature of each pocket and cylinder was measured, providing excellent input data for time-varying boundary conditions. Furthermore, sheet temperatures were measured in order to validate the calculated sheet temperatures and to check the warm-up time of the paper web. The measured warm-up time was around 10 cylinders.
By applying mass balances on each dryer section, the moisture content before and after each subsection was determined. The heat balance computed was of little use, due to the lack of data. Due to the large temperature difference between the steam and outer cylinder wall, it was found that cylinder 23 was malfunctioning and probably in flooded state. Only data from the pre-dry section were used to

validate the model. Based on data from the field survey, the final wet-basis moisture content at the end of the pre-dry section was calculated to be 0.271 $\left[\frac{kg}{kg}\right]$ (dry) or 0.213 $\left[\frac{kg}{kg}\right]$ (wet).

Parameter selection
In order to validate the model, boundary conditions proposed by Reardon [11] and Nasrallah [16] were investigated first. Both sets of boundary conditions were subject to one-sided cylinder heating. Reardon's [11] set of boundary conditions showed diverging and contradicting behaviour, while Nasrallah's [16] set of boundary conditions converged with second order accuracy.
A sensivity analysis was carried out in order to evaluate the suitability of the different parameters found in the literature. Due to missing information, the parameters were only tested against measurements performed in the pre-dry section. The final average moisture content at the end of the pre-dry section was used as test criterion in combination with the mean average error (MAE) of two sheet temperature profiles. One sheet temperature profile indicates the temperatures before each cylinder and the other indicates the temperatures after each cylinder. By comparing the calculated values with data from the field survey, the two MAEs were calculated.
In the analysis, several correlations for the contact heat transfer coefficient, the wetting relative permeability, the non-wetting relative permeability, capillary pressure and diffusibility were investigated. Furthermore, the most applicable values for the absolute permeability, FSP and remaining partial pressure of air were examined. The analysis resulted in the following findings:

- The wetting relative permeability correlation proposed by Robertson [75] grossly overestimates the final moisture content. The diminishing effect of the capillary flow at high saturation is the cause of this.

- The effect of changing the non-wetting relative permeability correlation resulted in negligible differences. This could be explained by the limited amount of time the total pressure in the sheet exceeded atmospheric (only 2%).

- The capillary pressure correlations evaluated showed a negligible effect on the final moisture content and sheet temperatures.

- The diffusibility correlation proposed by Hartley and Richards [51] resulted in lower calculated average moisture contents. The correlation ensured the sides of the web to remain moist for a longer period of time, enhancing the mass transfer from the web.

- Yeo et al.'s [23] correlation for the contact heat transfer coefficient results in moisture contents closest to the measured values. Furthermore, the temperature profiles were described with sufficient accuracy.

- The convective component in the evaporation process could not be neglected. Therefore, high mass transfer theory should be used for further modeling.

- The FSP and the absolute permeability significantly influenced the drying performance. 0.1 $\left[\frac{kg}{kg}\right]$ (dry) and 300×10^{-15} $\left[m^2\right]$ were the most applicable values for the FSP and the absolute permeability, respectively.

- A temperature measurement distance of $0.3[m]$ gave the smallest mean average error compared to measured temperatures. This distance is measured between the contact point of the paper web with the cylinder and the point of the sheet temperature measurement.

A time step of 0.5 $[ms]$ and and 11 nodes were chosen for future calculations. For the final model, an average wet-basis moisture content of 0.2354 $\left[\frac{kg}{kg}\right]$ (wet) was obtained, overestimating the measured wet basis moisture content by 0.0224. $\left[\frac{kg}{kg}\right](wet)$. The MAEs for sheet temperatures measured before and after each cylinder were 3.98 and $3.51[K]$, respectively.

Changing operating conditions
Three operating conditions were changed to evaluate the effect on the moisture content and temperature.

- Felting of the first ten cylinders was considered first. A reduction of 9% in the final wet-basis moisture content could be achieved. This would reduce the warm-up time by 50%.

- Secondly, the relative humidity of the pockets was fixed at 80%. This results in an increase by 20% in the final moisture content. However, a reduction by 60% in volumetric flow rate through the fans could be achieved, reducing the operational costs.

- Lastly, the effect of varying the machine speed was investigated. By increasing the machine speed, the final moisture content was increased, due to less evapourating time and less heat input. The input of less heat is supported by lower calculated sheet temperatures for increased machine speeds.

12 Recommendations for future work

1. By incorporating a separate mass balance for air, the total pressure in the sheet can be estimated more closely. This will give a better insight in the convective flow contributions. Furthermore, this will contribute to a better accuracy of the model.

2. Account for movement of bound water. In this study this movement was not taken into account. Taking this into account will give more accurate results, especially when the moisture content in the sheet enters the hygroscopic region.

3. Incorporate other cylinder and felt configurations in the model. This generalizes the model, making it applicable to more dryer sections. The priority should be on single-felted configurations as this is the most common type of felting in modern dryers that is not included in the model.

4. Investigate the change in paper- and transport properties in case additives are added to the sheet. This is important to fully understand what happens when sizing- and coating solutions are added. This may help to optimize the design of the speedsizers and coaters and this will contribute to the accurate modeling of a complete dryer section, including speedsizers and coaters.

5. Investigate other types of drying. Over the years impingement drying and through drying have proven to be reliable and efficient drying technologies. Investigating the transport phenomena occuring when implementing these technologies may give insight into new developments.

6. Investigate the effect of different furnish types on the thermodynamic properties more precisely. At this point, too little furnish types have been investigated, making it hard to determine which thermodynamic properties apply best to this case. Furthermore, there is a lack of standardization in furnish type measurements, making it hard to compare different correlations and properties.

7. Perform more elaborate surveys on different furnish types at different drying temperatures. In this work only one dryer section is used for validation, leaving it vulnerable to error. By extending the validation to several dryer sections, the model is more generally applicable.

8. The effect of changing paper properties during drying could be examined more closely. Several paper properties were examined at bone-dry conditions, while paper may face significant changes upon drying.

9. Investigate the effect of changing more operating conditions. In this project only the effect of changing three conditions was investigated.

10. Include the heat transfer from the steam through the cylinder in the model. In this way, the effect of changing steam temperatures could be modeled. Furthermore, the effect of changing cylinder properties and conditions could be captured. These properties and conditions include the thermal conductivity and thickness of the cylinder wall and the behaviour and thickness of the condensate layer inside the cylinder.

11. An optimal operating point could be investigated. This requires performing a cost analysis in order to define a reasonable business case.

References

[1] M. C. Asensio, *Transport phenomena during drying of deformable, hygroscopic porous media: Fundamentals and applications.* PhD thesis, Texas A & M University, 2000.

[2] A. K. Ghosh, "Fundamentals of paper drying-theory and application from industrial perspective, evaporation, condensation and heat transfer," pp. 535–582, 1988.

[3] K. Roonprasang, "Thermal analysis of multi-cylinder drying section with variant geometry," 2008.

[4] O. Polat and A. Mujumdar, "Drying of pulp and paper," *Handbook of industrial drying, Third Edition*, no. November, 2006.

[5] M. Karlsson, *Papermaking Part 2, Drying.* Helsinki: Fapet Oy, 2000.

[6] L. Sivill and P. Ahtila, "Energy efficiency improvement of dryer section heat recovery systems in paper machines – a case study," *Applied Thermal Engineering*, vol. 29, pp. 3663–3668, 2009.

[7] M. Bernardes, "Convective heat transfer analysis of solar chimney power plant collectors," 2013.

[8] M. Sophocleous, "Understanding and explaining surface tension and capillarity: An introduction to fundamental physics for water professionals," *Hydrogeology Journal*, vol. 18, pp. 811–821, 2010.

[9] A. Kharaghani, *Drying and wetting of capillary porous materials: Insights from imaging and pysics-based modeling.* PhD thesis, Otto-von-Guericke-Univerität, 2020.

[10] R. H. Brooks and A. Corey, "Properties of porous media affecting fluid flow," *Journal of the irrigation and drainage division*, vol. 92, pp. 61–88, 1966.

[11] S. Reardon, "a Mathematical Model for the Simulation of Paper Drying Energy Consumption," no. November 1994, p. 279, 1994.

[12] Z. Alothman, "A review: Fundamental aspects of silicate mesoporous materials," *Materials*, vol. 5, pp. 2874–2902, 2012.

[13] J. Prahl, "Thermodynamics of paper fiber and water mixtures phd thesis harvard university cambridge," 1968.

[14] P. Heikkila, "A study on the drying process of pigment coated paper webs," *Drying Technology*, vol. 14, no. 3-4, pp. 945–946, 1996.

[15] M. Karlsson and M. Soininen, "The influence of hygroscopic properties of paper on the transient phenomena during contact drying of paper webs," in *International drying symposium. 3*, pp. 494–503, 1982.

[16] S. Ben Nasrallah and P. Perré, "Detailed study of a model of heat and mass transfer during convective drying of porous media," *International Journal of Heat and Mass Transfer*, vol. 31, no. 5, pp. 957–967, 1988.

[17] J. J. T.Tuovinen and P. Becker, "Simulation of sloshing of condensate water inside a drying cylinder using particle finite element mehtod," in *Advances in pulp and paper research*, (Oxford), pp. 383–407, 2017.

[18] Kadant Johnson, "Drive power and torque in paper machine dryers." `https://www.slideshare.net/kadant/drive-power-and-torque-in-paper-machine-dryers`, 2020.

[19] The Nippon Joint, "Cantilever stationary syphonsTitle." `https://www.nippon-joint.co.jp/product/e-cantilever.html`, 2020.

[20] GmbH Dampf Kondensat und Maschinensysteme, "Heating systems." `http://www.dkum.de/Englisch/system.htm`, 2015.

[21] Spirax Sarco, "Steam jet thermocompressor." `https://www.hvacwebconnection.com/Products/steam_jet_thermocompressors.htm`, 2018.

[22] M. Sadeghi, *Modeling and simulation of transport phenomena in paper drying.* PhD thesis, McGill University, Montreal, 2003.

[23] Y. K. Yeo, K. S. Hwang, S. C. Yi, and H. Kang, "Modeling of the drying process in paper plants," *Korean Journal of Chemical Engineering*, vol. 21, no. 4, pp. 761–766, 2004.

[24] S. Ramaswamy and R. A. Holm, "Analysis of heat and mass transfer during drying of paper/board," *Drying Technology*, vol. 17, no. 1-2, pp. 50–72, 1999.

[25] J. Laurijssen, A. Faaij, and E. Worrell, "Benchmarking energy use in the paper industry: A benchmarking study on process unit level," *Energy Efficiency*, vol. 6, no. 1, pp. 49–63, 2013.

[26] T. Xu, J. Sathaye, and K. Kramer, "Sustainability options in pulp and paper making: Costs of conserved energy and carbon reduction in the US," *Sustainable cities and society*, vol. 8, pp. 56–62, 2013.

[27] P. Gielen, Dolf & Bennaceur, Kamel & Kerr, Tom & Tam, Cecilia & Tanaka, Kanako & Taylor, Michael & Taylor, *Tracking industrial energy efficiency and CO2 emissions.* No. January, IEA, 2007.

[28] "Energy efficiency and CO2 reduction in the pulp and paper industry," tech. rep., European Commission, 2012.

[29] European Commission, "Communication from the Energy Roadmap 2050," in *Commission to the European Parliament, the council, the European economic and social committee and the committee of the regions*, (Brussels, Belgium), 2011.

[30] L. Szabó, A. Soria, J. Forsström, J. T. Keränen, and E. Hytönen, "A world model of the pulp and paper industry: Demand, energy consumption and emission scenarios to 2030," *Environmental Science and Policy*, vol. 12, no. 3, pp. 257–269, 2009.

[31] K. Edelmann, S. Kaijaluoto, O. Timofeev, T. Saarenko, H. Kiiskinen, and M. Karlsson, "The impact of new paper drying technologies on energy consumption," 1996.

[32] A. S. Mujumdar, *Handbook of industrial drying.* CRC Press, fourth edi ed., 2014.

[33] S. Stenström, "Drying of paper: A review 2000–2018," *Drying technology*, vol. 38, no. 7, pp. 825–845, 2020.

[34] S. Ghodbanan, R. Alizadeh, and S. Shafiei, "Thermodynamic and heat transfer evaluation of pocket drying section in the multi-cylinder dryers of paper machine," vol. 13, no. 2, pp. 57–70, 2016.

[35] A. Gubkov, N. Fermor, and N. Smirnov, "Vapor pressure of mono-poly systems," *Zh. Prikl. Khim*, vol. 37, pp. 2204–2210, 1964.

[36] O. Bridgeman and E. Aldrich, "Vapor pressure tables for water," 1964.

[37] G. Hundy, A. Trott, and T. Welch, *Refrigeration, air conditioning and heat pums.* Butterworth_Heinemann, fourth edi ed., 2016.

[38] R. H. Perry and D. W. Green, *Perry's chemical engineers' handbook.* McGraw-Hill, eight edit ed., 2008.

[39] Y. O. Devres, "Psychrometric properties of humid air: Calculation procedures," *Applied Energy*, vol. 48, no. 1, pp. 1–18, 1994.

[40] A. F. Mills, *Basic heat and mass transfer.* Pearson, second ed., 2014.

[41] S. Whitaker, "Forced convection heat transfer correlations for flow in pipes, past flat plates, single cylinder, single spheres, and for flow in packed beds and tube bundles," *AIChE Journal*, vol. 18, pp. 361–371, 1972.

[42] Sherwood, Pigford, and Wilke, *Mass Transfer*. McGraw-Hill, 1975.

[43] S. Park, R. A. Venditti, H. Jameel, and J. J. Pawlak, "Changes in pore size distribution during the drying of cellulose fibers as measured by differential scanning calorimetry," *Carbohydrate polymers*, vol. 66, no. 1, pp. 97–103, 2006.

[44] E. W. Comings, "Contributions of T.K.Sherwood and associates to the field of drying," *Drying Technology*, vol. 1, no. 2, pp. 249–273, 1983.

[45] A. Belhamri, "Characterization of the first falling rate period during drying of a porous material," *Drying Technology*, vol. 21, no. 7, pp. 1235–1252, 2003.

[46] A. Nissan and W. Kaye, "An analytical approach to the problem of drying of thin fibrous sheets on multicylinder machines," *Tappi Journal*, vol. 38, no. 7, pp. 385–398, 1955.

[47] A. Nissan and W. Kaye, "Mechanism of drying of thick porous bodies during the falling-rate period," *Nature*, vol. 180, no. 4577, pp. 142–143, 1957.

[48] A. Nissan, W. Kaye, and J. Bell, "Mechanism of drying thick porous bodies during the falling rate period: The pseudo-wet-bulb temperature," *AIChE Journal*, vol. 5, no. 1, pp. 103–110, 1959.

[49] J. A. Depoy, "Analog computer simulation of paper drying a workable model," *Pulp and Paper Magazine of Canada*, vol. 73, pp. 67–75, 1972.

[50] S. Han, "Drying of paper," *Tappi*, vol. 53, no. 6, p. 1034, 1970.

[51] F. Hartley and R. Richards, "Hot surface drying of paper, the development of a diffusion model," *Tappi journal*, vol. 57, no. 3, pp. 157–160, 1974.

[52] P. Lee, L. PF, and H. JA, "Optimizing dryer performance: Modeling heat and mass transfer within a moist sheet of paper or board," 1981.

[53] H. Ma, *Modelling of the drying section of a continuous paper machine: a thesis presented in partial fulfilment of the requirement for the degree of Master in Production Technology at Massey University*. PhD thesis, Massey University, 1996.

[54] J. A. Hinds and A. N. Neogi, "The dynamic computer simulation of a paper machine dryer," *Tappi*, vol. 66, no. 6, pp. 79–82, 1983.

[55] M. Karlsson and J. Paltakari, "A simulation model for paper machine dryer section," in *Drying'92—Proceedings of the eight international drying symposium*, vol. 2, pp. 913–923, 1992.

[56] M. Harrmann and S. Schulz, "Convective drying of paper calculated with a new model of the paper structure," *Drying technology*, vol. 8, no. 4, pp. 667–703, 1990.

[57] B. Wilhelmsson, *An experimental and theoretical study of multi-cylinder paper drying*. PhD thesis, Lund University, Sweden, 1996.

[58] J. Bond, V. Gomes, and W. M. DOUGLAS, "Computer simulation of drying paper by multiple techniques: Can compare performance of your equipment to industry standards," *Pulp & paper Canada*, vol. 97, no. 12, pp. 110–112, 1996.

[59] S. Sidwall, "Comparative structures for simulation of paper drying," in *TAPPI Engineering/Process and Product Quality Conference & Trade Fair, TAPPI Proceedings, 1999*, 1999.

[60] S. Sidwall, J.-F. Bond, and W. Douglas, "Industrial validation of a multiple technique paper drying simulator," in *Process and Product Quality Conference and Trade Fair*, vol. 1, pp. 271–302, 1999.

[61] M. Karlsson and S. Stenström, "Static and dynamic modeling of cardboard drying part 1: Theoretical model," *Drying Technology*, vol. 23, no. 1-2, pp. 143–163, 2005.

[62] M. Karlsson and S. Stenström, "Static and dynamic modeling of cardboard drying part 2: Simulations and experimental results," *Drying Technology*, vol. 23, no. 1-2, pp. 165–186, 2005.

[63] S. A. Reardon, M. R. Davis, and P. E. Doe, "Summaries of peer reviewed papers - computational modeling of paper drying machines," *Tappi Journal*, vol. 83, no. 9, pp. 58–58, 2000.

[64] G. Spolek and O. A. Plumb, "Capillary pressure in softwoods," *Wood Science and Technology*, vol. 15, pp. 189–199, 1981.

[65] M. Lampinen and K. Toivonen, "Application of a thermodynamic theory to determine capillary pressure and other fundamental material properties affecting the drying process," *Drying*, vol. 84, p. 228, 1984.

[66] F. A. Dullien, *Porous media: Fluid transport and pore structure.* Academic press, 2012.

[67] J. Kozeny, "Uber kapillare leitung der wasser in boden," *Royal Academy of Science, Vienna, Proc. Class I*, vol. 136, pp. 271–306, 1927.

[68] P. C. Carman, "Fluid flow through granular beds," *Trans. Inst. Chem. Eng.*, vol. 15, pp. 150–166, 1937.

[69] P. Kassenbeck, "Bilateral structure of cotton fibers as revealed by enzymatic degradation," *Textile Research Journal*, vol. 40, no. 4, pp. 330–334, 1970.

[70] L. Nilsson, "Some studies of the transport coefficients of pulp and paper," 1996.

[71] J. D. Lindsay and P. Brady, "Studies of anisotropic permeability with applications to water removal in fibrous webs part 2: Relationship between water removal and permeability, and additional factors affecting permeability," 1993.

[72] O. Polat, R. Crotogino, A. P. VAN HEININGEN, and W. M. DOUGLAS, "Permeability and specific surface of paper," *Journal of pulp and paper science*, vol. 19, no. 4, pp. J137–J142, 1993.

[73] J. Asensio, MC and Seyed-Yagoobi, "Simulation of paper-drying systems with incorporation of an experimental drum/paper thermal contact conductance relationship," *Journal of Energy resources technology*, vol. 115, no. 4, pp. 291–300, 1993.

[74] S. Norouzi Apourvari and C. H. Arns, "Image-based relative permeability upscaling from the pore scale," *Advances in Water Resources*, vol. 95, pp. 161–175, 2016.

[75] A. Robertson, "The physical properties of wet webs. part 1. fiber-water association and wet-web behavior," *Tappi J*, vol. 42, no. 12, pp. 969–978, 1959.

[76] A. S. Hashemi, "Through drying of machine formed paper and drying nonuniformity.," 2003.

[77] W. Boynton and W. Brattain, "Interdiffusion of gases and vapors," *International Critical Tables*, vol. 5, pp. 62–63, 1929.

[78] W. J. Massman, "A review of the molecular diffusivities of h2o, co2, ch4, co, o3, so2, nh3, n2o, no, and no2 in air, o2 and n2 near stp," *Atmospheric Environment*, vol. 32, no. 6, pp. 1111–1127, 1998.

[79] R. Schirmer, *Die Diffusionszahl von Wasserdampf-Luft-Gemischen und die Verdampfungsgeschwindigkeit.* PhD thesis, 1938.

[80] E. Wintergerst, "Determination of the diffusion coefficient of ammonia referred to air," *Annalen der Physik*, vol. 4, pp. 323–351, 1930.

[81] F. P. Incropera, D. Dewitt, T. Bergman, and A. Lavine, *Fundamentals of heat and mass transfer*. Indiana: John Wiley and Sons, sixth edit ed., 2006.

[82] M. Kobari, Y. Shimizu, M. Endo, and H. Inazuml, "Contact drying of fibrous sheet material," *Industrial and engineering chemistry process design and development*, vol. 24, no. 1, pp. 188–194, 1985.

[83] C. J. Nederveen and J. G. Finken, "Thermal conductivity measurements on wet paper samples at high temperatures," *Drying Technology*, vol. 10, no. 1, pp. 189–198, 1992.

[84] S. Palosaari and H. Nordén, "Heat transfer in porous media with various moisture contents," *Kemian Teollisuus*, vol. 22, no. 5, pp. 359–364, 1965.

[85] K. Luukko and T. C. Maloney, "Swelling of mechanical pulp fines," *Cellulose*, vol. 6, no. 2, pp. 123–136, 1999.

[86] T. Wahlström, "Influence of shrinkage and stretch during drying on paper properties," vol. 31, no. 5, 1999.

[87] A. Lemaitre, C. Foulard, and M. Perron, "Modelling and parameter estimation of paper machine drying sections," *IFAC Proceedings Volumes*, vol. 10, no. 16, pp. 357–365, 1977.

[88] D. Rhodius and L. Gottsching, "Paper and board drying process and its dependence upon drying and paper technological parameters. 4. drying in the multi-cylinder dryer section.," *Papier*, vol. 33, no. 1, pp. 1–9, 1979.

[89] B. Wilhelmsson and S. Stenström, "Heat and mass transfer coefficients in computer simulation of paper drying," *Drying Technology*, vol. 13, no. 4, pp. 959–975, 1995.

[90] Tappi, "TIP 0404-04 Recommended tensions in dryer fabrics," *Tappi*, no. 014, pp. 4–5, 2002.

[91] E. Amar, D. Chaussy, and M. Rueff, "A study of the influence of dryer fabrics upon paper drying: Analysis of contact area and contact coefficient variations with fabric tension," *Appita: Technology, Innovation, Manufacturing, Environment*, vol. 57, no. 6, p. 455–459, 2004.

[92] S. Ghodbanan, R. Alizadeh, and S. Shafiei, "Steady-state modeling of multi-cylinder dryers in a corrugating paper machine," *Drying Technology*, vol. 33, no. 12, pp. 1474–1490, 2015.

[93] G. L. Wedel, *Spoiler bars*. Atlanta: TAPPI Press, 1986.

[94] N. Saad, A. S. Mujumdar, and W. Douglas, "Heat transfer under multiple turbulent slot jets impinging on a flat plate," *Drying technology*, vol. 1, p. 422, 1980.

[95] H. K. Corte and E. Lloyd, "Fluid flow through paper and sheet structure," in *Trans. of the IIIrd Fund. Res. Symp.*, (Cambridge), 1965.

[96] C. T. Dodson and W. W. Sampson, "Modeling a class of stochastic porous media," *Applied Mathematics Letters*, vol. 10, no. 2, pp. 87–89, 1997.

A Appendix

A.1 Additional information on dryer cylinders

A.1.1 Behaviour of the condensate

The behaviour of the condensate depends on various parameters, such as the machine speed, cylinder diameter, amount of condensate and smoothness of the inner side of the cylinder wall. In figure A.1.1 the different conditions occurring at different machine speeds are presented. At low machine speeds there exists only a puddle on the bottom of the cylinder. The mixing is low, but most of the cylinder wall is free of condensate allowing for a good heat transfer. As the speed increases, the puddle goes into

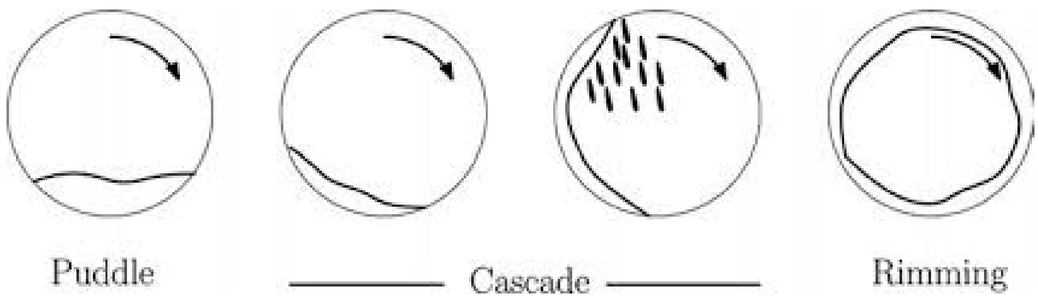

Figure A.1.1: Condensate behaviour for increasing rotational speeds. [17]

cascading conditions. Karlsson [5] reports a transitional speed of 2.5 $\left[\frac{m}{s}\right]$. In the cascading condition, the water is carried up the cylinder wall partly due to centrifugal and viscous forces. Depending on the rotation speed, the condensate falls down at a certain height as the gravitational force still outweighs the centrifugal one.
As speeds increase even further, the centrifugal forces become dominant causing the condensate to go in rimming condition. In this condition, a thin layer of condensate is formed on the cylinder wall. This condensate layer is dynamic, because gravitational input makes the ring sloshing back and forth over the wall. This sloshing causes turbulence in the condensate ring boosting the heat transfer [5]. As rotational speeds increase even further the gravitational influence will reduce. This reduces the sloshing effect and, thus, reduces the heat transfer.

A.1.2 Driving power

Together with the dimension of the cylinder and the amount of condensate in the cylinder, the condensate behaviour strongly influences the driving power required to rotate the cylinder. Figure(A.1.2a) and (A.1.2b) show the driving power required for different dryer speeds for various amounts of condensate. At low speeds, the condensate is puddling and only a small amount of driving power is required. As rotational speeds increase, cascading features start to occur and the driving power required increases rapidly. As the rotational speed increases further, it carries more water along the cylinder wall. Gravity forms an opposing force, causing an increase in driving power. At this point, the combined centrifugal and viscous forces are not strong enough to loop the condensate film. At a certain height, the condensate falls down, losing the angular momentum. When the viscous and centrifugal forces are strong enough to loop the film (rimming condition), the angular momentum is preserved. This explains the sudden drop in required driving power. Further increasing the dryer speeds causes a gradual increase in drying power.

A.1.3 Siphons

The function of a siphon is to transport the formed condensate out of the cylinder. The amount of condensate in the cylinder should be minimized, because the condensate acts as an insulator, resisting heat transfer. In addition, the accumulation of condensate in the cylinder can also affect the runnability of the cylinder as more power is needed to drive the cylinder. A common problem in multicylinder drying is the flooding of a cylinder. In the case of flooding, the rate of dewatering is

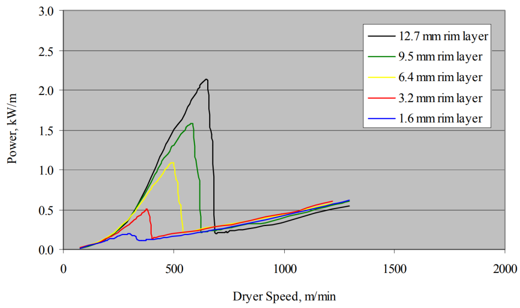

(a) Drive Power vs. dryer speed. Diameter: 1.5 m (without spoiler bars)

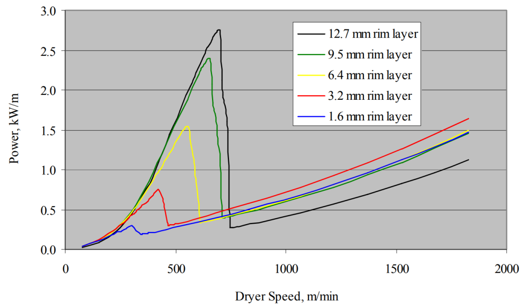

(b) Drive Power vs. dryer speed. Diameter: 1.8 m (without spoiler bars)

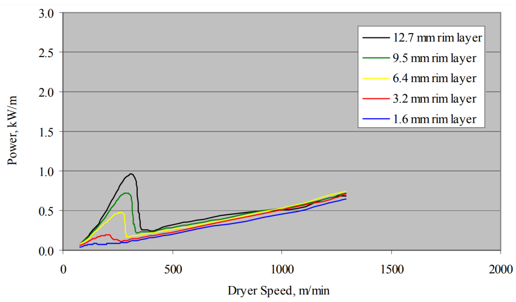

(c) Drive Power vs. dryer speed. Diameter: 1.5 m (with spoiler bars)

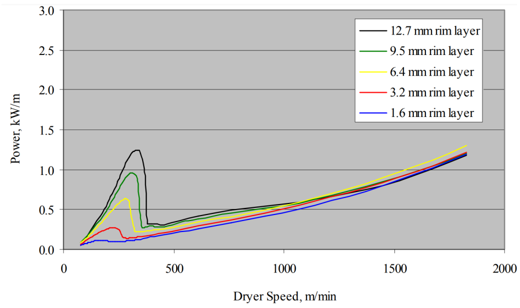

(d) Drive Power vs. dryer speed. Diameter: 1.8 m (with spoiler bars)

Figure A.1.2: Various driving powers required for different condensate levels in a 1.5 m and 1.8 m diameter drying cylinder. [18]

lower than the rate of condensate formed. If just a slight amount of flooding is occurring, the operator can still adjust the operating conditions so that the rate of dewatering becomes higher than the rate of condensate formed. However, sometimes the condensate reaches a position at which recovery by adjusting operating conditions is not possible anymore. In those cases, the cylinder needs to be drained while the whole machine is stopped, which is a very costly process.
Therefore, determining the size, type and shape of the siphons is essential for a good runnability of the dryer section. In general, three type of siphons exist: static siphons, rotating siphons and scoops.

A.1.3.1 Static siphons

A static syphon does not rotate along with the cylinder. It is mounted on the rotary joints as can be seen in figure A.1.3a. This type of siphon is mostly used for higher machine speeds, where centrifugal forces can become significant, pushing the condensate against the cylinder wall. By designing the siphon in the correct way, the kinetic energy of the condensate can be used to force the condensate into the siphon. Once the condensate is in the siphon, it is not affected by the centrifugal forces any more. Therefore, only a small differential pressure is needed over the cylinder group to drain the condensate from the system. Most of the time this kinetic energy provides insufficient energy to force the condensate towards the centerline of the cylinder. In that case blow-through steam is required to force the condensate out.

A.1.3.2 Rotating siphons

A rotating siphon is a siphon which rotates along with the cylinder (see figure A.1.3b). It works best at speeds where the centrifugal forces are moderate. As described above, for increased machine speeds, the centrifugal forces increase as well. However, different from stationary siphons, this increase in kinetic energy can not be used to drain the condensate as the siphons rotate along with the cylinder. Therefore, a larger differential pressure is required to drain the condensate, and a small hole is often present a few centimetres above the inlet of the siphon. This hole allows blow-through steam to mix with the condensate in the siphon reducing the density of the steam-condensate mixture. This

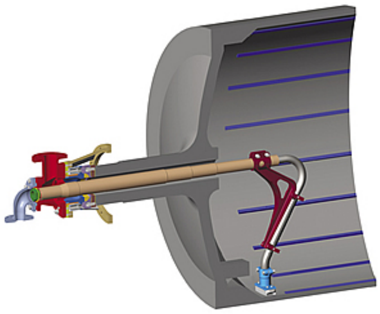

(a) Static siphon

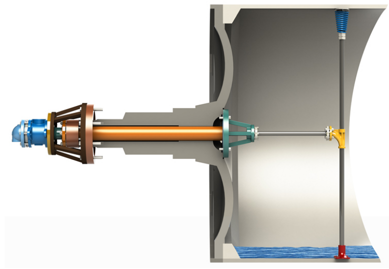

(b) Rotating siphon

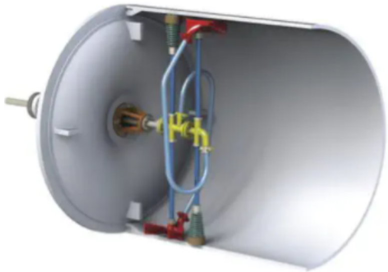

(c) Scoop

Figure A.1.3: Three common siphon configurations [19]

reduction in density requires less energy to drain the condensate to the centerline of the dryer. In this case, a larger amount of blow-through steam is required to drain the condensate. For increasing machine speeds, the centrifugal forces increase as well. Therefore, more blow-through steam is required for increased machine speeds. For that reason, static siphons are preferred for increased machine speeds. An advantage over the static siphon is the fixed siphon clearance from the cylinder wall. A rotating siphon can be mounted directly onto the cylinder wall ensuring a fixed opening for the condensate to be drained. For a static siphon its clearance can vary slightly during operation, because the static siphon is mounted to the centre of the cylinder head. This makes the clearance dependent on the stiffness of the static siphon.

A.1.3.3 Scoop-bucket

In figure A.1.3c a scoop-bucket siphon is shown. A scoop-bucket siphon can be described as a rotating bucket with a scoop mounted near the cylinder wall that works only at relative low operating speeds, where the centrifugal forces become negligible. Its driving force is gravity. Unlike the other siphon types, it does not make use of blow-through steam. At the low rotational speed, the condensate is concentrated at the bottom of the dryer. Each turn the condensate is scooped from the bottom. When the scoop attains a horizontal position, the gravitational force transports the condensate to the centerline, where a collecting pipe drains the condensate out of the cylinder. Depending on the width of the cylinder, there may be several scoops installed next to each other. Like the rotational siphons the scoop can be positioned on a fixed clearance from the cylinder wall.

A.1.4 Non-condensables

In the feed water for steam generation, some non-condensable gases are present. When steam is generated and fed into the cylinder, the transport of non-condensable gasses is unavoidable. In small quantities these gasses will not affect the operating conditions of the cylinder, but accumulation may lead to deterioration of the cylinder performance. In addition, an increasing amount of non-condensable gasses affect the vapour pressure of the water inside the cylinder. This, in turn, may affect the overall pressure and condensation temperature in the cylinder, which also affects the heat transfer to the cylinder wall [4]. By using blow-through steam, the non-condensable gasses are carried away from the cylinder, preventing the accumulation of these gasses.

A.1.5 Spoiler bars

As can seen in figure A.1.4, metal bars are present along the length direction of the cylinder. These spoiler bars have been installed in recent decades on high-speed machines to improve the heat transfer through the condensate layer while in rimming conditions. The spacing between the spoiler bars causes the condensate to oscillate between neighbouring bars. This effect increases the mixing and turbulence and thus enhances the heat transfer though the condensate layer. Wedel [93] and Saad et al. [94] derived the ideal spacing between spoiler bars to be:

$$L = \pi(r\delta_c)^{0.5} \tag{112}$$

Where:

- r: cylinder radius $[m]$
- δ_c: thickness of the condensate film $[m]$
- L: spacing between spoiler bars $[m]$

At this spacing the condensate film oscillates at its natural frequency providing maximum turbulence. An additional feature of spoiler bars is that the rimming state can be attained at lower speeds. The spoiler bars carry the water upwards with the rotating cylinders. This explains an increase in torque at lower speeds. As a result, the condensate can attain a rimming state at lower dryer speeds. As rimming conditions are often preferred over cascading conditions, it can be more efficient to install spoiler bars in cylinders just below rimming speed. In figure A.1.2c and A.1.2d the drive power versus the dryer speed is shown with spoiler bars. If compared to figure A.1.2a and A.1.2b the drive power needed to reach rimming conditions is lower with the use of spoiler bars. With rimming conditions, the spoiler bars hardly affect the driving power.

Figure A.1.4: Spoiler bars mounted on the inside of a dryer cylinder.

A.2 Yankee dryer

The creping process is shown in figure A.2.1. In figure A.2.2 a side view of a yankee dryer is presented.

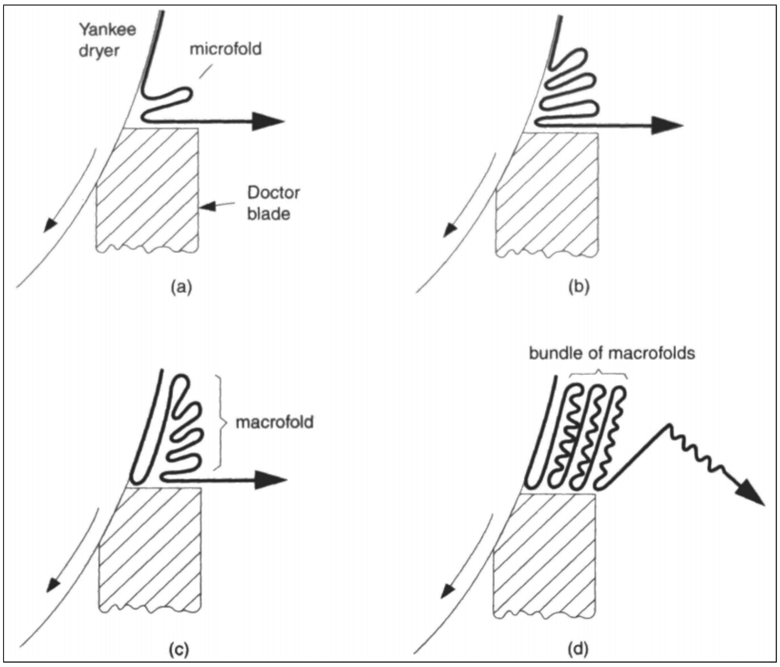

Figure A.2.1: Creping process at the end nip of the Yankee dryer. [5]

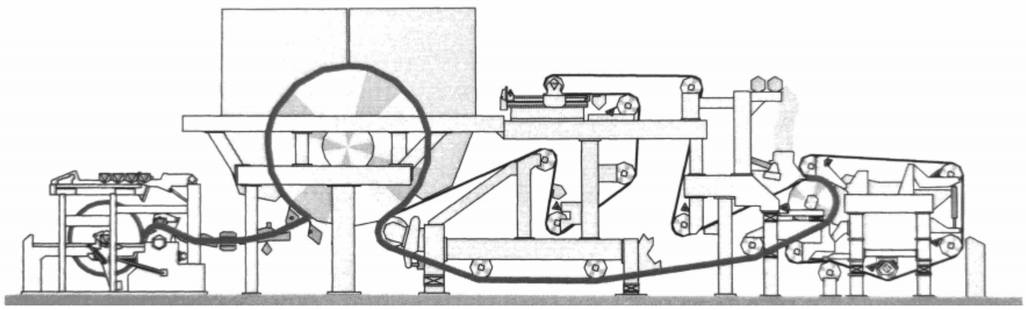

Figure A.2.2: Side view of a Yankee dryer installation. [5]

A.3 The effect of hood and basement enclosures

In general, the hood should be designed to prevent undesired air flows and to provide sufficient insulation to keep the heat inside the hood. In addition, they are used for air humidity control and heat recovery. It has two additional side benefits. Firstly, it improves the working conditions, because most of the heat and moisture is prevented from escaping to the machine floor, where the operators work. The second side benefit is the extension of the lifetime of the machinery and several equipment parts outside the hood. Due to the lower moisture content corrosion effects will be reduced.

A.3.1 Chimney effect and zero level

The chimney effect occurs when air of low density tries to escape to the outside air in upper part of a building, while in the lower parts of the building higher density air (i.e. leakage air) leaks into the building. This effect is used in the hood design for the dryer section of a paper machine. In figure A.3.1 the distribution of the under- and overpressure zones are shown. The level were the pressure inside the hood is equal to that of the outside air is known as the zero level. By adjusting the amount of supply air, the height of the zero level can be controlled so that an optimum can be achieved.
Controlling this location of the zero level is important, because too little supply air will introduce excessive leakage air. This leakage air has a comparable temperature to the outside air and will therefore be much lower than the supply air. This will effect the energy consumption negatively. The leakage air causes the air inside the hood to drop below the dew point and condensation can take place. Besides corrosive effects, the condensation can also cause droplet of water to fall on the paper web. This can result in tiny holes in the web. These tiny holes can cause breakage of the paper web further down stream the drying process, when large forces are applied on the web.
A surplus in supply air can also cause problems. Firstly, too much humid air will escape from the hood into the machine hall. This can cause excessive corrosive effects on the machinery or other metal parts in the machine hall. Secondly, the excessive air flows occurs in the pockets between the cylinders close to the paper sheet. This can cause the paper sheet to flutter, causing runnability problems.

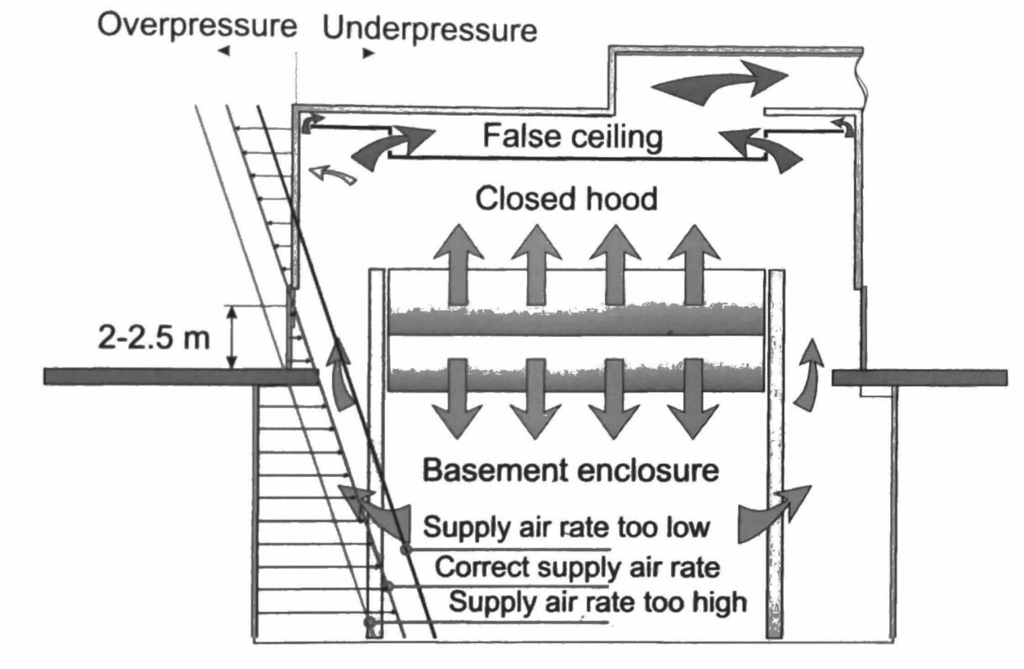

Figure A.3.1: Location of the zero-pressure level in a closed hood configuration [5]

A.4 Pocket ventilation layouts

Figure A.4.1b shows the most common ventilator type. It is mounted close to the fabric and serves two purposes. Firstly, air is injected through the fabric and almost in parallel with the paper web. This breaks the humid boundary layer and provides parallel air flows to the paper web, so that fluttering effects are minimized.
The configuration shown in figure A.4.1c is mainly used for increased machine speeds. The unsupported length of the paper web is reduced, increasing runnability. By applying an under pressure below the fabric, the paper web will stick to the fabric for a longer time. On the other side of the blow box ventilation air is supplied in the direction opposing the natural air pumping effect.
Number 1 in figure A.4.1d indicates the blow box for a single-felted configuration. A blow box was originally installed to control the air balance at moderate machine speeds only. As machine speeds and fabric permeability increased, separate blow boxes were required as well to prevent fluttering. These separate blow boxes are referred to as stabilizers. In figure A.4.1d these stabilizers are indicated with number 2. Number 3 indicates the doctor blades that is installed to scrape off dirt and separated fibres to keep the cylinder surface clean.
The presence of natural ventilation is more dominant in open pockets. Therefore, the blowbox does not provide any stability to the paper web, but only controls the air balance in the pockets. As machine speed increased, ventilation air should be supplied in the area where the sheet detaches from the cylinder. In this location the evaporation is the highest and, therefore, ventilation is needed the most. Often, air is injected along the doctor blade towards the opening nip.

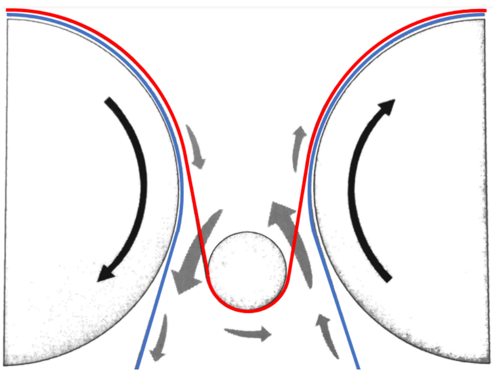

(a) Air pumping effect created by permeable fabric.

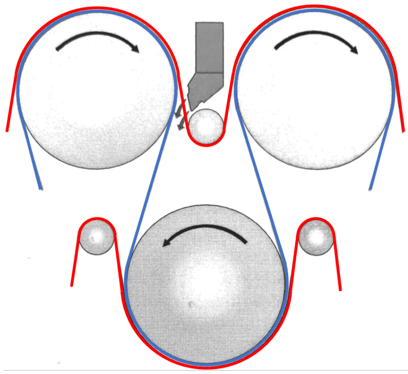

(b) Blow box in traditional double-felted configuration.

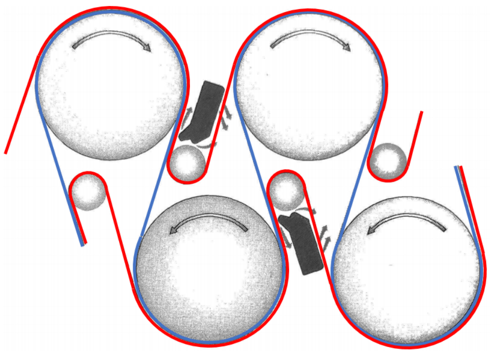

(c) Blow box in partly supported double-felted configuration.

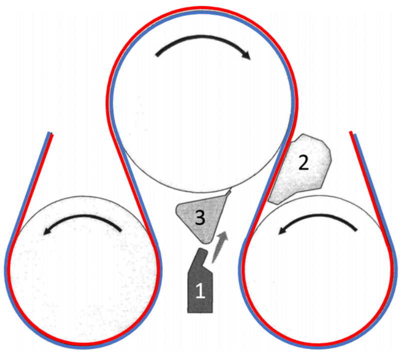

(d) Blow box (1), stabilizer (2) and doctor blade (3) in single-felted configuration.

Figure A.4.1: Air pumping effect (a) and different blow box configurations (b,c,d). The paper web and the felt are indicated in blue and red, respectively. [5]

A.5 P&ID of dryer section's steam and condensate system

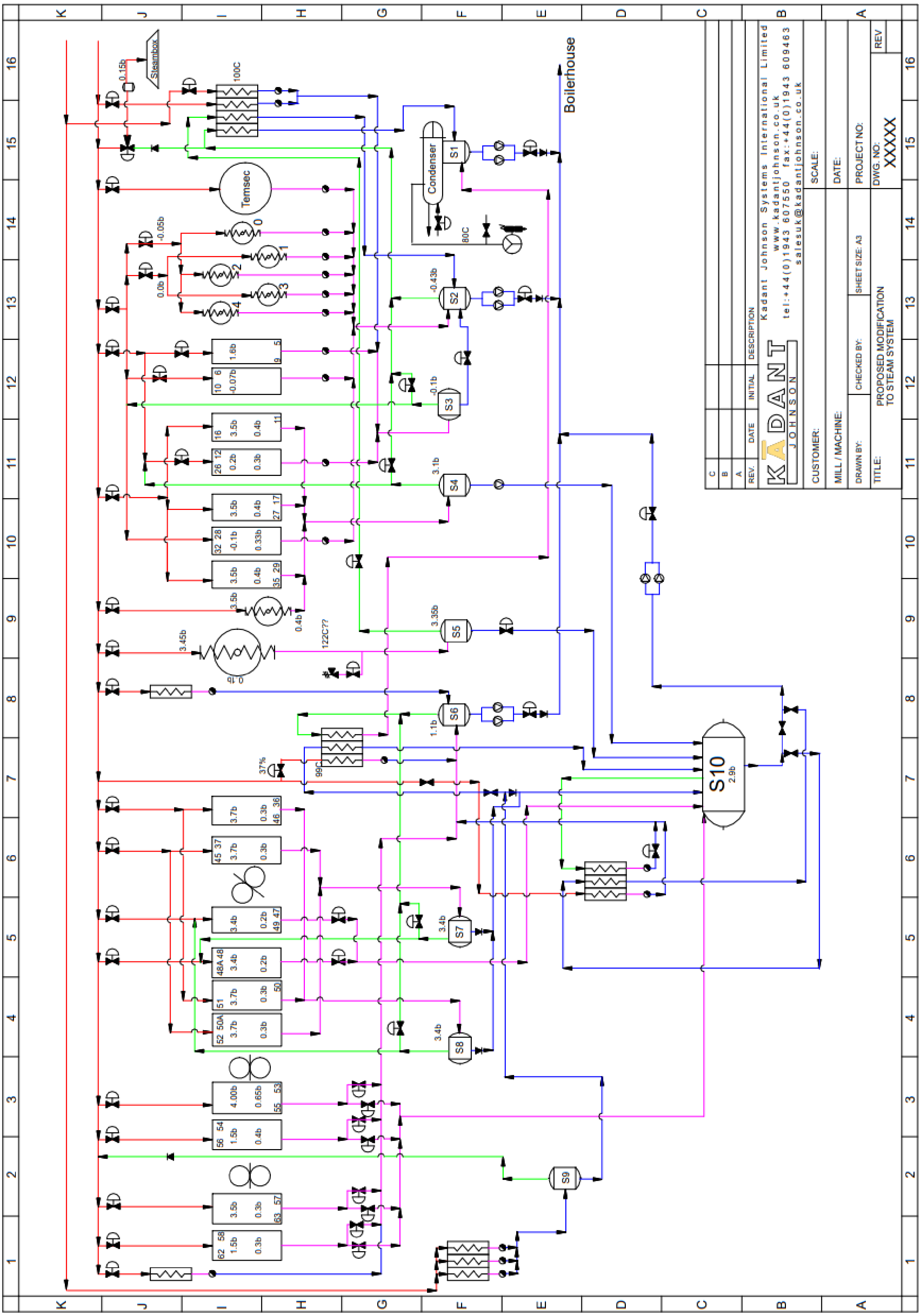

Figure A.5.1: Simplified P&ID of a steam and condensate system used in the dryer section of a paper machine.

A.6 Steam and condensate system

As described in section 2.3, a distinquison can be made between two steam and condensate systems: A cascading system and thermocompressor system.

A.6.1 Cascading system

In figure A.6.1 a typical cascading system is shown. The red line is the steam header, which provides steam to 3 groups: a low-pressure pre-dryer group, an intermediate-pressure drying group and a main group operating at higher pressures. The difference in operating pressures between the intermediate and main group is higher than the pressure drop over the main group. Therefore, the blow-through steam, used to help drain the cylinders, can be used as supply steam for the intermediate group. The same principle applies between the pre-drying group and the intermediate group: the blow-through steam from the intermediate group can be used as steam supply for the pre-dryer group.
Often the pre-drying group operates under vacuum conditions. This vacuum is created by a condenser. The blow-through steam and condensate from the pre-dryer group are collected in the most left condensate tank. As there is no more cascading potential left, the blow-through steam is transported to a condenser. The condenser condenses the blow-through steam reducing its specific volume drastically, resulting in pressure reduction. The heat exchanged in the condenser can be used to pre-heat the supply air (see section 2.4). An air-water water heat exchanger can be used in parallel to the condenser to preheat the supply air, in case the capacity of the condenser is to small. The condensate is transported back to the main condensate tank, before transported back to the boiler. A vacuum pump and valve are usually installed near the condenser. In this way, the pressure difference over the pre-dryer group (see figure(A.6.1)) can be controlled and the non-condensables can be removed from the system.

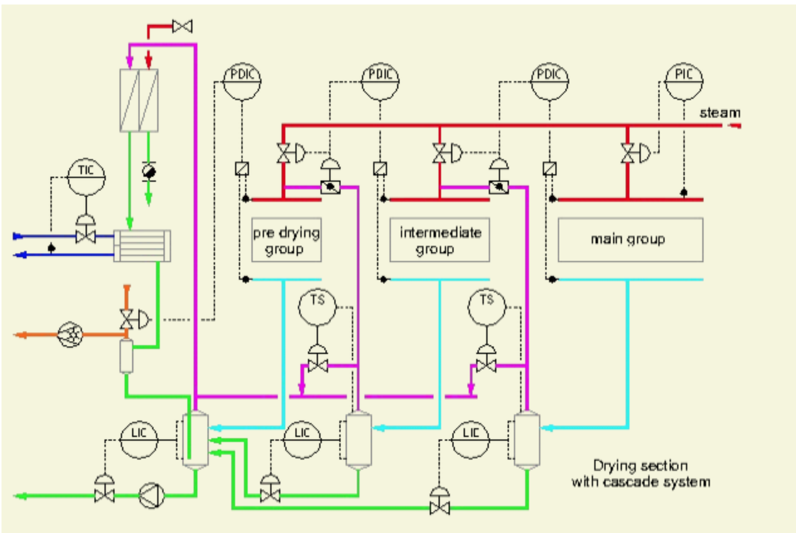

Figure A.6.1: A typical cascading steam and condensate system. In this figure, steam is cascaded twice. Note that the air-water water heat exchanger before the condenser is placed in series in this figure. [20]

A.6.2 Thermocompressor system

In figure A.6.2 and (A.6.3) a thermocompressor system and a thermocompressor are shown, respectively. In a thermocompressor high pressure steam and low pressure steam are combined to create an intermediate pressure. High pressure steam is expanded in the nozzle, resulting in a high speed steam jet ejecting from the nozzle. This creates a suction effect and causes the low pressure steam to mix with the high-speed steam. In the diffuser the speed of the mixture is reduced and an intermediate pressure level is reached. By implementing thermocompressors in the steam and condensate system, blow-through steam can be upgraded to the desired pressure level of the original steam supplied. Depending on the available high-pressure steam and the differential pressure over a certain group, the

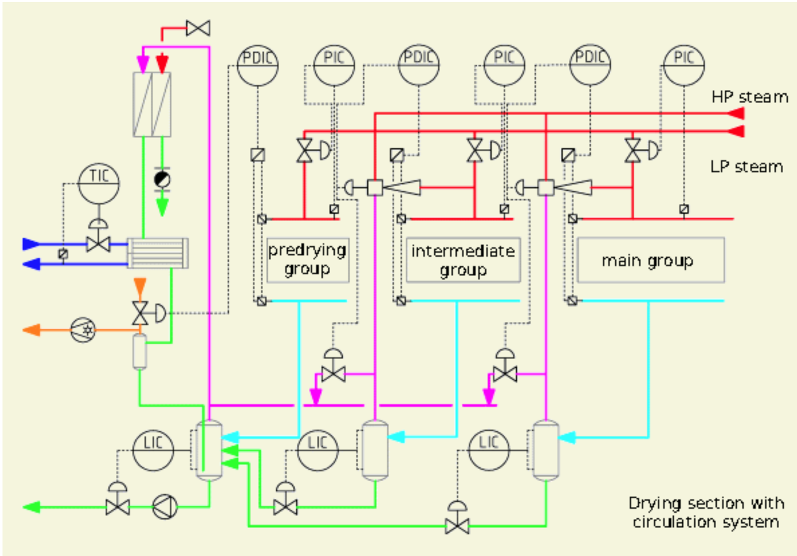

Figure A.6.2: A typical steam and condensate system that makes use of thermocompressors. In this figure, two thermocompressors are present. Note that the air-water water heat exchanger before the condenser is placed in series in this figure. [20]

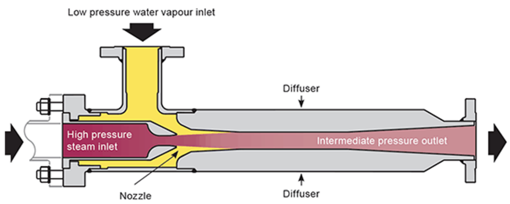

Figure A.6.3: A cross-section of a steam jet thermcompressor. [21]

amount of blow-through steam circulated is controlled.
Unlike the cascading system, a thermocompressor system allows all dryer groups to be operated under separated conditions independent from each other. In this way, higher production can be achieved during normal operation and during reduced demands the condensation pressure can be lowered in all groups. However, this system requires a high steam pressure network to be present on site. This high-pressure steam is usually more expensive compared to low pressure steam.

A.7 Dimensionless numbers

Table A.7.1: Dimensionless groups used for determining evaporation from the paper web

Dimensionless number	Definition	Interpretation
Nusselt number	$\mathrm{Nu} = \frac{h_{c_h} L}{\lambda}$	$\frac{\text{Convective heat transfer}}{\text{Conductive heat transfer}}$
Lewis number	$\mathrm{Le} = \frac{\alpha}{D_v} = \frac{\mathrm{Sc}}{\mathrm{Pr}}$	$\frac{\text{Thermal diffusivity}}{\text{Mass diffusivity}}$
Prandtl number	$\mathrm{Pr} = \frac{\nu}{\alpha}$	$\frac{\text{Momentum diffusivity}}{\text{Thermal diffusivity}}$
Reynolds number	$\mathrm{Re} = \frac{\rho\ u\ L}{\mu}$	$\frac{\text{Inertial force}}{\text{Viscous force}}$
Schmidt number	$\mathrm{Sc} = \frac{\nu}{D_v}$	$\frac{\text{Momentum diffusivity}}{\text{Mass diffusivity}}$
Sherwood number	$\mathrm{Sh} = \frac{h_{c_m} L}{D_v}$	$\frac{\text{Convective mass transfer}}{\text{Diffusive mass transfer}}$
J factor (heat transfer)	$J_H = \frac{\mathrm{Nu}}{\mathrm{Re}\mathrm{Pr}^{\frac{1}{3}}}$	
J factor (mass transfer)	$J_D = \frac{\mathrm{Sh}}{\mathrm{Re}\mathrm{Sc}^{\frac{1}{3}}}$	
J factor (momentum transfer)	$J_M = \frac{f}{2}$	

A.8 Pore size distribution functions

In the literature, many authors have used pore size distribution functions to relate the volumetric saturation to the largest radius of the liquid water-filled pores. In this way, a capillary pressure and relative permeability can be expressed as a function of moisture content.
The pore size distribution is described in several ways. Corte and Lloyd [95] described the pore size distribution using a normal distribution function. Dodson and Sampson [96] extended this work by adding a gamma function, so a more general solution was obtained. In the present study, the pore size distribution used by Reardon [11] will be examined in more detail. Reardon made use of a beta function to describe the pore size distribution. By using the a normalised pore radius and two estimation parameters, the distribution could be defined by eq. (113a).

$$g(r;a,b) = \frac{(a+b+1)!}{a!b!} r^a (1-r)^b \tag{113a}$$

Here:
- $a, b =$ are parameters to be fitted to the measured data. $[-]$
- $r =$ dimensioless pore radius: $\left(\frac{R}{R_{max}}\right)$ $[-]$

By assuming cylindrical pores, Reardon [11] defined the volumetric saturation as the ratio of the volume contained by pores up to raidus R, $V(R)$, to the volume occupied by all pores, $V(R_{max})$:

$$S = \frac{V(R)}{V(R_{max})} \tag{114}$$

The total cumulative volume of pores up to radius R can be described by:

$$V(R) = \int_0^R N\pi r^2 g(r) dr \tag{115}$$

The pore size can be related to the maximum pore size. By dividing eq.(114) by the maximum pore size (R_{max}) the formula is normalized:

$$S = \frac{V(r)}{V(1)} \tag{116}$$

Where r is defined as $\frac{R}{R_{max}}$. Eq. (116) can be further expanded using eq. (115):

$$S = \frac{\int_0^r N\pi r^2 g(r) dr}{\int_0^1 N\pi r^2 g(r) dr} \tag{117a}$$

By integrating over the whole range of normalized radii, the second moment of the distribution function is obtained:

$$\int_0^1 r^2 g(r) dr = \frac{(a+1(a+2)}{(a+b+2)(a+b+3)} \tag{118}$$

As a result, a single incomplete β function can be constructed [11]. This is given by eq.(119).

$$S = \beta(r, a+2, b) \tag{119}$$

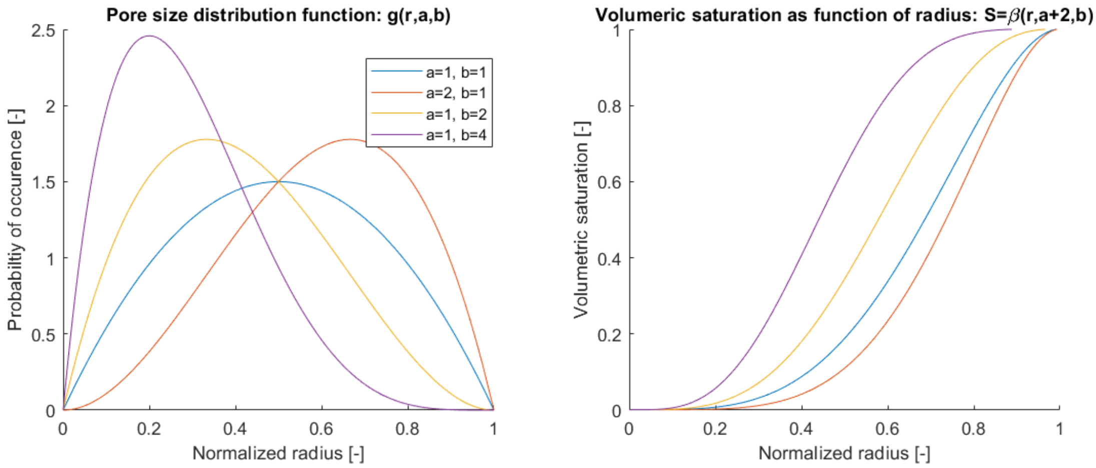

Figure A.8.1: The pore size distribution for various values of a and b (left). The corresponding incomplete beta function $\beta(r, a+2, b)$ (right).

A.9 Relating moisture content to capillary pressure

In order to to relate the moisture content to the capillary pressure, a correct estimation of the pore size distribution has to be made first (figure A.9.1a). Using the incomplete beta function, $\beta(r, a+2, b)$, the volumetric saturation of free water, S_{free}, can be determined (figure A.9.1b).
Inversion of the incomplete beta function results in the normalized radius as a function of the volumetric saturation (figure A.9.1c). By using eq.(42), the normalized radius can be substituted by the capillary pressure. In this substitution, it should be noted that the maximum pore radius, R_{max}, is inserted, because of the definition of the normalized pore radius: $r = \frac{R}{R_{max}}$. The relation of the capillary pressure as a function of the volumetric saturation is depicted in figure A.9.1d. At a certain saturation, increasing the capillary pressure will not reduce the moisture content. This point coincides with the FSP and is shown in figure A.9.1e. In this figure an arbitrary FSP is chosen to indicate the shift of the curve.

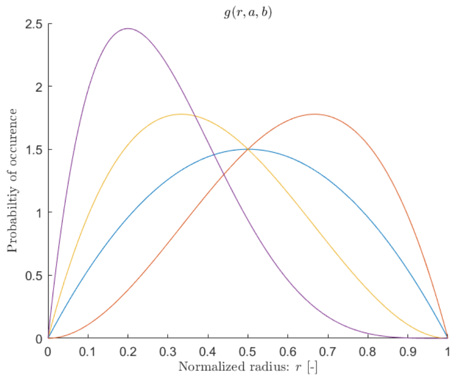

(a) Pore size distribution functions based on eq.(113a) for different values of a and b.

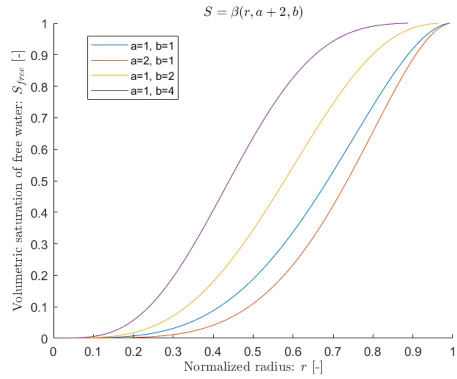

(b) Determining the volumetric saturation from the normalized radius using the incomplete beta function.

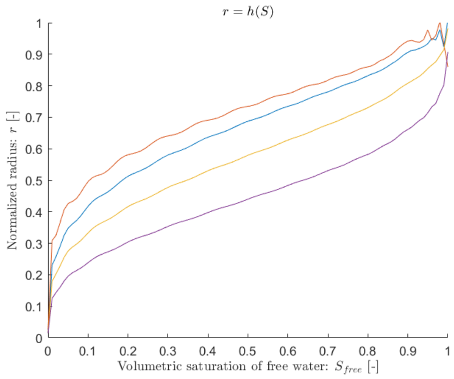

(c) The inverse function of the incomplete beta function.

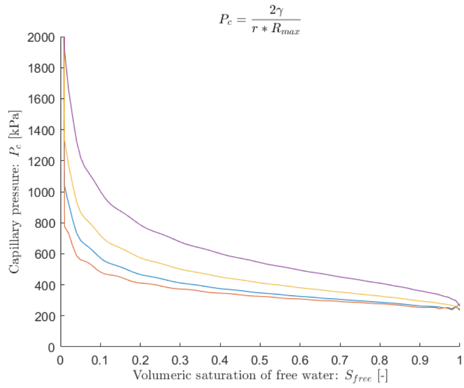

(d) Relation between the volumetric saturation of free water and the capillary pressure based on eq.(42).

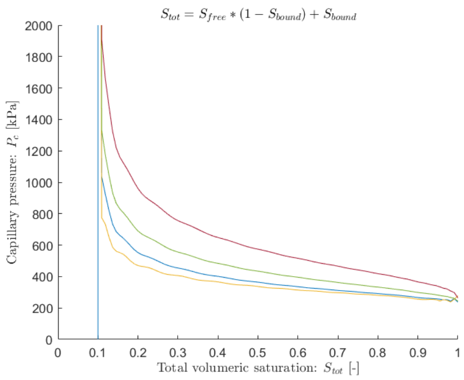

(e) Relation between the total volumetric saturation and the capillary pressure. The vertical blue line indicates the FSP.

Figure A.9.1: Derivation of the capillary pressure pressure from a pore size distribution. (a) pore size distribution functions are shown, (b) the incomplete beta function for the distribution functions, (c) the inverse of the incomplete beta function, (d) the relation between the capillary pressure and S_{free}, (e) relation between the capillary pressure and S_{tot}.

A.10 Coefficients proposed by Asensio [1]

In this section the coefficients found by Asensio [1] are reported.

Furnish	Temp. [$^\circ C$]	Equation	M_{irr}	b	c	d
LWC	24	eq.(46a)	0.491	8.848	6.519	0.967
Newsprint	24	eq.(46a)	0.349	8.257	6.413	0.950
Linerboard	24	eq.(46a)	1.132	8.541	4.179	1.319
Eucalyptus A	24	eq.(46a)	0.536	6.670	5.117	1.302
Eucalyptus B	24	eq.(46a)	0.393	7.940	3.168	1.342
NSWK	24	eq.(46a)	0.456	7.327	2.649	1.344
Linerboard	56	eq.(46a)	0.907	8.298	2.982	0.995
Eucalyptus A	56	eq.(46b)	0.504	7.229	1.051	N.A.
Eucalyptus B	56	eq.(46a)	0.488	6.809	4.143	1.315
Linerboard	85	eq.(46b)	0.702	8.417	0.304	N.A.

Table A.10.1: furnish dependent coefficients in order to calculate the capillary pressure as function of moisture content. These coefficients apply to eqs.(46a) and (46b). M_{irr} denotes the irreducible moisture content. [1]

Furnish	Temp. [$^\circ C$]	M_{irr}	Equation	a	b	c
LWC	24	0.490	eq.(86a)	0.360	4.854	0.455
Newsprint	24	0.349	eq.(86a)	0.533	4.868	0.475
Linerboard	24	1.132	eq.(86b)	0.562	1.184	0.487
Eucalyptus A	24	0.536	eq.(86a)	0.021	4.164	0.578
Eucalyptus B	24	0.393	eq.(86b)	0.494	4.156	0.500
NSWK	24	0.456	eq.(86a)	0.127	4.221	0.459
Linerboard	56	0.907	eq.(86b)	1.254	4.522	0.670
Eucalyptus A	56	0.504	eq.(86b)	1.447	4.528	0.704
Eucalyptus B	56	0.488	eq.(86b)	0.215	4.114	0.593
Linerboard	85	0.702	eq.(86b)	1.337	4.524	0.665

Table A.10.2: Relative permeability of liquid water according to Asensio [1]. X_b denotes the beginning of the hygroscopic region. Table taken from Sadeghi [22]. The coefficients apply to eq.(86a) and (86b).

Furnish	Temp. [$^\circ C$]	Equation	a	b	c	d
LWC	24	eq.(86c)	-0.173	1.163	0.563	3.501
Newsprint	24	eq.(86c)	-0.123	1.109	0.510	3.778
Linerboard	24	eq.(86c)	-0.148	1.132	0.847	3.092
Eucalyptus A	24	eq.(86c)	-0.178	1.164	0.941	3.041
Eucalyptus B	24	eq.(86c)	-0.161	1.146	0.873	3.026
NSWK	24	eq.(86c)	-0.171	1.156	0.633	2.971
Linerboard	56	eq.(86c)	-0.141	1.127	0.788	3.598
Eucalyptus A	56	eq.(86c)	-0.172	1.161	0.780	3.476
Eucalyptus B	56	eq.(86c)	-0.182	1.168	1.050	3.028
Linerboard	85	eq.(86c)	-0.185	1.175	0.796	3.411

Table A.10.3: Relative permeability of water vapour according to Asensio [1]. Table taken from Sadeghi [22]. The coefficients apply to eq.(86c)

A.11 The Kelvin effect

In the beginning of the drying process, evaporation can be modeled as evaporation from a free water surface. Therefore, its vapour pressure is equal to the saturation vapour pressure and could be determined using Antoine's equation (eq.(9)).
In the pores, the vapour pressure is reduced by the meniscus curvature. In this case the saturated vapour pressure is lower than the saturated vapour pressure for a flat water-vapour interface. This is known as the Kelvin effect and can be described by eq.(120) [9]:

$$\frac{P_v}{P'_v = \exp\left\{-\frac{M_v}{RT}\frac{P_c}{\rho_l}\right\}(120)}$$

Substituting for the capillary pressure (eq.(42)) and assuming a perfectly wetted inner pore surface ($cos(\theta) = 1$) gives:

$$\frac{P_v}{P'_v = \exp\left\{-\frac{M_v}{RT}\frac{2\gamma}{\rho_l r}\right\}(121)}$$

Where:

- P_v = vapour pressure $[kPa]$
- P_v^* = Saturation vapour pressure $[kPa]$
- M_v = Molecular weight $[kg/mol]$
- R = Gas constant: 8.314 $[\frac{J}{molK}]$
- T = Temperature $[K]$
- ρ_L = Water density $[\frac{kg}{m^3}]$
- γ = Surface tension $[\frac{N}{m}]$
- r = Normalized pore radius $[m]$

This effect only becomes significant in case for very small pore radii. Therefore, this effect only is accounted for once the water-vapour interface has moved to pores with very small radii. In these radii only bound water is presented. Therefore, the onset of this effect can be taken from the FSP. This effect is also captured by sorption isotherms and therefore the Kelvin equation will not be directly be used in the model. Nevertheless, it is important to be aware of the transportation mechanisms, as it is physically present in the web.

A.12 Cylinder groups

As described earlier, a full description of the steam and condensate lay-out is ommitted here, because this is outside the scope of this project. Instead, table A.12.1 provides a summary of how the steam supply is connected to the different cylinder. As can be deduced from the table steam is supplied in groups to the cylinders. Each group, consisting of a number of cylinders, can operate at different conditions. In this way, paperdrying can be controlled. Each cylinder group operates a certain pressure. By assuming saturated conditions, the temperature can be deduced as well. The steam and condensate removed is measured per cylinder group. Assuming that only steam is supplied to the cylinders, the steam supply can be calculated as the sum of those two. The heat released per cylinder group can be calculated according to eq.(...). In this case, saturated conditions are assumed.

$$Q = H_{latent}((\dot{m}_{cond} + \dot{m}_{steam})_{removed} - \dot{m}_{steam\ supplied}) \tag{122}$$

Where:

- Q = Heat released in cylinder group $\left[\frac{kJ}{s}\right]$
- H_{latent} = Latent heat $\left[\frac{kJ}{kg}\right]$
- m_{cond} = rate of condensate removed from cylinder group $\left[\frac{kg}{s}\right]$
- m_{steam} = rate of steam removed from cylinder group $\left[\frac{kJ}{s}\right]$

The first 7 groups are located in the pre-dryer section. The first two groups operate at a relative low pressure, because the paper web needs a certain warm-up period. This period is necessary so that the paper web does not stick to the cylinders. Note that the bottom cylinders (the odd cylinder numbers) operate at a lower pressure. This is done to control the curling effect throughout the dryer section. At the MG, only one side of the paper web is in contact with the heated cylinder wall, causing an uneven drying profile in the thickness direction. The consequence of this uneven profile results in a curl in the web. In order to counter this curling effect, the other side of paper web is dried to a further extend in the pre-dryer section. In this way a curl in opposite direction is applied in the predyer section. Therefore, only a limited amount of curl occurs after the MG.

Note that the pre-MG and MG operate at high temperatures and consume the most steam per second, while they represent only one cylinder. This results in very intense drying. Unfortunately, there was no information available about the steam consumption in both correction groups, making it impossible to complete a heat balance over these groups.

Dryer section	Group	Cylinders	Press. $[kPa]$	Temp. $[^{\circ}C]$	Steam supply $\left[\frac{kg}{s}\right]$	Cond. removal $\left[\frac{kg}{s}\right]$	Steam removal $\left[\frac{kg}{s}\right]$	Heat released $\left[\frac{kJ}{s}\right]$
Pre-dryer	1	0, 2, 4	91	97	0.0453	0.0287	0.0167	65
Pre-dryer	2	1, 3	81	94	0.0465	0.0326	0.0139	74
Pre-dryer	3	5, 7, 9	140	109	0.0806	0.0426	0.0380	95
Pre-dryer	4	6, 8, 10	89	96	0.0537	0.0296	0.0241	67
Pre-dryer	5	11, 13, ..., 31, 33, 34, 35	341	138	0.1901	0.1452	0.0448	312
Pre-dryer	6	12, 14, ..., 24, 26	122	105	0.1300	0.0689	0.0611	155
Pre-dryer	7	28, 30, 32	71	90	0.0727	0.0343	0.0384	78
Pre-MG	8	35A	341	138	0.4194	0.2667	0.1528	573
MG	9	35B	312	135	0.4444	0.3333	0.1111	720
1st After dryer	10	36, 38, ..., 46, 48	261	129	0.1712	0.0506	0.1206	110
1st After dryer	11	37, 39, ..., 47, 49	260	129	0.1722	0.0508	0.1214	111
2nd After dryer	12	50, 52, 54, 56	223	124	0.1479	0.0799	0.0681	175
2nd After dryer	13	51, 53, 55	224	124	0.1972	0.0787	0.1185	172
1st Correction	14	57, 59	261	129	0	0	0	0
1st Correction	15	58, 60	141	110	0	0	0	0
2nd Correction	16	61, 63, 65, 67	261	129	0	0	0	0
2nd Correction	17	62, 64, 66	141	110	0	0	0	0

Table A.12.1: Overview of the cylinder that are grouped together and connected to a single steam supply stream. Also the conditions in the cylinders are reported. The pressure in the cylinders were measured directly, while the temperature is derived on the assumption that saturated conditions occur in the cylinders. The heat removal from each group is calculated by multiplying the amount of condensed steam with the latent heat (eq.(122)). Note that the number of the cylinders refer to the numbers used in figure 7.4.

A.13 Speedsizer and coating specifications

It is essential that specifications of the speedsizer and coating solutions are reported. This is done in table A.13.1. As can be seen in the table, the mixture added in the speedsizer consists of three separate solutions and the mixture added in the coaters consists of two separate solutions.

It is assumed that the mixtures added in the speedsizer and the coaters fully attache to the paper web. Furthermore, no information on the distribution of coating added between the coaters was reported. Therefore, it is assumed that the coating added equally distributed. With these assumptions it is possible to rewrite the information in terms of mass flow added to the paper web. In this way the information can easily be implemented in the mass balance. Calculating the different mass flows was done using equations:

$$\dot{m}_i(solid) = \frac{1}{3600} \times (\dot{V}_i \rho_i x_i) \tag{123a}$$

$$\dot{m}_i(water) = \frac{1}{3600} \times (\dot{V}_i \rho_i (1 - x_i)) \tag{123b}$$

$$\dot{m}_{spd}(solid) = \dot{m}_{AL}(solid) + \dot{m}_{DL}(solid) + \dot{m}_{Unidyne}(solid) \tag{123c}$$

$$\dot{m}_{spd}(water) = \dot{m}_{AL}(water) + \dot{m}_{DL}(water) + \dot{m}_{Unidyne}(water) \tag{123d}$$

$$\dot{m}_{coat}(solid) = \frac{\dot{m}_{DS}(solid) + \dot{m}_{TS}(solid)}{2} \tag{123e}$$

$$\dot{m}_{coat}(water) = \frac{\dot{m}_{DS}(water) + \dot{m}_{TS}(water)}{2} \tag{123f}$$

Where:

- i = Solutions AL, DL, $Unidyne$, DS or TS.
- $m_i(dry)$ = mass flow of solids in different solutions $\left[\frac{kg}{s}\right]$
- $m_i(water)$ = mass flow of water in different solutions $\left[\frac{kg}{s}\right]$
- $m_{spd}(dry)$ = mass flow of solids added in speedsizer $\left[\frac{kg}{s}\right]$
- $m_{spd}(water)$ = mass flow of water added in speedsizer $\left[\frac{kg}{s}\right]$
- $m_{coat}(dry)$ = mass flow of solids added per coater $\left[\frac{kg}{s}\right]$
- $m_{coat}(water)$ = mass flow of water added per coater $\left[\frac{kg}{s}\right]$

		Speedsizer			Coating	
		AL	DL	Unidyne	DS	TS
Concentration	$\left[\frac{kg_{dry}}{kg_{total}}\right]$	0.25	0.25	1	0.665	0.665
Density	$\left[\frac{kg}{L}\right]$	1.055	1.055	1.0	1.625	1.56
Flow rate	$\left[\frac{L}{h}\right]$	326	846	74.0	979	1095

Table A.13.1: The specifications of the different solutions added to the paper in the dryer section. Note that the concentration and the density of the solution is independent of the day the survey was performed. The flowrate was not measured at 24-09-2020, but conditions were similar that of 22-09-2020. Therefore, these values are assumed to be similar.

A.14 Fan flowrates

Fan Location*	T_{wet} $[°C]$	T_{dry} $[°C]$	x $\left[\frac{g_{water}}{kg_{d.a.}}\right]$	Q $\left[\frac{m^3}{h}\right]$	ρ $\left[\frac{kg}{m^3}\right]$	$\dot{m}_{tot}$ $\left[\frac{kg}{s}\right]$	$\dot{m}_w$ $\left[\frac{kg}{s}\right]$	$\dot{m}_{d.a.}$ $\left[\frac{kg}{s}\right]$
1	48.3	74.2	66.5	55500	0.9788	15.09	0.94	14.15
2	54.5	80.6	98.7	55500	0.9459	14.58	1.31	13.27
3	54.9	80.3	101.5	37000	0.9454	9.72	0.90	8.82
5	52.2	80.0	84.6	44000	0.9540	11.77	0.92	10.85
7	44.3	66.1	52.8	50000	1.0094	14.02	0.70	13.32
9	41.0	82.2	33.7	12200	0.9737	3.30	0.11	3.19
10	34.2	62.5	22.8	20000	1.0372	5.76	0.13	5.63
11	34.2	62.5	22.8	20000	1.0372	5.76	0.13	5.63
14	39.3	104.1	19.2	54114**	0.9248	13.90	0.26	13.64
15	39.3	115.1	14.7	4.9158**	0.9009	12.30	0.18	12.12
18	47.3	112.6	13.3	15000	0.9075	3.78	0.05	3.73
23	38.7	96.0	20.8	30000	0.9442	7.87	0.16	7.71

* The number refers to the streams labeled in figure 7.4.
** These values are corrected for steam leakage occurring in the pre-heaters.

Table A.14.1: Information about air streams necessary to compute mass balance. Note that the volumetric flow rate is derived from the fan specifications.

A.15 Calculating mass flows per dryer section

Second correction group
The dry solids and water mass flow in the paper sheet at the end of the second correction group can be calculated according to eq.(124a) and eq.(124b), respectively. The dry solids and water mass flow in the paper sheet at the beginning of the second correction group can be directly computed by using eqs.(124c) and (124d). In these equations, W denotes the width of the dryer section, Gr is the grammage of the paper web and u represents the machine speed. The grammage is defined as the total weight of the paper web per surface area.

$$\dot{m}_{w}^{out}\,(2^{nd}\ cor.) = M_{wet}\ Gr\ W\ u \tag{124a}$$
$$\dot{m}_{d.s.}^{out}\,(2^{nd}\ cor.) = (1 - M_{wet})\ Gr\ W\ u \tag{124b}$$
$$\dot{m}_{w}^{in}\,(2^{nd}\ cor.) = \dot{m}_{w}^{out}\,(2^{nd}\ cor.)\ +\ \dot{m}_{evap}\,(2^{nd}\ cor.) \tag{124c}$$
$$\dot{m}_{d.s.}^{in}\,(2^{nd}\ cor.) = \dot{m}_{d.s.}^{out}\,(2^{nd}\ cor.) \tag{124d}$$

First correction group
In order to calculate the outlet mass flows of the paper sheet at the first correction group, the mass flow of the second coater have to be added to the inlet conditions of the second correction group (eqs.(125a)and (125b)). The inlet mass flows can be calculated in a similar way to the second correction group.

$$\dot{m}_{w}^{out}\,(1^{st}\ cor.) = \dot{m}_{w}^{in}\,(2^{nd}\ cor.)\ +\ \dot{m}_{w}\,(2^{nd}\ coater.) \tag{125a}$$
$$\dot{m}_{d.s.}^{out}\,(1^{st}\ cor.) = \dot{m}_{d.s.}^{in}\,(2^{nd}\ cor.)\ +\ \dot{m}_{d.s.}\,(2^{nd}\ coater.) \tag{125b}$$
$$\dot{m}_{w}^{in}\,(1^{st}\ cor.) = \dot{m}_{w}^{out}\,(2^{nd}\ cor.)\ +\ \dot{m}_{evap}\,(2^{nd}\ cor.) \tag{125c}$$
$$\dot{m}_{d.s.}^{in}\,(1^{st}\ cor.) = \dot{m}_{d.s.}^{out}\,(2^{nd}\ cor.) \tag{125d}$$

Second Afterdryer group
The mass flow of the first coater are combined with the inlet mass flows of the first correction group to calculate the outlet mass flows of the second after dryer group (eqs.(126a)and (126b)). The inlet mass flows can be calculated in a similar way to the correction groups.

$$\dot{m}_{w}^{out}\,(2^{nd}\ aft.\ dry.) = \dot{m}_{w}^{in}\,(1^{st}\ cor.)\ +\ \dot{m}_{w}\,(1^{st}\ coater.) \tag{126a}$$
$$\dot{m}_{d.s.}^{out}\,(2^{nd}\ aft.\ dry.) = \dot{m}_{d.s.}^{in}\,(1^{st}\ cor.)\ +\ \dot{m}_{d.s.}\,(1^{st}\ coater.) \tag{126b}$$
$$\dot{m}_{w}^{in}\,(2^{nd}\ aft.\ dry.) = \dot{m}_{w}^{out}\,(2^{nd}\ aft.\ dry.)\ +\ \dot{m}_{evap}\,(2^{nd}\ aft.\ dry.) \tag{126c}$$
$$\dot{m}_{d.s.}^{in}\,(2^{nd}\ aft.\ dry.) = \dot{m}_{d.s.}^{out}\,(2^{nd}\ aft.\ dry.) \tag{126d}$$

First Afterdryer group
The mass flow of the speedsizer is combined with the inlet mass flows of the second after dryer group to calculate the outlet mass flows of the first after dryer group (eqs.(127a)and (127b)). The inlet mass flows can be calculated in a similar way to the correction groups and second after dryer group.

$$\dot{m}_{w}^{out}\,(1^{st}\ aft.\ dry.) = \dot{m}_{w}^{in}\,(2^{nd}\ aft.\ dry.)\ +\ \dot{m}_{w}\,(Speedsizer) \tag{127a}$$
$$\dot{m}_{d.s.}^{out}\,(1^{st}\ aft.\ dry.) = \dot{m}_{d.s.}^{in}\,(2^{nd}\ aft.\ dry.)\ +\ \dot{m}_{d.s.}\,(Speedsizer) \tag{127b}$$
$$\dot{m}_{w}^{in}\,(1^{st}\ aft.\ dry.) = \dot{m}_{w}^{out}\,(1^{st}\ aft.\ dry.)\ +\ \dot{m}_{evap}\,(1^{st}\ aft.\ dry.) \tag{127c}$$
$$\dot{m}_{d.s.}^{in}\,(1^{st}\ aft.\ dry.) = \dot{m}_{d.s.}^{out}\,(1^{st}\ aft.\ dry.) \tag{127d}$$

Pre-dryer
Ventilation data for the MG were unavailable and no mass balance could be performed over this dryer

section. In addition, this makes it impossible to calculate the mass flow of water at the outlet of the pre-dryer group. However, by assuming that there is no change of mass flow of dry solids over the MG, the dry solids mass flow at the end of the pre-dryer section is equal to the dry solids mass flow at the beginning of the first after dryer group (eq(128a)). The moisture content at the beginning of the pre-dryer section is known. Combining this moisture content with the mass flow of dry solids at the beginning of the pre-dryer section results in the mass flow of water(eq.(128c)). Finally, the mass flow of water in the outlet of the Pre-dryer be calculated by subtracting the evapourated water form the inlet mass flow (eq.(128d)).

$$\dot{m}_{d.s.}^{out}\ (Pre-dryer) = \dot{m}_{d.s.}^{in}\ (1^{st}\ aft.\ dry.) \tag{128a}$$

$$\dot{m}_{d.s.}^{in}\ (Pre-dryer) = \dot{m}_{d.s.}^{out}\ (Pre-dryer) \tag{128b}$$

$$\dot{m}_{w}^{in}\ (Pre-dryer) = \frac{M_{wet}}{1-M_{wet}}\ \dot{m}_{d.s.}^{in}\ (Pre-dryer) \tag{128c}$$

$$\dot{m}_{w}^{out}\ (Pre-dryer) = \dot{m}_{w}^{in}\ (Pre-dryer)\ -\ \dot{m}_{evap}\ (Pre-dryer) \tag{128d}$$

MG

At this point, the mass flow of water and dry solids at the end of the pre-dryer section and the beginning of the first after dryer group are known. It is assumed that the in- and outlet conditions of the MG correspond to the out- and inlet conditions of the pre-dryer and first afterdryer, respectively (eqs.(129)).

$$\dot{m}_{d.s.}^{in}\ (MG) = \dot{m}_{d.s.}^{out}\ (Pre-dryer) \tag{129a}$$

$$\dot{m}_{d.s.}^{out}\ (MG) = \dot{m}_{d.s.}^{in}\ (1^{st}\ aft.\ dry.) \tag{129b}$$

$$\dot{m}_{w}^{in}\ (MG) = \dot{m}_{w}^{out}\ (Pre-dryer) \tag{129c}$$

$$\dot{m}_{w}^{out}\ (MG) = \dot{m}_{w}^{in}\ (1^{st}\ aft.\ dry.) \tag{129d}$$

A.16 Measured temperatures and humidity's per cylinder

Cyl. Numb.	Web temp. $[°C]$		Cylinder temp. $[°C]$	Pocket temp. $[°C]$		Humidity $\left[\frac{g}{m^3}\right]$
	before	after		T_{dry}	T_{wet}	
0	52	55	74	54	40	43
1	52	53	81.8	55	41	45
2	51	61	89.5	61	46	62
3	52	53	82	59	42	47
4	51	66	89.5	55	39	39
5	53	59	101.9	62	44	53
6	53	55	88.4	63	47	66
7	55	58	102	67	44	51
8	53	56	88.9	64	47	65
9	56	64	103.2	65	46	60
10	55	63	89	65	38	31
11	57	77	111.5	79	52	85
12	65	76	86	72	54	100
13	73	84	115.5	77	58	128
14	74	81	90.8	71	57	122
15	79	87	116	82	62	163
16	79	92	-	-	-	-
17	73	85	111.7	82	60	143
18	77	81	87.3	76	62	165
19	83	92	116.2	83	75	381
20	77	83	-	-	-	-
21	80	84	-	-	-	-
22	82	-	-	-	-	-
23	78	77	86.1	78	61	154
24	73	80	89.3	71	42	42
25	77	87	112	81	52	84
26	81	82	91.8			
27	80	88	112.5	87	64	183
28	77	-	-	-	-	-
29	82	86	-	-	-	-
30	78	-	-	-	-	-
31	73	89	112.2	77	57	120
32	77	77	82.5	74	66	214
33	77	91	116.3	71	50	77
34	-	-	-	68	55	109
35	77	91	116.2	65	40	38
35a	82	98	115.5	78	54	98
MG	68	89	99.5	64	47	65
36	78	93	113.3	87	59	132
37	80	95	110.3	79	59	135
38	90	99	116.8	93	62	158
39	86	96	-	-	-	-
40	93	100	116.5	94	63	168

Cyl. Numb.	Web temp. $[°C]$		Cylinder temp. $[°C]$	Pocket temp. $[°C]$		Humidity $\left[\frac{g}{m^3}\right]$
	before	after		Tdry	Twet	
41	82	96	-	-	-	-
42	88	91	-	-	-	-
43	84	95	-	-	-	-
44	88	99	114.8	63	42	45
45	86	98	113.6	97	52	76
46	92	102	117.2	93	58	120
47	86	104	-	-	-	-
48	-	-		-	-	-
49	-	-	-	-	-	-
50	48	79	102.2	53	35	28
51	63	84	103.3	72	51	82
52	71	94	-	-	-	-
53	77	84	-	-	-	-
54	86	99	-	-	-	-
55	82	92	108.6	79	60	144
56	84	93	105.9	63	55	111
57	63	79	115.2	60	37	31
58	65	83	95.3	56	35	27
59	79	86	117	66	42	44
60	79	89	98.9	57	35	27
61	71	84	117.8	106	48	51
62	77	86	103.5	60	33	20
63	83	89	119.5	80	47	58
64	83	93	103.8	74	40	34
65	91	96	120.5	86	50	70
66	88	93	104.3	70	39	32
67	92	96	120.6	69	39	33
68	88	82	-	-	-	-
69	78	67	-	-	-	-
70	70	69	-	-	-	-

Table A.16.1: Temperature measurements per cylinder.

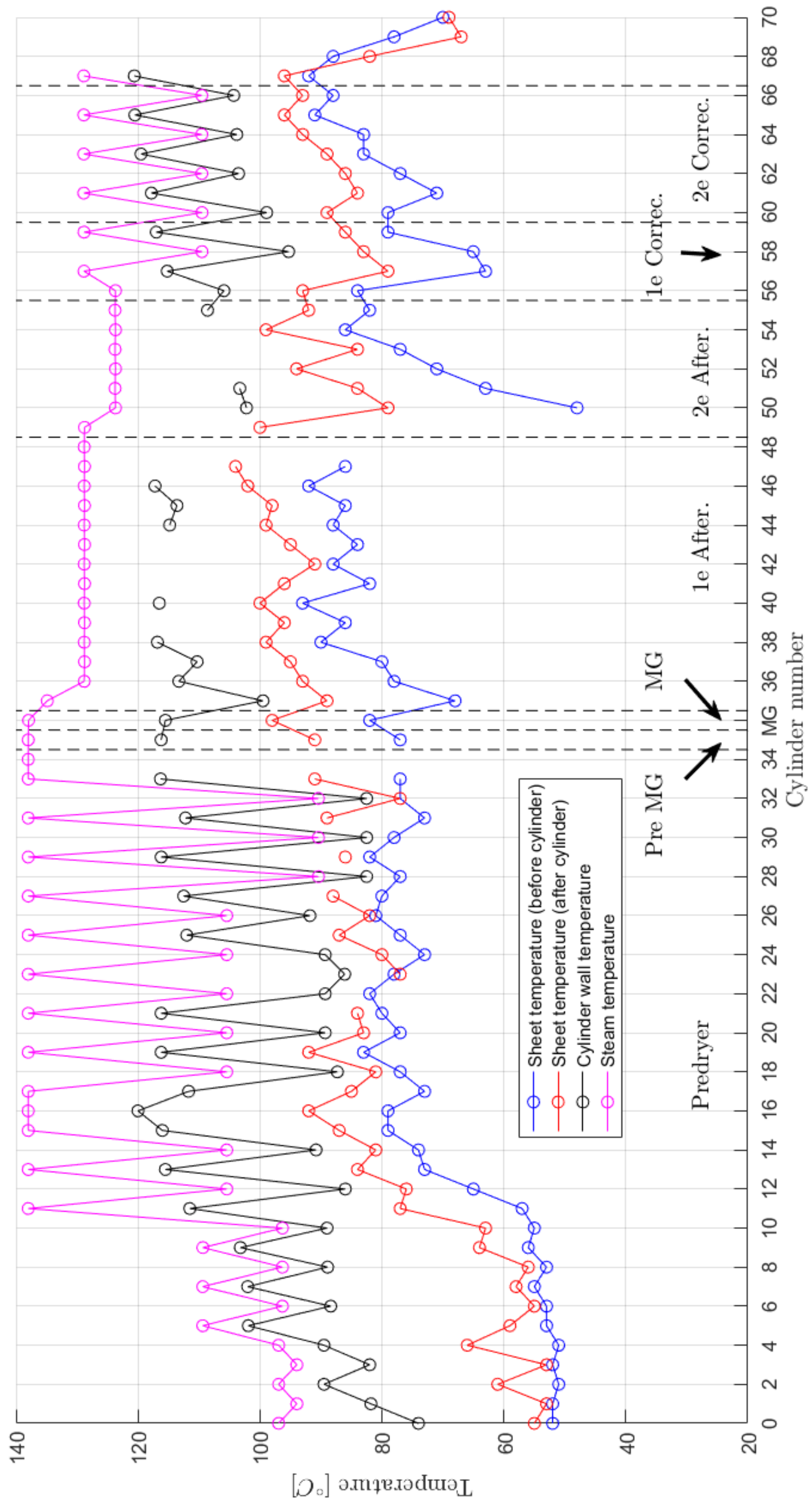

Figure A.16.1: Measured temperatures at the field survey.

A.17 Reduction of volumetric flow rate

As can be seen from figure 7.4, three exhaust fans exist in the pre-dryer section. In table (A.17.1) the properties of each fans and corresponding exhaust flow are tabulated. The total density of the air mixture, ρ_{tot}, is calculated according to eq.(130a). Subsequently, the mass flow rate of the vapour through each ventilator, $\dot{m}_v$, can be calculated according to eq.(130b).

$$\rho_{tot} = \rho_v z_v + \rho_{d.a.}(1 - z_v) \tag{130a}$$

$$\dot{m}_v = Q \rho_{tot} z_v \tag{130b}$$

z_v denotes the moisture content of the air in $\left[\frac{kg_{vapour}}{kg_{tot}}\right]$.

When the relative humidity is set to a fixed value, a new volumetric flow rate through the fans can be calculated. In order to transport the same amount of vapour, the vapour mass flow rate should remain the same. Furthermore, it can be assumed that the same temperatures apply. Firstly, the saturated moisture content of air is calculated using eqs. (7) and (9). Subsequently, the new moisture content of air can calculated as:

$$x_v = RH \times x_v' \tag{131}$$

RH, x_v' and x_v represent the relative humidity $[-]$, the saturated moisture content of air and the actual moisture content of air, respectively. Note that in this case the moisture content has units of $\left[\frac{kg_{vapour}}{kg_{dry\ air}}\right]$. The moisture content of the air per total weight of air can be calculated according to:

$$z_v = \frac{x_v}{x_v + 1} \tag{132}$$

The total volumetric flow rate required. to transfer the same amount of vapour with, can be calculated according to:

$$Q = \frac{\dot{m}_v}{z_v \rho_{tot}} \tag{133}$$

In this case Q represent the total volumetric flow rate required to transfer the same amount of vapour for the current operating conditions.

Ventilator	Total flow rate $\left[\frac{m^3}{h}\right]$	Moisture content $\left[\frac{kg_{vapour}}{kg_{tot}}\right]$	Temperature $[°C]$	Density $\left[\frac{kg}{m^3}\right]$	vapour flow rate $\left[\frac{kg}{h}\right]$
1	55500	0.0627	74.2	0.9639	3610
2	55500	0.0901	80.6	0.9318	5365
3	37000	0.0925	80.3	0.9306	3677

Table A.17.1: Flow rate specifications of the pre-dryer ventilators.

Ventilator	Relative humidity $[-]$	Temperature $[°C]$	Moisture content $\left[\frac{kg_{vapour}}{kg_{tot}}\right]$	Total flow rate $\left[\frac{m^3}{h}\right]$	Flow reduction $[\%]$
1	0.8	74.2	0.2268	19034	65.7%
2	0.8	80.6	0.3201	21705	60.9%
3	0.8	80.3	0.3419	15059	59.3%

Table A.17.2: Calculated reduction in volumetric flow rates in case the relative humidity is fixed at 0.8$[-]$.

A.18 Heat transfer per cylinder

Cylinder	Energy input [kW]	Cylinder	Energy input [kW]
1	0.806	19	4.432
2	0.967	20	0.848
3	0.726	21	3.790
4	0.900	22	0.521
5	1.188	23	0.936
6	0.782	24	1.528
7	1.126	25	3.898
8	0.741	26	1.249
9	1.117	27	3.617
10	0.728	28	0.612
11	6.081	29	3.729
12	0.882	30	0.272
13	5.273	31	3.573
14	0.898	32	0.369
15	5.195	33	3.981
16	5.289	34	5.021
17	4.476	35	3.430
18	0.644	35A (Pre-MG)	6.1853

Table A.18.1: Energy transfer from the cylinder to the paper web.